Master's thesis

NTNU
Norwegian University of Science and Technology
Faculty of Information Technology and Electrical Engineering
Department of Engineering Cybernetics

Mari Linnerud

Heading estimation during motor-related magnetic disturbances

Master's thesis in Cybernetics and Robotics
Supervisor: Øyvind Stavdahl
Co-supervisor: Jostein Løwer
July 2023

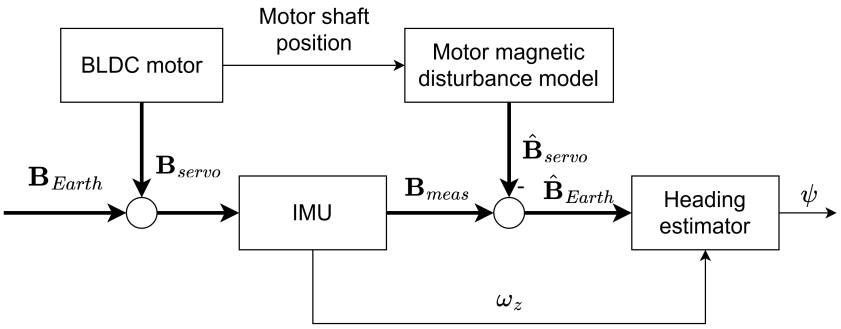

NTNU
Norwegian University of Science and Technology

Mari Linnerud

Heading estimation during motor-related magnetic disturbances

Master's thesis in Cybernetics and Robotics
Supervisor: Øyvind Stavdahl
Co-supervisor: Jostein Løwer
July 2023

Norwegian University of Science and Technology
Faculty of Information Technology and Electrical Engineering
Department of Engineering Cybernetics

NTNU
Norwegian University of
Science and Technology

NTNU
Norwegian University of
Science and Technology

Faculty of Information technology
Electrical Engineering
Department of Engineering Cybernetics

Master's Thesis

Student's name: Mari Linnerud

Field: Engineering Cybernetics

Title (Norwegian): Estimering av kursvinkel ved motorrelaterte magnetiske forstyrrelser

Title (English): Heading estimation during motor-related magnetic disturbances

Description:
Boa, a next generation sensor-driven snake robot, is currently under development at ITK. A previous student project investigated how magnetic disturbances affect the IMU measurements and demonstrated the viability of modeling the magnetic cross-talk from the motor to the magnetometers, thereby paving the way for model based noise reduction.

Recently the robot has been redesigned to use a new type of motor. This assignment aims at adapting the previous results to this motor and implementing improved heading estimation.

The work should include the following:

1. Adapt the magnetic crosstalk model to the new motor.
2. Assess the influence of varying motor load torque, which is highly correlated with current and magnetic flux density.
3. Consider and evaluate other physical and/or algorithmic measures to reduce the magnetic disturbance.
4. Assess the results in terms of heading estimation quality.

Advisor(s): Jostein Løwer
Øyvind Stavdahl

Trondheim, March 1, 2023

Øyvind Stavdahl
Supervisor

Preface

This master's thesis concludes my M.Sc degree in Cybernetic and Robotics with specialization in Autonomous Systems at the Department of Engineering Cybernetics at the Faculty of Information Technology and Electrical Engineering at the Norwegian University of Science and Technology. The master's thesis is an extension of the specialization project performed in the autumn of 2022. Some parts are therefore based on this project. The work was performed in the spring of 2023, and is entirely my own.

The code developed for this thesis can be found on GitHub with examples [1]. The part of the experimental test script controlling the servo motor is based on the "Python Read Write Protocol 2.0" example code provided by the `Dynamixel SDK` library [2, 3]. The code was greatly modified for the designed experiments. However, the general structure for communicating with the motor was based on the example code.

Due to the lack of a proper test rig, I had to design an experimental setup to emulate a rotational load on the motor. This was performed by using the auto-cad software Fusion 360 [4]. The home-made test rig was 3D-printed using a Prusa 3D printer [5].

Pandas was used to read the CSV files and plot the acquired data from the experiments [6]. Additionally Seaborn's `pairplot` was used as a starting point for the analysis of the data [7]. The Statsmodels's `tsa` module was used for the time series analysis to investigate if the noise should be modelled using an Auto Regressive and Moving Average (ARMA) model [8]. Lastly, Scipy's `optimize.curve_fit` was used to model the magnetic cross-talk from the servo motor [9, 10]. Figures were created using either Matplotlib, Inkscape, Google Drawings, draw.io or a combination of the aforementioned methods [11–14].

Mari Linnerud
Trondheim
July 13, 2023

Acknowledgements

Over the course of this thesis, there are several people that deserve to be acknowledged. The incredibly cool assignment would not have been possible without my supervisors, Jostein Løwer and Øyvind Stavdahl. Jostein especially, has given great support and guidance throughout the semester, even when he was under pressure to deliver his PhD.

Additionally, there are two technical organizations at NTNU that deserve to be thanked. I would like to thank Omega Verksted for letting me use your equipment and lab for the experiments, as well as for your bottomless fridge and candy shelf. I would also like to thank Orbit NTNU for letting me use their offices and equipment.

I would also like to thank to my friends for the coffee breaks, waffle Fridays, and long days at the office. Lastly my sister and PhD. Candidate in Physics, Marthe Linnerud, deserves my greatest gratitude for proofreading my entire thesis and giving me lots of tips on how to improve my writing.

Thank you all for your great support throughout the semester.
I could not have done this without any of you.

Abstract

Heading estimation is a challenging task in the presence of magnetic disturbances. For small vehicles with electric motors, such as a snake robot, heading estimation becomes extra challenging due to the induced electromagnetic field from the motors and magnetic materials in the environment. The Boa snake robot, currently under development at the Norwegian University of Science and Technology, was built to investigate novel methods for estimating contact forces and contact points for planar snake robots. To this end, the robot has an IMU fixed to each link. The magnetic cross-talk from the motors must therefore be addressed to enable accurate heading and attitude estimates.

In this thesis, the magnetic disturbance on the onboard IMUs induced by the robots' motors was assessed. The rotating magnetic field induced by the motors was found to be accurately modeled by a sinusoidal signal. The model was further tested and validated with additional motor load. Additionally, the effect of physical magnetic shielding was explored using ferrite shielding sheets and physical distance between the IMU and the motor. The experiments showed that physical distance and shielding sheets provided approximately the same magnetic field attenuation, but shielding sheets made the cross-talk more complex and the model less reliable. Lastly, a magnetic disturbance rejection technique using an adaptive Kalman filter was explored by performing a simple proof-of-concept heading experiment. The heading experiment showed that the heading estimates could be significantly improved using a cross-talk model as a predictor in a feed-forward loop to correct the magnetometer measurements. The heading can be estimated using a Kalman filter with an adaptive measurement covariance matrix to reject magnetic disturbances.

Hence, a general technique to improve heading estimates in the presence of electric motors and magnetically noisy environments was proposed. Future work includes testing the technique on a multi-link snake robot using obstacle-aided locomotion with full attitude and position estimation.

Sammendrag

Kursvinkelestimering er en utfordrende oppgave i nærvær av forstyrrelser fra magnetiske materialer. For små kjøretøy med elektriske motorer, som for eksempel en slangerobot, blir kursvinkelestimering ekstra utfordrende på grunn av det induserte elektromagnetiske feltet fra motorene, foruten å nevne mulige magnetiske materialer i omgivelsene. Slangeroboten Boa, som for øyeblikket er under utvikling ved Norges Teknisk-Naturvitenskapelige universitet, ble bygget for å undersøke en ny metode for å estimere kontaktkrefter og kontaktpunkter for slangeroboter. Roboten har derfor en IMU på toppen av hvert robotledd med børsteløse likestrømsmotorer.

Arbeidet i denne avhandlingen har undersøkt den magnetiske forstyrrelsen på IMU-en ombord slangeroboten, indusert fra motoren. Den magnetiske forstyrrelsen på magnetometeret ble modellert som en sinuskurve. Modellen ble videre testet og validert med ekstra belastning på motoren. I tillegg ble effekten av fysisk skjerming ved hjelp av ferrittskjermingsark og fysisk avstand testet og evaluert. Eksperimentene viste at fysisk avstand og skjermingsark ga omtrent samme magnetfeltredusering, men skjermingsark gjorde krysstalen mer kompleks og modellen mindre pålitelig. Til slutt ble en teknikk for å avvise magnetiske forstyrrelser ved hjelp av et adaptivt Kalmanfilter utforsket gjennom et enkelt dugelighetseksperiment for kursvinkelestimering. Eksperimentet viste at kursvinkelestimatene kan betydelig forbedres ved å bruke krysstalemodellen som en prediktor i en foroverkoblingssløyfe som korrigerer magnetometermålingene. Kursvinkelen kan estimeres ved hjelp av et Kalmanfilter som adaptivt endrer målekovariansmatrisen for å avvise magnetiske forstyrrelser.

Avslutningsvis ble det foreslått en generell teknikk for å forbedre kursvinkelestimatene i nærvær av elektriske motorer og magnetisk støyende miljøer. Det foreslås at fremtidig arbeid tester teknikken på en flerleddet slangerobot som bruker hinderassistert forflytning, med full bevegelses- og posisjonsestimering.

Contents

Acronyms

AC Alternating Current. 10

ACF Auto Correlation Function. 15, 28

ARMA Auto Regressive and Moving Average. v, 14, 22

AUV Autonomous underwater vehicle. 12, 22

BLDC Brushless DC. 1, 2, 10, 26, 32, 66, 79

DC Direct Current. 10

DQEKF Double Quaternion Extended Kalman filter. 21, 22, 77

EKF Extended Kalman Filter. 18, 22, 76

EMF Electromotive force. 9, 69, 70

I2C Inter-Integrated Circuit. 5, 13

IMU Inertial Measurement Unit. 1, 2, 12

IQR Interquartile range. 16

MDR Magnetic Disturbance Rejection. 34

MEMS Micro-electromechanical systems . 12

PACF Partial Auto Correlation Function. 15, 28

RMSE Root Mean Square Error. 14, 16, 68

UAV Unmanned aerial vehicle. 12, 22

Chapter 1

Introduction

The research of snake robots is ever expanding due to their promising applications in search and rescue operations, exploration of celestial bodies in the outer solar system, such as the Jovian moons, maintenance of oil platform and other scenarios [15] [16]. Snake robots may be especially suitable for search an rescue operations in ruins, or research in harsh environments. The navigation of autonomous robots is vital to the efficiency and reliability of the mission. The heading and attitude estimation problem for vehicles is however a difficult in magnetically noisy environments, since magnetometers are used, especially if the use of GPS is limited. Heading estimation becomes even harder for small vehicles with electric motors which generate an electromagnetic field, disturbing the magnetometer measurements. The problem remains challenging, even though extensive research has been conducted on the topic [17]. Improving heading estimation in the presence of magnetic disturbances is the main topic of this thesis.

1.1 Background and motivation

The Boa snake robot, currently under development at NTNU, is a sensor driven terrestrial snake robot. One of its intended uses is to test a novel technique to estimate the contact force between the robot and its environment [18]. To this end, an Inertial Measurement Unit (IMU) is mounted on top of each joint. Each joint contains a Brushless DC (BLDC) servo motor. Figure 1.1 displays an illustration of the design of the Boa snake robot with the previous motors and chassis design. The magnetic cross-talk from the motor must therefore be addressed to enable precise heading and attitude estimates.

Force sensors have historically been used to estimate the interaction forces between snake robots and obstacles in their environment. These are however prone to wear and tear [18]. To overcome this problem, the design of the Boa

Figure 1.1: Illustration of the previous design of the Boa snake robot with five links. Figure retrieved from Löwer *et al.* [18].

uses principles based on Newton's 2nd law to estimate the forces [18]. This led to the decision of adding the Inertial Measurement Unit (IMU)s on top of each motor joint. The IMU will be used to estimate the forces acting on each snake robot link by the obstacles, and are used in heading, attitude and spatial position estimation.

Research conducted in the autumn of 2022 investigated how the IMU measurements are affected by the servo motor. The main result was that the magnetic cross talk from the motor is accurately modelled by a sinusoidal signal [19]. Since the previous study, the Boa snake robot has been redesigned with a new set of Brushless DC (BLDC) servo motors. This work aims at continuing the previous work by concluding on unresolved work, and investigating to what degree it is possible to use the magnetic field measurements in heading estimation.

Good attitude and heading estimates in magnetically noisy environments are a challenge typically solved by high quality and expensive equipment such as GPS or high-quality IMUs. However, robots used in ruins or inside buildings, may not have reliable GPS connection. Additionally, reducing the cost of the snake robot is an objective in itself, to enable making a snake robot for commercial use. The snake robot should therefore be able to navigate, without the use of GPS or high-cost IMUs. This would be a big step in enabling large scale use of snake robots.

This work focuses on achieving good heading estimates for each individual link of the snake robot, which might also help with position and attitude estimates of the snake robot as a whole.

1.2 Assignment description and scope

The description of this assignment was outlined as a facsimile that can be found in the very beginning of this thesis. The main objective was to improve the heading estimation on the Boa snake robot, based on the results from the previous project work. Four main research points were outlined in the assignment description. The next paragraphs will describe how these have been interpreted by the author and incorporated into this work.

The first assignment point describes that this thesis should adapt the magnetic cross-talk model to the new motor. This was assessed by redoing the experiments performed in the previous project work, however improved and with the new motor. The second assignment point about the influence of varying load torque was assessed by performing the same experiment used to assess the first point, but using a test rig that emulated a rotational load. Other measures to reduce the magnetic disturbances were investigated by performing a literature review on algorithmic methods to improve heading estimates in magnetically noisy environments. Additionally, a series of experiments with magnetic shielding sheets and increased distance between the servo motor and the IMU was performed to analyse how effective these measures were in the context of heading estimation.

The last research point in the assignment captures the main objective to improve the heading estimation when the IMU was subject to the magnetic disturbance from the servo motor. This was done by proposing a technique based on the results from the previous steps. By further testing the technique in terms of a proof-of-concept heading experiment and compare it to the standard approach of heading estimation utilizing the same sensors, it would be able to assess the results in terms of heading estimation quality.

To limit the scope of the thesis, only one robot link was considered. Additionally, as the Boa is a planar snake robot, only the heading with respect to the sensors working in the 2D plane will be assessed. This means that the heading estimation does not need the accelerometer measurements, the gyroscope measurements along the x- or y-axis, or the z-axis magnetometer measurements. However, these sensors will be part of the work related to nominal IMU noise characterization, since it benefits the project as a whole when the full attitude estimates will be considered in the future.

A limitation to the assigned work was that the Boa link chassis was not available for the work, due to the previously mentioned redesign. The experimental setup was therefore limited by this fact. Additionally, the cross-talk model and heading estimation could only be assessed as seen in the IMU sensor frame, and the results therefore cannot be directly related to a Boa link. However, the method developed in this work can be redone once the Boa robot is operational.

1.3 Structure of the thesis

This thesis has been structure in the following manner to provide the results obtained by the work:

In Chapter 2, the theory needed to understand snake robots, electromagnetic fields in servo motors and the basic principles of IMUs will be described, as well as data analysis methods used to model the magnetic cross-talk from the motor. Additionally, the theory on heading estimation will be covered.

In Chapter 3, a literature review on previous work in the field is conducted as part of the method to investigate methods to improve the heading estimation. The chapter also introduces the reader to the previous project work on the Boa, which this thesis is a continuation of. It is presented before Chapter 4: *Method*, since it formed the basis of the experimental design.

In Chapter 4, the work was divided into five phases, and the experimental design to reach the objective of each phase described. The chapter also introduces the reader to the hardware under investigation during the thesis.

In Chapter 5, the results from the experiments will be presented and described. Additional observation from the experiments is also presented that should be assessed in future work.

In Chapter 6, the results are discussed, the previous work are validated, and a technique to improve the heading estimates when the servo motor's actuates are proposed based on the results. it further proposes future work to be conducted to test the proposed technique under more realistic conditions.

Chapter 7 concludes the work.

Appendix A provides large plots and additional numbers from the results.

Chapter 2

Theory

This chapter will introduce the main theory relevant to the thesis. It will include basic theory about snake robots and electromagnetic fields. Further, the theory goes into detail about electric motors before the basic principles of how IMUs work. Moreover, the reader will be introduced to the protocols critical in the experimental setup: RS-485 and Inter-Integrated Circuit (I2C). Further on, the basic principles of the data analysis methods used are presented. A section is also devoted to sine regression as this is an important part of modeling the magnetic cross-talk from the motor. Lastly, the theory on heading estimation and filtering techniques will be covered.

Note that almost every section is a direct citation from the theory chapter in the previous project work carried out in advance of this thesis [19]. Exceptions are minor changes in Section 2.2, the addition of Section 2.5.2 in Section 2.5, and greater changes in Section 2.6. Sections 2.6.2, 2.6.3, 2.8 and 2.9 are new.

2.1 Snake Robots

This section is based on the theory section of Pål Liljebäck's doctoral thesis [20]. Only the basic principles of snake robots, their basic structure, and how they propel through the environment will be described. This is done in order to capture the basic principles and terminology needed to understand the motivation behind the research of this thesis.

The general snake robot is composed of four different elements: links, joints, motors, and sensors. The front link is called the head. Figure 2.1 illustrates this basic principle. The sensors are needed for navigation. These could be but are not restrained to IMUs, force sensors, cameras, GNNS, and encoders. The servo motors are used as actuators to propel the snake robot. It could be used in either a wheel, a propel, or in the joint itself, based on the locomotion method of the snake robot.

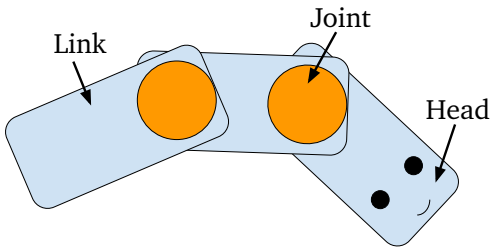

Figure 2.1: An illustration of a snake robot design. In addition to links, joint and a head, the snake robot has sensors distributed around the body of the robot.

A snake robot's propulsion method is inspired by biological snake locomotion [20]. Lateral undulation is the most common type of snake locomotion and is shown in Figure 2.2 [20]. The Boa snake robot project is researching a propulsion technique based on lateral undulation called obstacle-aided locomotion [18]. The snake robot uses lateral undulation against obstacles to propel itself in any given direction, utilizing Newton's second and third laws. Each joint is a servo motor, enabling the robot to move each link against obstacles and thus create a force to move in the desired direction. The reader is referred to *Liljebäck* [20] for mathematical details on the modeling of snake robots, as this is not relevant to this thesis.

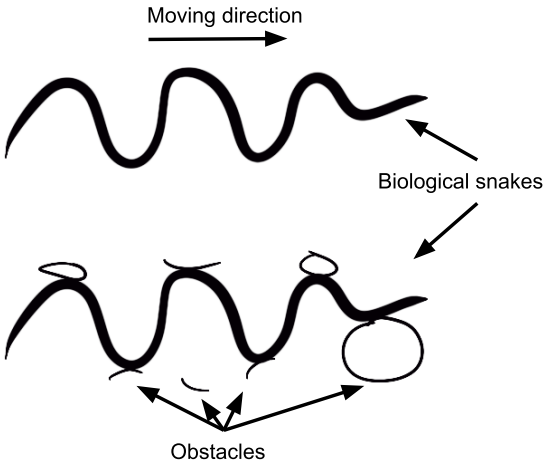

Figure 2.2: Illustration of two biological snake locomotion methods: lateral undulation (top) and obstacle-aided lateral undulation (bottom).

2.2 Electric and magnetic field theory

A basic understanding of dynamic electromagnetic fields is needed to understand how electric motors work and why sensors can be disturbed by an electric motor. The theory of static electric and magnetic fields will first be presented to more easily describe the theory of dynamic electromagnetic fields. Lastly, shielding of magnetic fields will be introduced. The entire section, except for subsection 2.2.4, is based on Sadiku and Nelatury [21].

2.2.1 Electrostatic fields

Electrostatic fields can be described in terms of Coulomb's law. Coulomb's law states that the force F between two point charges Q_1 and Q_2 acts along the line between the two point charges, with the strength given by

$$F = \frac{kQ_1Q_2}{R^2}, \tag{2.1}$$

where k is a constant, R is the distance between the two point charges and Q_1 and Q_2 are the size of the point charges. The electric field intensity, **E**, is the force that a unit positive charge experiences when placed in an electric field.

$$\mathbf{E} = \lim_{Q \to 0} \frac{\mathbf{F}}{Q} \tag{2.2}$$

Electric flux is measured in Coloumbs, and is defined as the amount of electric field passing through a given surface area. Thus, from the equations above, an electric field is a vector field that describes the force an electric charge experiences at a given point in the field.

2.2.2 Magnetostatic fields

Similar to electric fields, a magnetic field is a vector field that describes the force a moving electric charge experiences due to magnetism. A magnetic field can be induced by moving electric charges. Electric charges moving at a constant speed induces a static magnetic field, while electric charges moving at varying speeds will induce a dynamic magnetic field [21]. The force experienced by an electric charge in a static magnetic field is given by

$$\mathbf{F} = Q\mathbf{v} \times \mathbf{B} \tag{2.3}$$

where **v** is the velocity of the electric charge, **Q**, and **B** is the magnetic flux density.

However, in the presence of both an electric field and a magnetic field, **Lorentz law** states that an electric charge, Q, moving through the electric and

magnetic fields with velocity, **v**, experiences a force that is perpendicular to both fields, according to the right-hand rule. This force is called the Lorentz force [21].

$$\mathbf{F} = Q\mathbf{E} + Q\mathbf{v} \times \mathbf{B} \tag{2.4}$$

The magnetic field can either be described in terms of magnetic flux intensity, **H**, or by magnetic flux density, **B**, as described in equation (2.5) and Biot Savart's law in equation (2.7).

$$\mathbf{B} = \mu_0 H \tag{2.5}$$

The **magnetic flux** through a surface S is given by

$$\psi = \int_S \mathbf{B}\, dS \tag{2.6}$$

Biot-Savart's law states that the differential magnetic field intensity $d\mathbf{H}$, produced at a point P, by a current I, moving along a small line $d\mathbf{l}$, at a distance R from the point is given by

$$d\mathbf{H} = \frac{I\ d\mathbf{l} \times \mathbf{R}}{4\pi R^3} \tag{2.7}$$

This means that the magnetic field intensity at a point in a magnetostatic field depends on the current through a conductor and the distance to it.

The magnetic field around a permanent magnet and around a coil with constant current running through it is shaped as shown in Figure 2.3. One can see that they are similar. The magnetic field around a permanent magnet is induced by internal magnetic forces, while the magnetic field around the coil [1] is induced by a moving electric charge as given by Biot-Savart's law.

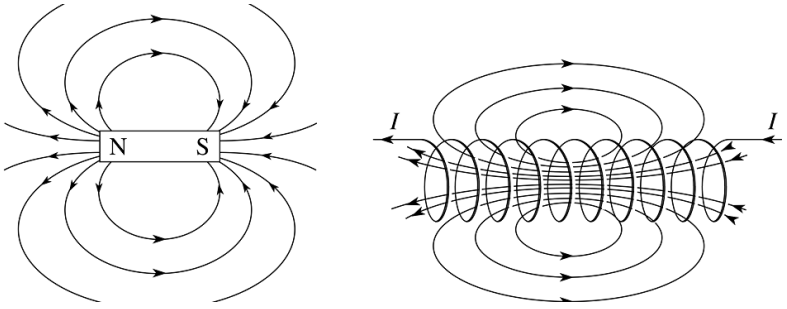

Figure 2.3: The magnetic field around a permanent magnet (left), and a coil with a constant current, I (right). Image retrieved from *Stanford Magnets* [22].

Magnetic fields can in most cases be assumed to be additive following the superposition principle [23].

[1] Also commonly called an electromagnet.

2.2.3 Dynamic electromagnetic fields

In dynamic electromagnetic fields, the electric and magnetic fields are interdependent of each other, as opposed to static fields where they are independent [21]. Dynamic electromagnetic fields can be made in three ways:

1. Having a time-varying loop in a stationary magnetic field
2. Having a time-varying magnetic field in a stationary loop
3. A combination of the above

As will be described in Section 2.3.1, these effects are utilized in electric motors.

Table 2.1: Summary of how electromagnetic fields are created. Table adapted from Sadiku and Nelatury [21]

Stationary charges	Electrostatic field
Steady currents (moving charges with constant velocity)	Magnetostatic field
Time-varying currents	Electromagnetic fields

Faradays' law states that if a closed electric loop experiences a changing magnetic field, it will induce an Electromotive force (EMF) proportional to the rate of change of the magnetic flux. **Lentz' law** further states that the direction of the current in the loop due to the electromotive force is such that it counteracts the change in magnetic field. This effects is what cause **eddy currents** in electrically conductive materials and the back emf voltage in DC motors.

2.2.4 Magnetic shielding

Magnetic fields cannot be stopped. It is however possible to contain or redirect the magnetic field using materials with high magnetic permeability [24]. Examples are ferrite shielding sheets or mu metals [25] [24]. This is called passive magnetic shielding, and can be accomplished by using permeable materials which contains the electromagnetic field [24]. Another passive shielding technique which is commonly used are electrically conductive materials [26]. When the shielding sheet is subject to a changing magnetic field, eddy currents will be induced following Faradays' and Lenz' law, and create an equal and opposite magnetic field, zeroing out the magnetic field. Eddy currents can therefore be used for dynamic magnetic fields only. For both methods, the performance of the shielding changes with frequency. It is therefore important to choose the correct material and thickness based on the data sheet of the shielding sheet.

2.3 Electric Motors

With the basics of electromagnetic fields covered, the principles of electric motors can be presented. The working principle of electric motors is based on the Lorentz force given in equation (2.4) [21]. By moving electrically charged particles through a conductor in a magnetic field, the Lorentz force will pull on the particles in the direction given by the right-hand rule and make the current loop rotate. The general design of electric motors will be presented in subsection 2.3.1. After that, the Brushless DC (BLDC) motor will be described in detail in subsection 2.3.2.

2.3.1 General structure of electric motors

An electric motor consists of a static element called the stator, and a rotating element called the rotor [27]. There exist several types of electric motors; synchronous Alternating Current (AC) motors, asynchronous AC motors, DC motors, and brushless DC motors, to name a few. Electric motors are built on armature windings consisting of one or several coils, and either permanent or electromagnets. Depending on the type of motor, the rotor could be the windings and the stator the magnets, or the other way around [27]. The relevant type of electric motor for this thesis is the Brushless DC motor.

The difference between a servo motor and a conventional electric motor is that the servo motor additionally has a control unit and encoders enabling the user to control the position of the motor, as opposed to only the speed [27]. The detailed theory behind servo motors is, however, above the scope of this thesis.

2.3.2 Brushless DC motors

The Brushless DC motor can have two configurations: either an outer ring rotor with permanent magnets and an inner ring stator with coils or an outer ring stator with coils and an inner ring rotor with permanent magnets. Figure 2.4 shows an illustration of both as three-phase motors. The BLDC motor is controlled by a control unit, providing current to each coil at a time as shown in Figure 2.4c. This sequence induces motion to the rotor. A hall effect sensor is used as feedback to the controller to change the direct current when the stator field is aligned with the stator field [27].

The most common type of BLDC motor is the 3-phase BLDC with three windings. The three stator windings are connected in a star connection, also called the Y-connection. Each winding can consist of one or more coils. The three windings are distributed over the stator to form an even number of poles [28]. The rotor consists of alternating north, and south pole permanent magnets [28]. According to *Yedamale* [28], the rotor pole pairs are constrained to be between two and eight pole pairs for 3-phase motors. A three-phase current is applied to

the three windings according to the current cycles shown in Figure 2.4c, creating a changing magnetic field which attracts the permanent magnets of the rotor. Other current cycles also exists. Thus, broadly speaking, electric motors utilize a strong magnetic field to function.

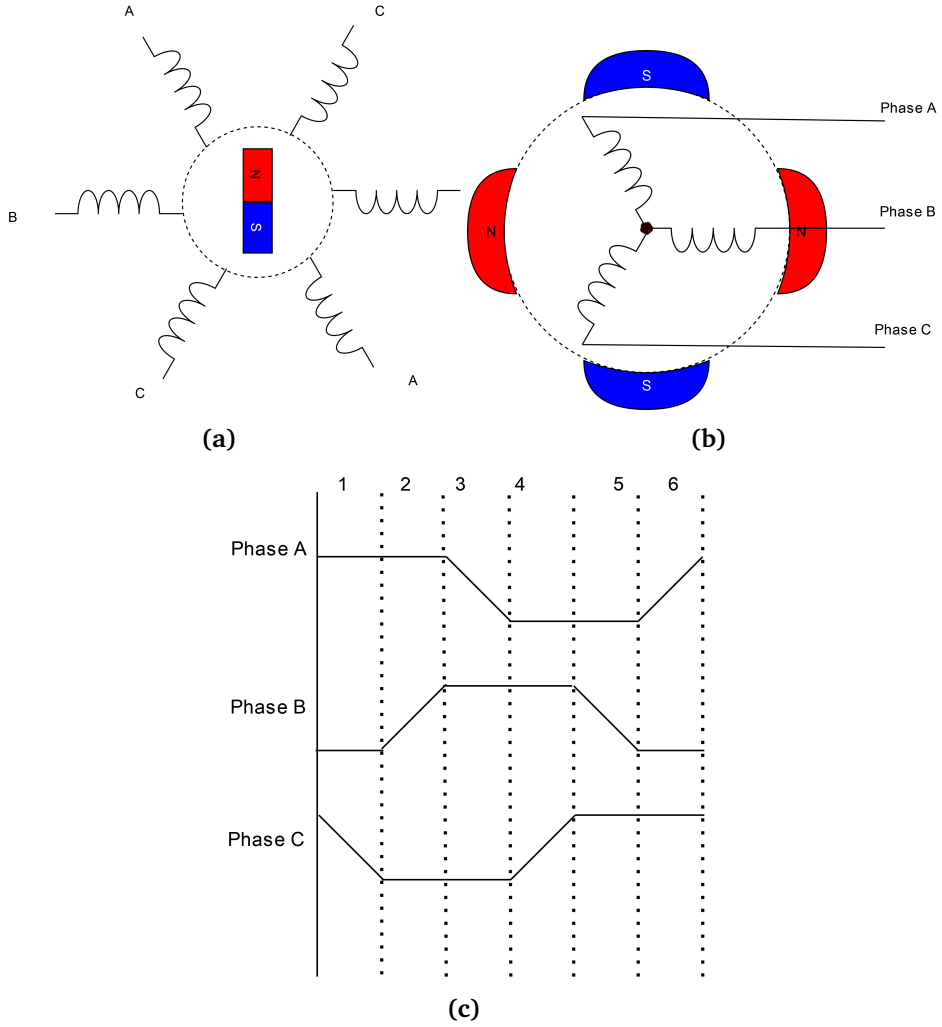

Figure 2.4: Illustration of how 3-phase brushless DC motors work. a) shows an inner ring stator with one pole pair. b) shows an outer ring stator with two pole pairs. c) shows an example of the trapezoidal three-phase current cycles that go through phases A, B, and C to make the rotor rotate.

2.4 Inertial Measurement Unit

An Inertial Measurement Unit (IMU) is a sensor essential to navigate unmanned vehicles such as satellites, robots, Unmanned aerial vehicle (UAV)s, Autonomous underwater vehicle (AUV)s, and snake robots, as well as guided control of cars and aircrafts. It consist of a 3-axis accelerometer, 3-axis gyroscope, and normally also a 3-axis magnetometer. The accelerometer measures specific force, while gyroscopes measure angular rate. Often, an IMU containing a magnetometer is also called a MIMU. In this thesis however, all references to an IMU contains both an accelereometer, a gyroscope and a magnetometer.

An image of a typical IMU is presented in Figure 2.5. IMUs are based on Micro-electromechanical systems (MEMS) technology. The most common type of MEMS inertial sensors are silicon-based. The technology enables large advantages related to cost, size, weight, and power consumption [29].

Figure 2.5: A typical IMU. Image retrieved from *Bosch* [30].

The most common types of MEMS accelerometers and gyroscopes both utilize a vibrating mass to measure the linear acceleration and angular velocity of an object [29]. The accelerometers are however in reality force sensors that measure the specific force. This means that an accelerometer in free fall will measure zero acceleration, while an accelerometer placed stationary on a table will measure $-9.81\,\mathrm{m\,s^{-2}}$ [31].

Three-axis magnetometers in IMUs are not necessarily MEMS technology. Magnetometers in IMUs are used to measure the Earth's magnetic field, often in order to measure an object's heading. Most magnetometers are either Hall-effect sensors or magnetoresistive sensors. Newer, more precise methods also exist. Overall, numerous different methods exist, utilizing different physical laws [32]. Common for them is that they measure the voltage difference either due to a change in resistance or the creation of an electric field due to a magnetic field [32] [33].

2.5 Communication protocols

Snake robots need a computing unit, such as a microcontroller, to be able to control the movements of the joints and sample data from the different sensors. To communicate with these peripheral units, different standardized communication methods are used. This section will give a brief introduction to the protocols used in this thesis, and the adequate information needed set up the communication between the units, since it is relevant to the experimental setup.

2.5.1 I2C

Inter-Integrated Circuit is a synchronous serial communication bus normally used for low speeds, and short distance communication [34]. The I2C protocol requires two lines: serial data where the data is transmitted and serial clock for synchronizing the two communicating devices. The voltage levels on the lines are either 3.3V or 5V. The standard speed of I2C is 100 kbit/s, while fast mode provides 400 kbit/s [34]. Each device on the I2C bus is allocated its own address. The address space is 7 bits, limiting the number of nodes communicating to 128 units [34].

The I2C protocol uses the master/slave convention, where one unit is assigned master, while all other devices are assigned the slave role. Multimaster is also possible [34]. There exist in-built libraries in programming languages, such as Python and Arduino to communicate over I2C.

2.5.2 RS-485

RS-485 is not per definition a communication protocol, as it does not specify signaling levels, speed or the format of the data transmission. It is however a standard in the physical layer of serial communication. The communication protocol used could be the UART standard, but often a unique protocol is used. RS-485 is good in electrically noisy environments, and can handle up to 1200 m distances. It uses differential signalling, and thereby has two data signals. The wires are commonly called A (or D+) and B (or D-). The recommended arrangement of serial communication transceivers are the daisy chain [35]

2.6 Data analysis methods

A basic understanding of correlation plots, Auto Regressive and Moving Average (ARMA) modelling and how to recognize White Gaussian Noise is needed to understand the data analysis performed on the experimental data. This section will introduce the reader to these data analysis methods.

2.6.1 Correlation and scatter plots

Correlation plots are, in general, the same as scatter plots, but with the intention of revealing systematic linear or non-linear patterns in a data set [36]. Correlation is a statistical property describing the linear relationship between two random variables, X, Y. The correlation coefficient is a measure between zero and one, which describes how correlated two features are. If the correlation coefficient is zero, it means that there is no correlation, and if it is one, it indicates a clear correlation. The correlation coefficient between two variables are proportional to the covariance between them, as defined by the correlation coefficient in Equation (2.8).

$$\rho_{X,Y} = \frac{\text{cov}(X,Y)}{\sigma_X \sigma_Y} \tag{2.8}$$

$$\text{cov}(X,Y) = E[(X - E[X])(Y - E[Y])] \tag{2.9}$$

where $\text{cov}(X,Y)$ is the covariance between X and Y, and σ_X, σ_Y are the standard deviations of X and Y respectively [36]. Note that in case of a nonlinear relationship, the correlation coefficient can be one [36]. For features with a nonlinear relationship, other fitness measures, such as the Root Mean Square Error (RMSE) or the residuals with the nonlinear curve can be used. These will be further described in Section 2.7.

2.6.2 ARMA modelling

Auto Regressive and Moving Average modelling is a time series analysis and modelling technique. The aim of time series analysis is to characterize the nature of the observed data, and evaluate if it is possible to predict future observations based on the analysis [37]. ARMA modelling is a common method used to model a univariate time series where there is a stochastic trend, or random variations over time. ARMA modelling can be used to model stationary timeseries such as stock market analysis, health data or to perform economic forecasting [38]. Ning *et al.* [39] modelled the magnetometer noise using an ARMA model to improve the magnetic field and heading measurements.

ARMA models combines two simpler structures: the Autoregressive (AR) and Moving Average (MA) models. The ARMA model is typically denoted as

ARMA(p, q), where p is the order of the AR part and q is the order of the MA part [38]. An ARMA model is defined as

$$Y_t = c + \sum_{i=1}^{p} \phi_i Y_{t-i} + \epsilon_t + \sum_{i=1}^{q} \theta_i \epsilon_{t-i} \tag{2.10}$$

where Y_t is the time series you are trying to forecast, c is a constant, ϕ_i are the parameters of the autoregressive part of the model, Y_{t-i} are the values of the time series at previous points in time, ϵ_t is the error term of the model, θ_i are the parameters of the moving average part of the model, and ϵ_{t-i} are the error terms at previous points in time. The model parameters can be estimated using least squares [38].

Choosing the appropriate order for the ARMA model determines the accuracay of the forecasting. This can be achieved by inspecting the Auto Correlation Function (ACF) and Partial Auto Correlation Function (PACF) plots of the time series data [38]. The basic principle is to investigate which time steps contains information about the next, which is exactly what auto correlation is. Auto correlation is defined as the correlation between a data sample, and the data sample in a previous time step. Let X_t be a time series. The auto correlation, ρ_k, at lag k is defined as

$$\rho_k = \frac{Cov(X_t, X_{t-k})}{\sqrt{Var(X_t)Var(X_{t-k})}} \tag{2.11}$$

One lag is the last time step, lag two is the second last time step, and so on. The partial autocorrelation at lag k is the autocorrelation between X_t and X_{t-k} that is not accounted for by lags 1 through $k-1$.

The ACF and PACF plots describes how much the next step in the time series can be described by the previous time steps. The goal is to find out at which lag the auto correlation is sufficiently close to zero, such that it does no longer holds information about the next time step. This is done by inspecting which lag first goes within the 95 % confidence interval, of the plot. An ARMA model of orders p and q has an autocorrelation and partial autocorrelation cutoff *after* lag p and lag q respectively [38].

2.6.3 Statistical measures

It can in many cases be sufficient to determine whether a time series is sufficiently close to a Gaussian distribution by statistical measures and visual inspection. One typical approach is to use skew and kurtosis as rough indicators of the normality of a data set [40].

The skew is a unitless measure which describes how symmetric the distribution of a data set is. It is a common rule of thumb that a skew less than 0.5 is approximately symmetric. The kurtosis describes the tailedness of the

distribution. The most common measure of the kurtosis was define by pearson. However, many statistical programming libraries use Fisher's definition of kurtosis, which more directly relates to the normal distribution [40]. This kurtosis measure is also called the excess kurtosis, which is simply Person's definition subtracted by three. An excess kurtosis of zero means that the distribution is gaussian, assuming the skew is sufficiently close to zero. The *Pandas* and *Scipy.stats Python* libraries both calculates the excess kurtosis [41] [42]. The literature is not consistent on at which range the data can be considered to be normal for the excess kurtosis. Some say ±1, others ±3.

If a discrete time series is Gaussian, and the autocorrelation is zero, meaning that the signal is considered as random, the time series can be assumed to be white [43].

For data sets originating from sensors, it is common to have outliers in the measurements. A common technique to identify and remove outliers is using a multiple of the Interquartile range (IQR) [36]. The method is called the IQR method, and the chosen multiple is referenced to as the *scale*. A scale of 1.5 is the normal rule to identify a sample as an outlier [36].

2.7 Sine regression

Sine regression is a data modeling technique used to fit data to a sine curve. The sine regression can be used as an estimator in cases where two variables are known to be correlated by a sine. One normal approach is to use nonlinear least squares. To solve nonlinear least squares one can use numerical optimization methods such as the Gauss-Newton method [44]. Matlab and Python both provide libraries/toolboxes to perform sine regression. In Python, it can be performed using *SciPy*'s `curve_fit` function in the optimization package [9]. In Matlab, one may use the `Sine Fitting toolbox` [45].

When fitting a data set to a nonlinear function, the model can be evaluated by analyzing the residuals between the estimated value at a point, and the real value. This error is called the residual [44]. The Root Mean Square Error is another normal fitness measure used to evaluate the model [46]. The RMSE is defined as the root of the mean of the square of the residuals, as described in equation (2.12).

$$RMSE = \sqrt{\frac{1}{N}\sum_{i=1}^{N}(\hat{y} - y)^2} \tag{2.12}$$

where $\hat{y}$ is the estimated value of y, using the regression model.

When evaluating the performance of the model, it is important to not only evaluate it based on the training set. The training set is the data set used to build the model. Instead, a test set should be used. By applying the estimator on the test

set, and calculating the RMSE and residuals, one can validate the model [47]. In many data analysis and modelling techniques, it is normal to split the data set into a training set, a test set and a validation set. The test set is then used to state the model order. However, since sine regression with only one sine technically do not have a model order, the test and validation step is fused.

2.8 Heading estimation

In this section, the concept of heading estimation will be explained. It focuses on the 2D plane only, as the Boa is a planar snake robot.

The heading of a body is defined as the clockwise angle from north [48]. One can either use the range between 0° and 360°, where 0°, 90°, 180° and 270° is north, east, south and west respectively. In control, the range from $-\pi$ to π is often used, as it avoids sudden changes in the values. The heading can be calculated by a three axis magnetometer measuring earth's magnetic field. Equation 2.13 shows the calculation in the planar case, where B_x and B_y are the X- and Y- axis magnetometer measurement respectively [39]. Note that this equation uses radians. Figure 2.6 illustrates the calculation.

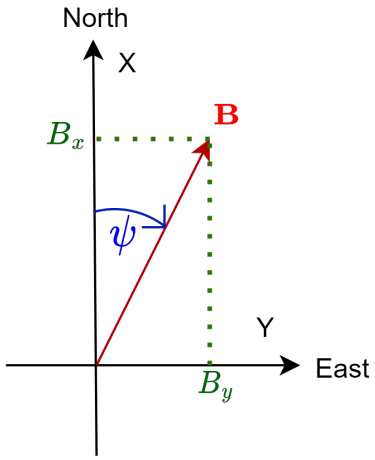

Figure 2.6: The heading can be calculated from the magnetometer's x and y-axis measurements by $\psi = \arctan(\frac{B_y}{B_x})$

$$\psi_{\mathrm{m}} = \begin{cases} \arctan\left(\frac{B_y}{B_x}\right) & \text{if } B_x > 0, \\ \arctan\left(\frac{B_y}{B_x}\right) + \pi & \text{if } B_x < 0 \text{ and } B_y \geq 0, \\ \arctan\left(\frac{B_y}{B_x}\right) - \pi & \text{if } B_x < 0 \text{ and } B_y < 0, \\ +\frac{\pi}{2} & \text{if } B_x = 0 \text{ and } B_y > 0, \\ -\frac{\pi}{2} & \text{if } B_x = 0 \text{ and } B_y < 0, \end{cases} \tag{2.13}$$

The different cases is to ensure the heading is in the correct quadrant. This is easily programmed in most programming languages using the *atan2* function. The heading estimate also needs to add what is called magnetic declination angle, which in the magnetic component. Magnetic declination angle is a constant covering the variation in earth's magnetic field around the world, and can be calculated using in example the World Magnetic Model [48].

$$\hat{\psi} = \hat{\psi}_m + \delta \tag{2.14}$$

where δ is the magnetic declination angle.

The heading can also be estimated by integrating Z-axis gyroscope measurements (in the 2D-plane), assuming the initial heading is known. Gyroscope samples are discrete values. Let ω_k and $\hat{\psi}_{m,k}$ be the gyroscope measurement and known heading estimate at time step k. The heading estimate at the next time step of size dt, can then be calculated by

$$\hat{\psi}_{k+1} = \hat{\psi}_k + \omega_k dt \tag{2.15}$$

The problem with gyroscope measurements is that they have a constant bias. When integrating over this bias, the heading estimation will drift. The magnetometer measurements are, however, prone to external magnetic fields, or electric current generating electromagnetic noise, which in turn affects the heading calculation [48]. To overcome these challenges, the heading can be estimated using sensor fusion techniques, such as the Kalman Filter described in Section 2.9. This way, the measurements can correct each other.

The heading estimate from inertial sensors such as the magnetometer and gyroscope is often called a digital compass. In the aviation industry, a typical digital compass has an accuracy of ± 1° when level, and ± 3° when tilted [48].

2.9 The Kalman Filter

The Kalman filter is a recursive filter used in sensor fusion to estimate the state of a dynamic system [49]. The Kalman filter can be used to estimate states with noisy measurements, both when the state can be measured directly, and when it needs to be calculated by transfer functions describing the dynamic system [49]. The Kalman Filter assumes the system model is observable, that the noise is white, and that the transfer function is linear. Modifications to the standard Kalman Filter, such as the Extended Kalman Filter (EKF), can handle non-linear dynamic systems [43]. As the measurements are sampled at discrete time steps, the discrete-time Kalman Filter is used in most practical applications.

The Kalman Filter essentially consists of only two steps: the prediction step, and the update step [43]. In the prediction step, the Kalman filter estimates the

future state of the system based on the previous state estimate and the system dynamics. Assume the system dynamics are described by

$$\mathbf{x}_k = \mathbf{F}x_{k-1} + \mathbf{v}_{k-1} \tag{2.16}$$
$$\mathbf{v}_{k-1} \sim \mathcal{N}(0, \mathbf{Q}_{k-1}) \tag{2.17}$$

where $\mathbf{x}_k$ is the state at time step k, $\mathbf{F}$ is the state transition matrix, and $\mathbf{v}_{k-1}$ is white process noise with covariance $\mathbf{Q}_{k-1}$. Further, assume the measurement model is

$$\mathbf{y}_k = \mathbf{H}\mathbf{x}_k + \mathbf{w} \tag{2.18}$$
$$\mathbf{w} \sim \mathcal{N}(0, \mathbf{R}) \tag{2.19}$$

where $\mathbf{y}_k$ is the measurement at time step k, $\mathbf{H}$ is the measurement matrix, and $\mathbf{w}$ is white measurement noise with covariance matrix $\mathbf{R}_k$. The prediction equations are as follows

$$\hat{\mathbf{x}}_{k|k-1} = \mathbf{F}_k\hat{\mathbf{x}}_{k-1} \tag{2.20}$$
$$\mathbf{P}_{k|k-1} = \mathbf{F}_k\mathbf{P}_{k-1}\mathbf{F}_k^T + \mathbf{Q}_k \tag{2.21}$$

where $\hat{\mathbf{x}}_{k|k-1}$ is the predicted state estimate, and $\mathbf{P}_{k|k-1}$ is the predicted error covariance matrix at time k.

In the update step, the Kalman filter corrects the state estimate based on the available measurements. The update equations are

$$\mathbf{K}_k = \mathbf{P}_{k|k-1}\mathbf{H}_k^T(\mathbf{H}_k\mathbf{P}_{k|k-1}\mathbf{H}_k^T + \mathbf{R}_k)^{-1} \tag{2.22}$$
$$\hat{\mathbf{x}}_k = \hat{\mathbf{x}}_{k|k-1} + \mathbf{K}_k(y_k - \mathbf{H}_k\hat{\mathbf{x}}_{k|k-1}) \tag{2.23}$$
$$\mathbf{P}_k = (\mathbf{I} - \mathbf{K}_k\mathbf{H}_k)\mathbf{P}_{k|k-1} \tag{2.24}$$

where, $\mathbf{K}_k$ is the Kalman gain, $\hat{x}_k$ is the updated state estimate, and $\mathbf{P}_k$ is the updated error covariance matrix at time k [43].

The Kalman filter has two tuning parameters: the process noise and measurement noise covariance matrices. The process noise covariance matrix, $\mathbf{Q}_k$ represents the uncertainty in the system dynamics, while the measurement noise covariance matrix, $\mathbf{R}$, captures the uncertainty in the sensor measurements. Proper initialization and tuning of these covariance matrices are essential for accurate state estimation [43].

Algorithm 1 describes the Kalman Filter algorithm in pseudo code. The Kalman filter first needs to be initialized with the initial state estimate $\hat{\mathbf{x}}_0$ and the

initial error covariance matrix $\mathbf{P}_0$ based on prior information. This is important as a bad initial estimate can lead to divergence of the filter.

The process covariance matrix, $\mathbf{Q_k}$, must be discretizted, and depends on the time step Δt. This is done using Van Loan's formula, assuming a contunious-time linear process $\mathbf{\dot{x} = Ax + Bu + Gn}$:

$$\exp\left(\begin{bmatrix} -\mathbf{A} & \mathbf{GDG}^T \\ \mathbf{0} & \mathbf{A}^T \end{bmatrix} \Delta t\right) = \begin{bmatrix} \times & \mathbf{V_2} \\ \mathbf{0} & \mathbf{V_1} \end{bmatrix} \tag{2.25}$$

$$\mathbf{Q_k} = \mathbf{V_1^T V_2} \tag{2.26}$$

Algorithm 1 Kalman Filter Algorithm

Input: $\mathbf{F}$: State transition matrix, $\mathbf{H}$: Measurement matrix, $\mathbf{Q}_k$: Discrete process noise covariance matrix, $\mathbf{R}$: Measurement noise covariance matrix, $\mathbf{y}_k$: Measurement vector
Output: $\hat{\mathbf{x}}$: Final state estimate
Initialization: $\hat{\mathbf{x}}_0$: Initial state estimate
$\mathbf{P}_0$: Initial error covariance estimate
for each time step k **do**
$\hat{\mathbf{x}}_{k|k-1} = \mathbf{F}\hat{\mathbf{x}}_{k-1}$ ▷ State prediction without control input
$\mathbf{P}_{k|k-1} = \mathbf{F}\mathbf{P}_{k-1}\mathbf{F}^T + \mathbf{Q}_k$ ▷ Error covariance prediction
$\mathbf{K}_k = \mathbf{P}_{k|k-1}\mathbf{H}^T(\mathbf{H}\mathbf{P}_{k|k-1}\mathbf{H}^T + \mathbf{R})^{-1}$ ▷ Kalman gain
$\hat{\mathbf{x}}_k = \hat{\mathbf{x}}_{k|k-1} + \mathbf{K}_k(\mathbf{y}_k - \mathbf{H}\hat{\mathbf{x}}_{k|k-1})$ ▷ State update
$\mathbf{P}_k = (\mathbf{I} - \mathbf{K}_k\mathbf{H})\mathbf{P}_{k|k-1}$ ▷ Error covariance update
end for

Chapter 3

Literature review

The literature review aims to investigate how other researchers in the field has overcome magnetic disturbances in heading and attitude estimation. The main topics of interest in the search, were how disturbances from electric motors were managed, magnetic disturbance rejection, and heading estimation. This chapter also includes a section on the project work performed in advance of this thesis.

3.1 Improved heading estimation in magnetically noisy environments

Achieving good heading and attitude estimates in environments with external magnetic disturbances has been a thoroughly examined topic, due to its complexity. As described in the theory, magnetic fields cannot be directly shielded, and external magnetic fields must therefore either be handled by software or redirected through metals with high magnetic permeability.

Wondosen *et al.* performed a comprehensive literature search in advance of the development of their improved attitude and heading estimation using what they called the Double Quaternion Extended Kalman filter (DQEKF) [17]. A common technique to overcome magnetic disturbances described in the paper, is by detecting the magnetic disturbance and rejecting the measurement by increasing the measurement noise covariance matrix for the magnetometer data, making the filter update the estimates based on data from more reliable sources. The key takeout from Wondosen *et al.*, is that multiple approaches to accurate heading and attitude estimation has been researched, yet, accurate and reliable heading estimates in magnetically noisy environments remains a problem. Wondosen *et al.* therefore proposed to decouple the attitude and heading estimation, preventing the inaccuracy in the heading estimates from the magnetic disturbance to propagate into the attitude estimates [17]. The heading estimates were improved by detecting magnetic disturbances and rejecting these

measurements before feeding them into the EKF. The detection algorithm worked by creating a rule, based on the error between the expected measured magnetic field at time step k, H_k, and the measured field, B_k, calculated as $d_m = \sum_{k-n}^{k}(|H_k| - |b_k|)^2)$ [1]. The results showed that the DQEKF performed better than the standard EKF when the magnetic disturbance rejection algorithm was employed to both methods [17].

Widey and Woo suggested a robust attitude estimation technique using an adaptive Kalman filter for UAVs [50]. In addition to magnetic disturbance detection and rejection from the environment, the method proposed in the paper specifically handles the magnetic noise from the motors on the UAV. The improved attitude estimation method introduced a few design changes to the standard Kalman Filter, whereas those relevant to the heading estimation will be presented next. The first design change managed magnetic distubrance detection and rejection. After the magnetometer has been calibrated, the norm of the measurement should not change in the case of no magnetic disturbances, as the earth's magnetic field norm is constant [50]. Thus, the rejection rule was that if the magnetometer norm deviates with a threshold from the initial magnetic field norm, the magnetometer measurement should be discarded, and thus not used in the update step of the Kalman Filter. The second design change specifically handled the interference from the thruster motors. The magnetic interference follows a periodic sine function proportional to the motors' speed. When the rpm is sufficiently higher than the dynamic rotation of the AUV, the disturbance from the motor's could be easily filtered by adaptively increasing the measurement noise covariance matrix. In their case, the magnitude of the magnetic disturbance was in the range of $10\,\mu$T. The last design change handled the magnetic disturbance which does not change the norm of the measured field, but the direction. Widey and Woo handled this by linearly increasing the measurement covariance matrix with the scaled difference between the predicted attitude and the measured attitude [50].

Laslty, Ning *et al.* had a more complex approach to improving the attitude estimation, and will therefore not be covered [39]. However, the authors saw the need to model the measurement noise using an Auto Regressive and Moving Average model.

To summarize, the literature review shows that magnetic disturbances in heading and attitude estimation can be handled by different magnetic disturbance and rejection techniques. Additionally, in the cases where the disturbance originates from known electric motors, the disturbance can be filtered if the dynamics of the disturbance is sufficiently larger than the dynamics of the system. Lastly, attitude estimates can be improved by decoupling the heading and attitude estimates to prevent the reduced heading accuracy due to magnetic fields from leaking into the attitude estimates.

[1] The rule was however not specified

3.2 Previous work on the Boa Snake Robot

Initial investigation of the Boa snake robot's servo motors and IMU were performed in the project work preceding this master's thesis. The work was focused on understanding to what extent the electromagnetic field induced by the servo motors would affect the IMU measurements on the robot [19]. Since then, the hardware on the Boa has been upgraded, and the servo motor changed from the *RMD-X6 1:6* to the *Dynamixel XH540-V150-R* [51] [52]. The results from the project work can therefore not be used directly in this thesis. However, the conclusion forms the base foundation for the method and experimental design in this thesis.

By designing a test rig based on the Boa snake robot design, and performing an experiment where the servo motor shaft rotated 30° three times while the motor and IMU themeselves never moved, the previous work was able to map out how the servo motor's generated magnetic field affects the IMU measurements. The main results showed that the gyroscope was unaffected by the induced magnetic field, and that the accelerometer variance increased significantly in the z-direction when the servo motor shaft rotated. However, the work could not conclude why, as the data collected was not sufficient for mapping out the potential relation between the increased variance and either the motor's shaft speed, position or torque current. It was hypothesised that there could be a relation with the motor's shaft speed, but a conclusion could not be made due to a lack of data points as the shaft acceleration was much higher than the sampling frequency. The increased variance could also have been due to vibrations in the motor. It was therefore recommended for future work to improve the experimental setup.

The most important result from the previous work showed that the magnetometer measured the magnetic field induced by the servo motor, in addition to the earth's magnetic field. It was concluded that the magnetic cross-talk from the motor to the IMU could be modelled as a sine function against the motor's shaft position. Furthermore, it was suggested that by estimating the generated motor field by sine regression, it might be possible to predict the motor's magnetic field contribution and subtracting the contribution by using feed-forward before feeding the magnetometer measurements into a Kalman Filter [19].

Chapter 4

Method

The investigation of how to improve the heading estimates of the Boa Snake robot involved a systematic approach divided into four main phases:

Phase 1: Literature review laying the foundation of the design of the next three phases. It was therefore presented in Chapter 3.

Phase 2: IMU noise characterization by performing time series analysis of raw IMU measurements without magnetic disturbance from the servo motor. This phase also utilised data from the experiments performed in phase 3.

Phase 3: Motor actuation experiments to investigate the cross-talk from the motor. The IMU was mounted on top of the servo motor as by the Boa Snake robot design, while the motor shaft rotated and the servo motor and IMU themselves did not move (Figure 4.2). The experiment was also performed with an emulated rotational load. Physical shielding methods were also tested to investigate if it could improve the magnetic field measurement.

Phase 4: Motor field disturbance modelling Using the experimental data from the baseline and additional load experiments, and sine regression, a model of the magnetic disturbance from the servo motor in the sensor frame was made.

Phase 5: Proposal of a improved heading estimation technique using feed-forward and magnetic disturbance detection and rejection. The design was tested by a a proof of concept experiment and heading estimator.

The sections in this chapter describes the experiments performed in the four steps in further detail. However first, the hardware and experimental setup will be introduced.

4.1 Hardware introduction

The main hardware components in investigation is the servo motor and IMU of the Boa snake robot. These will therefore be described in further detail in this section, together with the baseline hardware setup similar in all experiments.

The IMU and servo motor of the Boa Snake Robot are displayed in Figure 4.1. The *BNO-055* is a smart sensor from Bosch, with tri-axis accelerometer, gyroscope and magnetometer. The *BNO-055* performs internal sensor fusion estimates of the attitude in quarternions or euler angles, linear acceleration and gravity in the sensor frame, using the sensors' raw measurements [30]. The IMU is auto-calibrated by performing a set of predefined movements [53]. The *Dynamixel XH540-150V-R* is a BLDC servo motor from Robotis, allowing both position and velocity control. It is controlled by a command set over RS-485 serial communication [52]. Robotis provides the *Dynamixel SDK* package in several programming languages, including C/C++, Python and MatLab. This allows easy control of the *Dynamixel* motor family [2]. All references throughout this thesis to "the IMU" or "the BNO" refers to the *BNO-055*, while references to "the servo motor", the "motor" or "the Dynamixel" refers to the *Dynamixel XH540-V150-R*.

(a) Image by from Robotis [52].

(b) Image by Adafruit [54].

Figure 4.1: The main hardware of the Boa Snake Robot under investigation in this research are a) the *Dynamixel XH540-V150-R* servo motor, and b) the *BNO-055* IMU on a breakout board from Adafruit.

4.2 Baseline experimental setup and variations

The baseline hardware setup was similar for all the different experiments that was conducted in the different phases, however with slight variations. On the Boa Snake Robot, the *BNO-055* IMU will be mounted on top of the servo motor, which acts as a motor joint in each motor link. The chassis holding the robot link hardware was unfortunately not available at the time of writing. A good enough solution was therefore to secure the IMU (on a breadboard) to the top of the servo motor by using double sided tape. During the experiments, the servo motor was

secured to the table with a clamp. The motor shaft was outside the table to allow the shaft to rotate freely. This way, the IMU and servo motor itself could not move during the experiment after IMU calibration, making the results easy to interpret. The experimental setup with variations are shown in Figure 4.2. The baseline setup shown in Figure 4.2a served as the starting point for all the experiments. The different variations for the experimental setup during the additional load and shielding experiments will be further detailed in Sections 4.4.2 and 4.4.3.

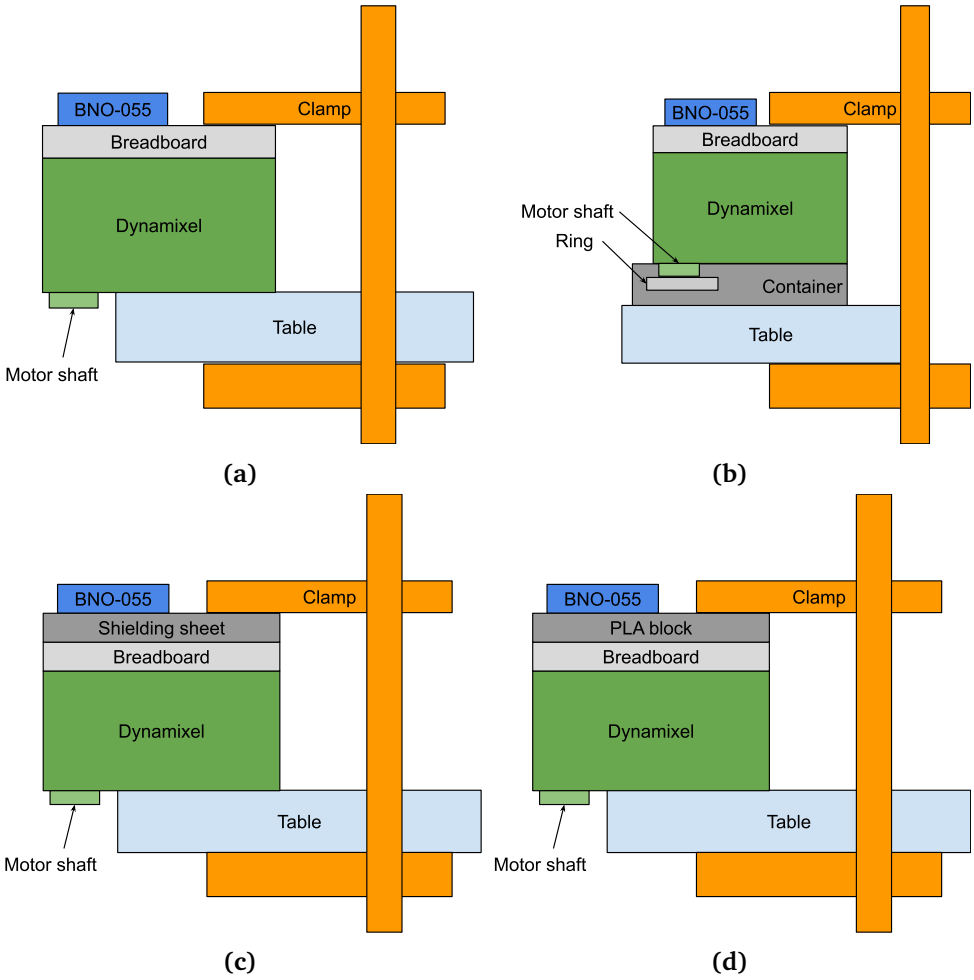

Figure 4.2: The experimental setup during a) the baseline servo experiment, b) the additional load experiment, c) the shielding experiment, and d) the distance experiment. The *Dynamixel* servo motor was clamped to a table, while the motor shaft was was outside the table, to ensure it could rotate freely while the motor itself remained stationary. The only exception was during the experiment with additional load, where a container was used to create a friction force adding load on the motor shaft. The *BNO-055* IMU was mounted on a breadboard on top of the motor.

Figure 4.3 shows the electrical interfaces in the experimental setup. The *Raspberry Pi* was chosen as the controller for the experiments. It is easy to use, has USB ports allowing easy serial communication with the *Dynamixel* through a USB-to-RS485 cable, and supports I2C communication with the *BNO-055*. The data from the IMU and the servo motor was saved as a CSV file on the *Raspeberry Pi*. The *Dynamixel* was powered by an external power supply. The *BNO-055* was powered through the *Raspberry Pi's* 5 V pin, and communicated over I2C. The *Raspberry Pi* itself was powered through a USB-C power supply.

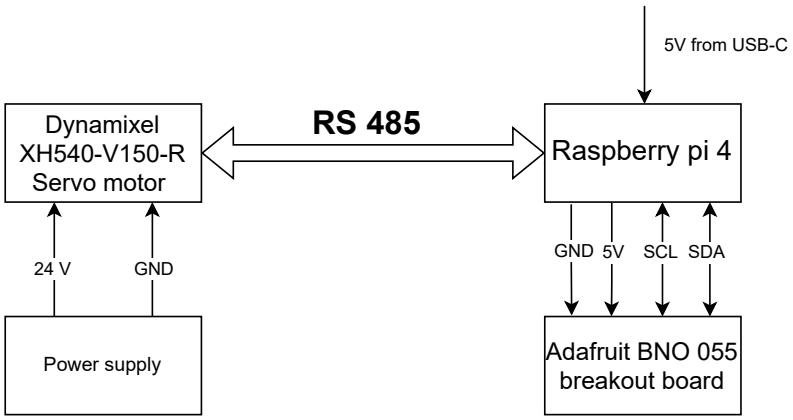

Figure 4.3: Schematic of the electrical interfaces in the baseline experimental setup. The *Raspberry Pi*, used as the main computer during the experiments, powered the *BNO-055* IMU and communicated over I2C. The *Dynamixel* servo motor was powered by an external power supply, and was controlled by the Raspberry Pi through serial communication over a RS4 85-to-usb-cable.

4.3 Nominal magnetometer noise characterization

Building upon the insights gained from the literature review in Chapter 3, the second phase aimed to characterize the natural measurement noise of the IMU. To investigate if the magnetometer measurement noise of the Boa snake robot should be modelled as an ARMA series, as Ning *et al.* suggested [39], it was decided to perform a dedicated time series analysis on the magnetometer measurements. The hardware setup was as sketched in Figure 4.4. The *BNO-055* IMU was wired to a *Raspberry Pi 4*, and placed flat on the table. A Python script was written that calibrates the IMU, and samples IMU measurements for 15 minutes. The time series analysis involved plotting the ACF and PACF plots to look at the autocorrelation of the time series, as described in Section 2.6.2 in the theory. Additionally, the skew, kurtosis and standard deviations of the measurements were investigated. The results are provided in Section 5.1, and discussed in Section 6.1.1.

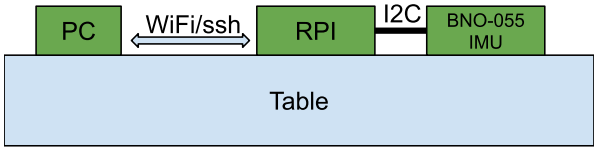

Figure 4.4: Setup during magnetometer noise characterization sampling. The power supply lines are not displayed for simplicity.

4.4 Servo motor actuation experiments

The third phase involved a series of servo motor experiments, inspired by the proceeding project work [19], as referenced in the literature review. The experiments conducted rotated the motor shaft at different speeds while the motor itself remained stationary. The experiments were performed both without and with additional load, and used the same test script. Raw IMU measurements where also sampled before and after the servo actuation. The primary objective was to develop a model of the magnetic disturbance caused by the servo motor on the magnetometer in the *BNO-055*. Additionally, two physical magnetic field reduction methods were evaluated with the same experimental setup: shielding sheets and physical distance. The goal was to explore the potential combination of software and hardware approaches to improve the accuracy of the magnetic field measurements. The modelling part of the third phase is described in Section 4.5.

The experiment was designed to achieve the following objectives: 1) Verification of the results obtained in the project work, 2) Building a model of the magnetic field disturbance generated by the servo motor 3) investigating how a changing motor load might impact the validity of the motor field model, and 4) explore physical techniques to reduce the magnetic field disturbance. The raw IMU measurements collected before and after servo actuation was used in phase 1 to find the nominal gyroscope and accelerometer noise. All these experiments were conducted using the same baseline hardware setup and test script, detailed in Sections 4.1 and 4.4.1, however with slight variations.

4.4.1 Test script development

The software script, used in almost all of the experiments, was designed as an improvement of the experiments performed by Linnerud in the previous project work [19]. The experiment designed in the previous project work were concluded to not have enough data points through the entire velocity span due to the high acceleration of the servo motor, making it harder to interpret correlations in the data set. It was however very suitable for modelling the magnetic disturbance as a function of the servo motor shaft position. The new test script design therefore aimed to ensure there were enough data points at the expected possible shaft velocities and positions of the Boa Snake Robot.

The motor actuation test script was programmed following the flowchart in Figure 4.5, and can be found on GitHub [1]. First, the IMU is initialized, and the serial communication ports are opened. Second, the IMU is calibrated by moving the IMU in a defined movement. Here, the user inputs if the IMU is calibrated or not until the calibrations status is good. Once the IMU is calibrated, raw IMU measurments are sampled for two minutes. After that, the servo motor is set to position control mode, the maximum acceleration set to 1072.9 $\mathrm{rev/min^2}$ and the torque is enabled. Then, the script enters the test loop, where the motor rotates the shaft clockwise from 0° to 360° and back to 0° counterclockwise with five evenly spread speeds between 5.7 and 41.2 rpm, while sampling IMU data. Lastly the torque was disabled and raw IMU measurements were sampled for two more minutes while the motor is not turned on. The reason for sampling IMU measurements both before, during and after servo actuation was to see if the magnetic field generated from the servo motor invalidates the IMU calibration.

In addition to sampling the raw IMU measurements, the calculated orientation estimated by the internal sensor fusion algorithm on the *BNO-055* was sampled and stored during the servo motor movements. The IMU was configured to display the orientation from the true north, and not the relative orientation from initialization. The test script was used for all the experiments performed, except the nominal magnetometer noise characterization sampling.

For the experiments performed in phase 3: motor actuation experiments, the user ensured the servo motor and IMU was secured to the table after IMU calibration, to allow the motor shaft to rotate while the servo motor and IMU themselves remained stationary, as shown in Figure 4.2.

4.4.2 Adding load

To investigate how the electromagnetic field generated by the servo motor change with servo motor torque load, a test rig was designed to simulate torque and friction forces, while keeping the servo motor stationary oriented. This is important as the snake robot will use friction forces against obstacles to move, adding torque load on the motor, which increases the torque current.

A proper test rig to measure or control the actual motor load was not available. The best solution was therefore to design a simple test rig using Fusion 360 and a 3D-printer [4]. The design is shown in Figure 4.2b. To simulate the additional load, the baseline hardware setup was modified. A 3D printed disk with additional weight was mounted on the motor shaft to apply additional torque to the rotation. Friction forces was simulated by applying a force between the disk, and a container with a pocket that the disk and shaft could be pressed against using the clamp. The force creating the friction was during this experiment made by the clamp securing the servo motor to the table in a stationary position. The experiment was otherwise identical to the baseline

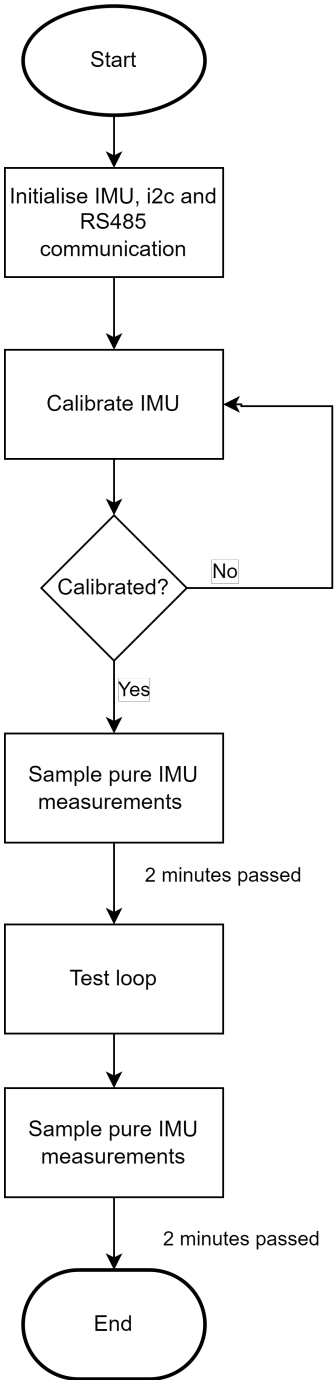

Test loop pseudo code

```
set servo operating mode to position mode
set max acceleration
enable torque
led on
for vel in np.linspace[5.725, 41.22, 5] rpm:
 maxVel  <-- vel
 for pos in [0, 360] degrees:
  goal_pos <-- pos
  while not in goal pos:
   read servo data
   read IMU data
save data to csv file
disable torque
led off
```

Figure 4.5: Flowchart of the test script used during the servo actuation experiments. The IMU auto calibrates by moving the IMU in a set of movements [53]. The servo motor was programmed using the Dynamixel SDK package [2]

experiment described in Section 4.1 and 4.4.1. As will be discussed in Section 6.2.3, the servo rotated a few degrees during actuation due to the friction forces between the motor and the container, and the fact that the clamp could not secure it completely.

4.4.3 Shielding experiments

In order to investigate if the heading estimates could benefit from using shielding materials around the servo motor, a series of the servo actuation experiments described in Section 4.4 were conducted with 1) physical shielding, and 2) a distance between the IMU and the servo motor. The purpose of the experiments was to compare how well the shielding could contain the magnetic disturbance from the servo motor, and compare the results to the reduced disturbance from simply moving the IMU away from the motor. The second objective of the experiment was to investigate if the filtering techniques would perform better with shielding or distancing.

Figure 4.2c and 4.2d visualizes the hardware setup in these experiments. The shielding sheet that was used was the self-adhesive *Wurth Elektronik Ferrite Shielding Sheet* with 0.1 mm thickness [25]. The physical distance between the IMU and servo was along the rotational axis of the servo motor, which is out of the plane. The motor could not move during any of the experiments, and the IMU was calibrated before each experiment, as follows from the test script flow in Figure 4.5. The experiment can be divided in three categories:

Reference experiment without shielding or additional distance between the IMU and the servo motor.

Ferrite shielding sheets between the servo motor and the IMU of thicknesses 0.1 mm, 0.3 mm, 0.3 mm in addition to 0.1 mm around the servo motor, and 0.5 mm in addition to 0.1 mm around the servo motor.

Physical distance between the servo motor and the IMU with distances10 mm, and 20 mm.

4.5 Magnetic cross-talk modeling

From the previous project work, described in Section 3.2, it was known that the relationship between the servo motor shaft position and magnetometer measurements could be fitted to a sine function using nonlinear least squares regression [19]. The magnetic field from the BLDC servo motor is a direct effect from the electromagnetic field generated to rotate and control the position of the motor's shaft. In this section, the method of fitting magnetic cross-talk from the servo motor to a sine will be described, as it is specific to the case in hand. However, the general sine fitting described in Section 2.7 was applied. The code

used to perform the sine regression on the experimental data can be found on GitHub, with an example in `modelEvaluation.py` [1].

As described in Section 2.2.2, magnetic fields are additive. This means that in this specific case, the measured magnetic field from the magnetometer is a sum of earth's magnetic field, the servo motor's generated magnetic field, and additional noise and effects in the environment. This is described in Equation (4.1), were $\mathbf{B}_{servo}$ is the magnetic field generated by the servo motor during servo actuation, $\mathbf{B}_{earth}$ is the earth's magnetic field, $\mathbf{B}_{meas}$ is the magnetic field measured by the magnetometer during servo actuation, and $\mathbf{n}$ is the measurement noise. The magnetic field generated by the servo motor can thereby be estimated by Equation (4.4), as a nonlinear function of the servo motor's shaft position $\mathbf{F}(\alpha)$.

$$\mathbf{B}_{meas} = \mathbf{B}_{Earth} + \mathbf{B}_{servo} + \mathbf{n} \tag{4.1}$$

$$\hat{\mathbf{B}}_{servo} = \mathbf{f}(\alpha) \tag{4.2}$$

$$f(\alpha) = A\sin(\omega\alpha - \phi) \tag{4.3}$$

$$\hat{\mathbf{B}}_{servo} = \mathbf{B}_{meas} - \mathbf{B}_{Earth} \tag{4.4}$$

First $\mathbf{B}_{Earth}$ was estimated from the experiments by taking the mean of the magnetometer measurements before servo actuation, as these measurments was not influenced by the magnetic field from the motor. $\mathbf{B}_{servo}$ was then estimated by subtracting $\hat{\mathbf{B}}_{Earth}$ from the measured magnetic field during servo actuation , $\mathbf{B}_{meas}$. Then, the time series of $\hat{\mathbf{B}}_{servo}$ was fitted to a sine as a function of the servo's shaft position, α, using *Scipi's* `curve_fit()` function.

The baseline experiment was used to estimate the sensed magnetic field from the servo motor. The data from the experiment with load was was used as the test set, making it possible to evaluate if the motor disturbance model also was valid with load variations.

4.6 Heading estimation experiment

The previous experiments described in this chapter served as preparatory work to propose how to reduce the disturbances in the magnetic field measurements for the Boa snake robot. The experiments described gave insights on how the magnetic disturbance from the motor could be modelled. This insight were then used to test an improved technique to improve the heading estimation for the Boa snake robot.

The proposed method to be evaluated was as described in the block diagram in Figure 4.6. Feed-forward is used to compensate for the magnetic disturbance

from the servo motor. The magnetic field and gyroscope measurements are then used to estimate the heading of the snake robot link. The heading estimator is an adaptive Kalman filter with Magnetic Disturbance Rejection (MDR) inspired by Widey and Woo [50], as described in the Literature review in Section 3.1. The Kalman filter design and magnetic disturbance rejection technique will be described in further detail in Section 4.6.1 and 4.6.2.

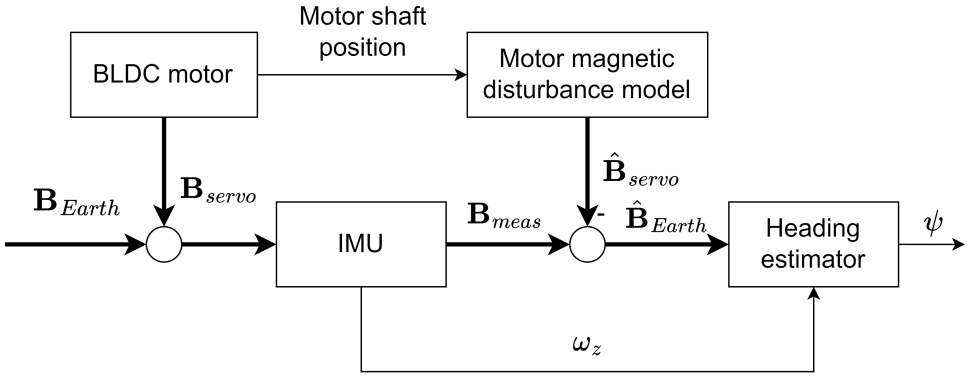

Figure 4.6: Proposed method to improve heading estimates for the Boa snake robot.

To evaluate the performance of the proposed method, one needs something to compare it with. The heading was therefore also estimated using the standard Kalman filter without magnetic disturbance rejection, but still including the feed-forward loop. The *BNO-055*'s internal sensor fusion estimate also served as a reference. Lastly, the two heading estimators where also applied without the feed-forward loop, with the same tunings, to evaluate their performance when purely relying on non-corrected magnetometer data. The tunings for the Kalman filter that was compared is shown in Table 4.1 in degrees. The first tuning was designed to be overconfident in the plant model and gyroscope measurements, and underconfident in the magnetometer measurements. This way, the heading estimate without the magnetometer measurements can be assessed. The second tuning was attempted to achieve the best possible heading estimates without magnetic disturbance rejection, while still using the magnetic field measurements. The last heading estimator tested the Kalman filter with magnetic disturbance rejection, and was tuned to achieve what was believed to be the best heading results using this filter.

To test the heading estimators, there was a lack of proper equipment to perform experiments where the ground truth was tracked. Additionally, due to time limitations, a test rig where the movement of the experimental setup was caused by actuating the motor shaft itself could not be built. Despite this, the best solution was to test the Kalman filters by a simple proof-of-concept experiment. The starting point of the experimental setup was the baseline setup, except that the motor was not clamped to the table. Since the goal of the

Table 4.1: The process and measurement covariance matrices for the different Kalman filter tunings.

	KF tuning 1	KF tuning 2	KF with MDR
Q	$\begin{bmatrix} 0.001^2 & 0 \\ 0 & 10^2 \end{bmatrix}$	$\begin{bmatrix} 0.1^2 & 0 \\ 0 & 10^2 \end{bmatrix}$	$\begin{bmatrix} 0.1^2 & 0 \\ 0 & 10^2 \end{bmatrix}$
R	$\begin{bmatrix} 1^2 & 0 \\ 0 & 0.001^2 \end{bmatrix}$	$\begin{bmatrix} 1^2 & 0 \\ 0 & 0.001^2 \end{bmatrix}$	$\begin{bmatrix} 0.1^2 & 0 \\ 0 & 0.001^2 \end{bmatrix}$

experiment was to evaluate if it is possible to estimate the heading while the servo motor rotates, the only movement needed to estimate the heading is a rotation around the IMU's z-axis. The physical experiment performed rotated the motor counterclockwise about 45°, then counterclockwise back to the initial starting position, around 45° clockwise, and back to the starting position again. The same movement was performed one more time, before lastly the motor was rotated 90° counterclockwise. The movement was performed by hand, while the motor itself was controlled by the same test script as all previous experiments, meaning the motor shaft position had no correlation with the movement of the motor. The initial starting position was approximately 290° (or −70°), and was measured by the compass on a smart phone. The uncertainty in the initial position can therefore be roughly estimated as around ± 10°.

It was attempted to improve the experimental accuracy of the movement by mounting the motor on a camera tripod. For reasons explained in Section 6.5.1, the attempted improvement proved to show key insights into possible practical obstacles which would need to be addressed in future work. The attempted test stand could therefore not be used for the proof of concept heading estimate experiment, and results from this attempt will be further elaborated in Section 6.5.1.

An implementation of the proposed heading estimator can be found on GitHub [1]. The example code found in `KFtest.py` shows the adaptive Kalman filter and feed-forward correction used on the data acquired from the heading experiment.

4.6.1 Kalman filter design

This section describes the Kalman filter design made specifically to estimate the heading during the heading experiment. The Kalman filter algorithm described in Algorithm 1 in Section 2.9 in the Theory was used.

The states of the system was defined as $\mathbf{x} = [\psi, \dot{\psi}]^{\mathrm{T}}$. The system was

approximated to have a constant heading acceleration, as it could not be estimated by torque or force measurements, nor measured. The linear time variant discrete process model was thereby defined as

$$\mathbf{x}_k = \mathbf{F}_{k-1}\mathbf{x}_{k-1} + \mathbf{v}_{k-1} \tag{4.5}$$

$$\mathbf{F}_{k-1} = \begin{bmatrix} 1 & \Delta t_{k-1} \\ 0 & 1 \end{bmatrix} \tag{4.6}$$

$$\mathbf{v}_{k-1} \sim \mathcal{N}(0, \mathbf{Q}_{k-1}) \tag{4.7}$$

with initial state estimate $\mathbf{x}_0 = \mathbf{0}$. The process covriance matrix $\mathbf{Q}_{k-1}$ is the discretized version of $\mathbf{Q}$, and depends on the step size Δt_{k-1}. Since the process was approximated to have constant acceleration, even though it is known not to be true, the entry in $\mathbf{Q}$ belonging to the heading rate should therefore be large compared to the entry belonging to the heading.

To avoid non-linearities, the pseudo measurement of the heading was defined as $\psi_m = \arctan(\frac{magY}{magX})$. The heading rate could be measured as the negative of the gyroscope measurement. The measurement model was thus

$$\mathbf{y}_k = \mathbf{H}\mathbf{x}_k + \mathbf{w} \tag{4.8}$$

$$\mathbf{H} = \begin{bmatrix} 1 & 0 \\ 0 & 1 \end{bmatrix} \tag{4.9}$$

$$\mathbf{w} \sim \mathcal{N}(0, \mathbf{R}) \tag{4.10}$$

where the measurement covariance matrix is $\mathbf{R} = diag([\sigma^2_{\psi_m}, \sigma^2_{\omega}])$. The gyroscope variance could be identified by analysing the gyroscope measurement noise. σ_{ψ_m} is the variance of the pseudo measurement. The standard deviation of the gyroscope measurements found by the experiments should be sufficient to use in the covariance matrix, while σ_{ψ_m} would need to be tuned.

The gyroscope measurement was used in the innovation calculation and update step of the heading rate, while the pseudo measurement was used in the innovation calculation and update step of the heading, as described by $\mathbf{H}$.

4.6.2 Magnetic disturbance rejection

The Magnetic disturbance detection and rejection rules, introduced in Section 3.1, where performed by adaptively increasing the measurement covariance matrix. Let r_h be the entry in the covariance matrix, $\mathbf{R}$, belonging to the heading measurement. Further, let $\sigma^2_{\psi_m}$ be the initial heading pseudo measurement variance. The measurement variance of the heading measurement is adaptively increased based on the square of the residual between the estimated and measured heading as shown in Equation (4.11), and the square error of the

change in earth's magnetic field norm as shown in Equation (4.12).

$$r_h = \sigma^2_{\psi_m} + c(\psi_k - \hat{\psi}_k)^2 \tag{4.11}$$

$$r_h += c(B_k - B_0)^2 \tag{4.12}$$

where ψ_k is the measured heading from the magnetometer measurements, $\hat{\psi}_k$ is the heading estimate from the Kalman filter at time step k, B_k is the magnetometer norm at time step k, and B_0 is the initial magnetometer norm before the servo motor start to actuate. c is a scaling factor, which was tuned to 0.01. Note that only the x- and y- axis magnetometer measurements where used in the Kalman filter.

Chapter 5

Results

In this chapter, the results from the work performed in the different phases to improve the heading estimates will be presented. First, Section 5.1 presents the nominal magnetometer noise characterization results. Second, the results from the baseline experiment are presented in Section 5.2, followed by the additional load results in Section 5.3. Section 5.4 presents the results from phase 4 on magnetic cross-talk modelling. The shielding experiments are then presented in Section 5.5, although the experiments were performed in phase 3. This was decided since the conclusions drawn from the data relied on the cross-talk modelling results. Lastly, the improved heading estimation results are presented in Section 5.6.

Note that the gyroscope and accelerometer data collected from the baseline and additional load experiments in phase 3 were used to conclude on phase 2 on IMU measurement noise characterization, as well as phase 4 on motor field disturbance modelling.

5.1 Magnetometer noise characterization

As described in Ning *et al.*, the magnetometer's measurement noise might need to be modelled in terms of an ARMA model [39], and not as white Gaussian noise which often is the normal assumption. This was investigated performing time series analysis on a 15 minutes long time series where the IMU lay motionless on a table, as described in Section 4.3. The time series is shown in Figure 5.1. It shows that the IMU measurements has many large outliers with approximately the same value, but otherwise visually look like white noise. The density of the measurements along each axes are plotted in Figure 5.2. The x- and z-axes clearly follows a normal distribution.

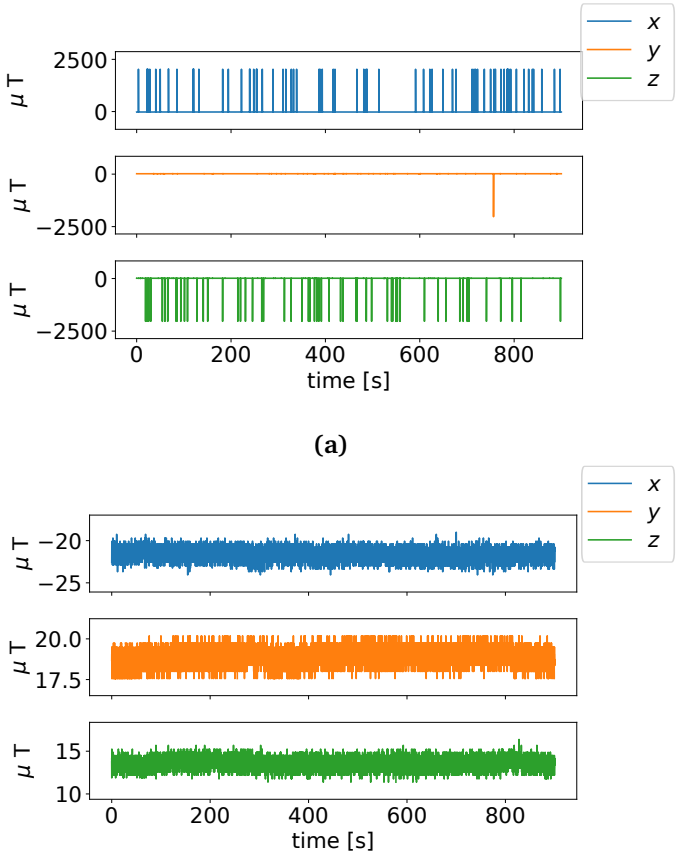

Figure 5.1: Time series plot of the magnetometer measurement noise, a) with outliers, and b) after removing outliers.

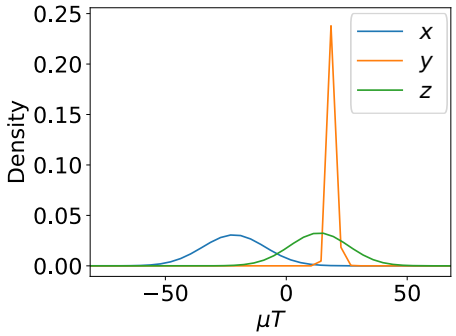

Figure 5.2: Density plot of the magnetometer measurement time series.

The mean, standard deviation, skew and excess kurtosis of the magnetometer data is displayed with three decimals in Table 5.1a. The kurtosis, skew and standard deviation is very large. Removing the outliers using the IQR method with a scale of 3 (instead of the normal scale of 1.5 to only remove the data points due to sensor faults), yielded the results in Table 5.1b.

Table 5.1: Magnetometer measurement statistics from the nominal magnetometer noise experiment with a) the entire dataset and b) after removing outliers.

(a)

	x	y	z
skew	20.175	-169.801	-21.425
kurtosis	405.057	28924.743	457.105
mean [μT]	-16.670	18.857	9.149
std [μT]	101.042	12.015	95.174

(b)

	x	y	z
skew	0.018	-0.014	-0.075
kurtosis	0.133	-0.095	-0.033
mean [μT]	-21.666	18.915	13.599
std [μT]	0.634	0.486	0.612

The auto correlation and partial auto correlation function of the data set, used to determine whether an ARMA model of the magnetometer noise was needed, are displayed in Figure 5.3. It is observed that lag 1 is within the 95 % confidence interval, shown in green, in both the ACF and PACF plot. The noise therefore has no autocorrelation or partial autocorrelation, and an ARMA model is not needed.

5.2 Baseline servo actuation experiment

As described in Section 4.4, several tests were conducted to investigate the effect of the magnetic cross-talk between the motor and the IMU. In this section, the results from the baseline servo actuation experiment is presented. To make the plots more readable, evident outliers were removed. Through this entire section, the motor's position or velocity refers to the angular position or rotational velocity of the servo motor's shaft if not otherwise is specified. The motor itself was always secured to a table, and did not move throughout the experiment.

A time series plot of the motor's position and velocity, and the magnetometer measurements, is presented in Figure 5.4. The servo motor and IMU themselves did not move during the test, and the change in magnetic field can thus be fully attributed to the motor's generated magnetic field. The electromagnetic field along each axis changes when the motor shaft rotates.

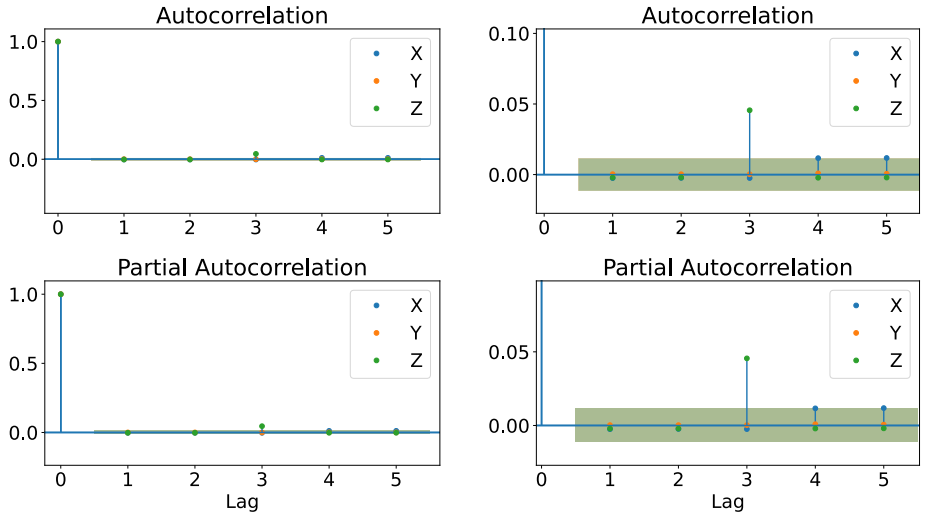

Figure 5.3: Auto correlation and partial auto correlation plot of the magnetometer measurements a) up to lag five, and b) zoomed in on the confidence interval, shown in green. The plot was made using *Statsmodels'* `graphics.tsa.plot_acf` and `graphics.tsa.plot_pacf` functions [8].

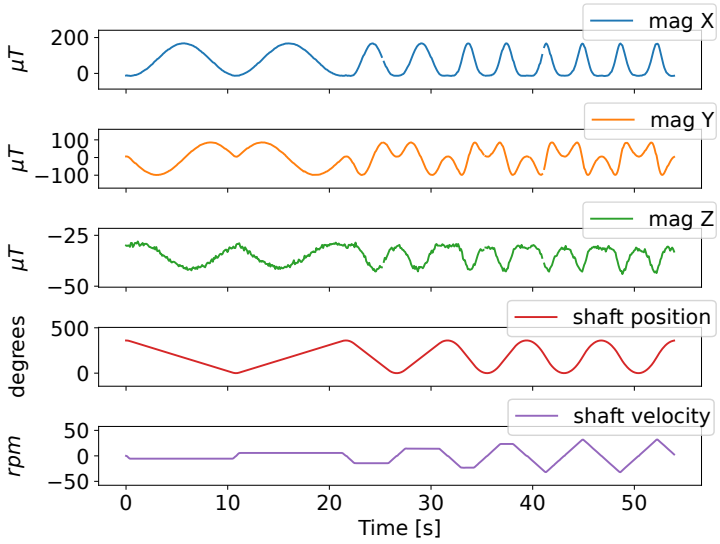

Figure 5.4: Timeseries from the baseline servo actuation experiment. The two last rows shows the motor shaft position and velocity during the experiment, which were pre-programmed. The three first rows shows the measured magnetic field along the x-, y- and z- axis. The missing data points are outliers which were removed.

To easily get an overview of the experimental results, pair plots for the accelerometer, gyroscope and magnetometer measurements against the motor's shaft position, velocity and torque current were made using *Seaborn's* `pairplot` function [7]. These can be found in Appendix A in Figures A.1, A.2, and Figure A.3. In this section, the observations from the pair plots of particular interest will be extracted and displayed in a concise format for the reader.

The first evident observations is that neither the gyroscope or accelerometer measurements show any correlation with the motor position, velocity nor torque current for any of the sensor axes. This can be seen in Figure 5.5 with an example of the z-axis gyroscope scatter plots. The accelerometer scatter plots are similar. Additionally, the pair plots displayed no correlation between the motor's torque current and any of the IMU measurements.

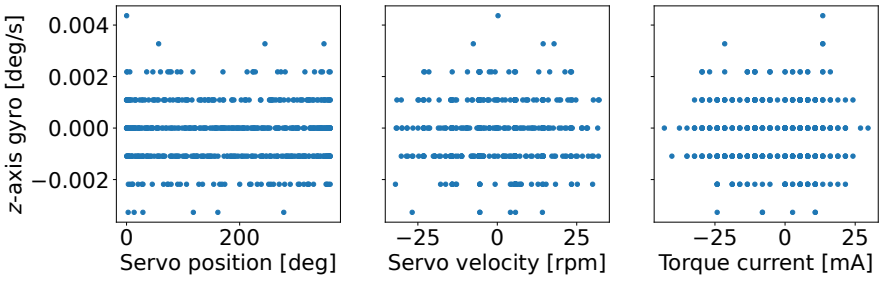

Figure 5.5: Scatter plots between the gyroscope z-axis and the motor shaft's angular position, velocity and torque current, viewing no clear correlations.

Figure 5.6 displays a 3D scatter plot between each magnetometer axes, and scatter plots between each of the axes and the motor position in degrees. The expected sine relationship between the motor position and the magnetic field measurements are evident. Furthermore, the 3D scatter plot views that the magnitude of the magnetic field rotates along an ellipse with the rotation of the motor's shaft. It is observed that x-and y-axis magnetic fields has a peak-to-peak of approximately 175 µT, while the z-axis field has a peak-to-peak of approximately 15 µT.

The magnetometer scatter plots against the servo velocity shows complex patterns, as viewed in Figure 5.7. There are nonlinear curves, as well as evenly spaced lines at different speeds, and the x- and z-axis magnetic fields seems to be outer bounded by a nonlinear curve. However, the different speeds spans the entire magnetic filed span along the y-axis. As will be explained and discussed in Section 6.2, the patterns are however due to the design of the experiment.

Figure 5.8 displays density histograms from the baseline experiment when the motor shaft rotated for one axis of each sensor. The other axes had similar shapes. The figure shows that the accelerometer and gyroscope measurements are approximately normal distributed even when the motor actuates. Oppositely,

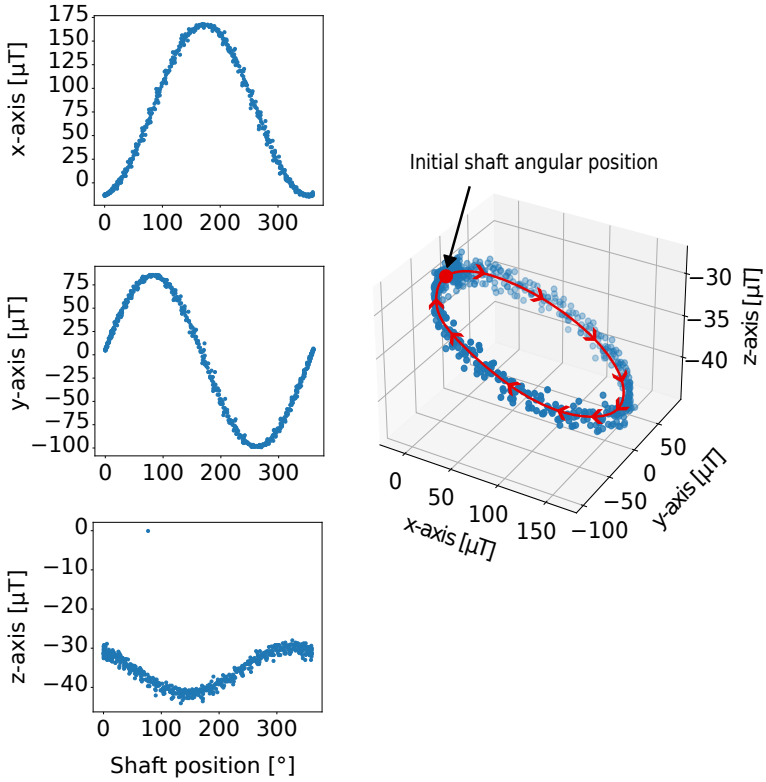

Figure 5.6: 3D scatter plot of magnetometer measurement along each axis, and the clear correlation between the position of the motor shaft and the measured magnetic field. The scatter plots shows that the magnetic field rotates with the motor shaft rotation.

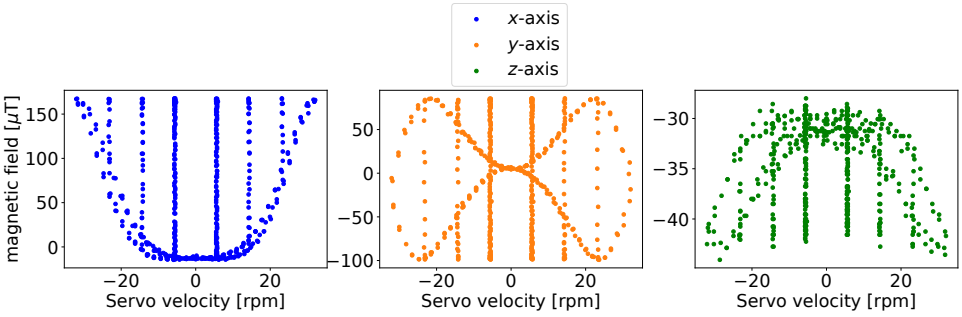

Figure 5.7: Scatter plot between the measurements of each magnetometer axis and the motor velocity. The complex patterns is due to the design of the experiment.

the magnetic field density is clearly not normal distributed. This is as expected from the observed correlation plots in Figures 5.5 and 5.6.

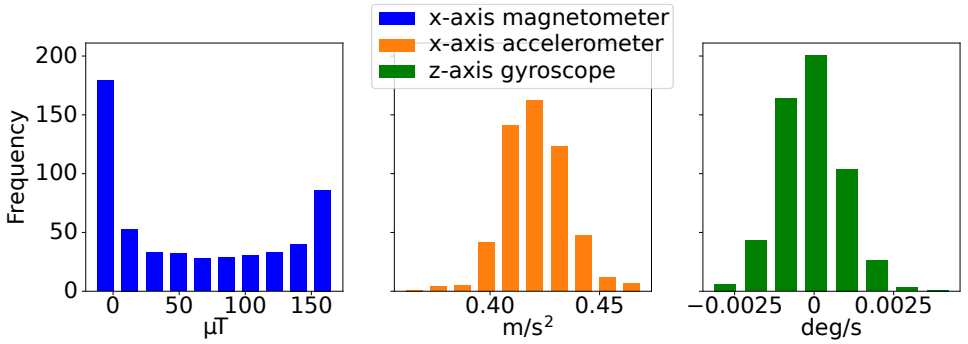

Figure 5.8: Histogram plots of the sample densities of one axis for each IMU sensor during servo actuation from the baseline experiment. The gyroscope view is from the z-axis, as this is the one axis relevant for a planar snake robot.

Figure 5.9 compares the raw magnetometer measurements before and after the servo actuation test, to inspect if the motor actuation left any permanent effects on the magnetic field measurements. The figure visually shows no difference.

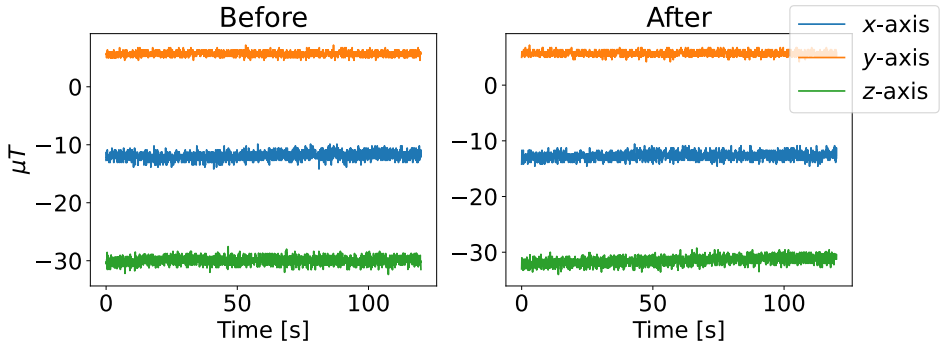

Figure 5.9: Comparison of the magnetometer measurements before and after the motor actuates in the baseline experiment.

The mean, standard deviation, excess kurtosis and skewness of the IMU measurements before, during and after the motor actuation are further presented in Tables 5.2, 5.3 and 5.4. Table 5.2 shows that the largest change in the magnetometer means was along the z-axis with 1.531 μT. The standard deviations of the magnetometer measurements after servo actuation were approximately the same as before actuation, but not equal. The change is however negligible in the engineering context. The skew and kurtosis also changed with around 0.1 for each axis, but while the x- and z axis kurtosis increased, the y-axis decreased. The changes are however relatively small.

Table 5.2: Magnetometer sample statistics before and after the servo actuation in the baseline experiment. The statistics during servo actuation was omitted as the measurements were known to be strongly affected by the motor.

	mean	**std**	**skew**	**kurtosis**
Before				
magX	-11.941	0.656	0.140	0.079
magY	5.695	0.400	-0.005	-0.198
magZ	-29.964	0.623	-0.054	-0.040
After				
magX	-12.656	0.612	-0.067	0.172
magY	5.708	0.409	-0.038	0.016
magZ	-31.495	0.708	-0.077	-0.163

Table 5.4 shows that the statistics for the gyroscope measurements are approximately equal before, during and after servo actuation. The same applies to the accelerometer measurement statistics in Table 5.3. It is however observed that the accelerometer has a skew of over 0.5 along the z-axis both before and during servo actuation, and a kurtosis over 1 for the x- and z- axes both before, during and after servo actuation. This might indicate the accelerometer measurement noise does not follow the Gaussian distribution, and will be further discussed in Section 6.2.1.

Table 5.3: Accelerometer sample statistics before, during and after the servo actuation in the baseline experiment.

	mean	**std**	**skew**	**kurtosis**
Before				
accX	0.420	0.012	-0.029	1.035
accY	0.378	0.014	-0.070	0.482
accZ	9.824	0.017	-0.500	1.135
During				
accX	0.420	0.014	0.139	1.270
accY	0.380	0.014	-0.062	-0.019
accZ	9.824	0.017	-0.599	1.721
After				
accX	0.419	0.013	-0.032	0.606
accY	0.379	0.013	-0.072	0.035
accZ	9.824	0.018	-0.321	1.123

Table 5.4: Gyroscope sample statistics before, during and after the servo actuation in the baseline experiment.

	mean	**std**	**skew**	**kurtosis**
Before				
gyrX	0.000	0.001	0.115	0.005
gyrY	-0.000	0.002	-0.001	0.012
gyrZ	-0.000	0.001	-0.015	0.138
During				
gyrX	0.000	0.001	-0.024	0.448
gyrY	0.000	0.002	0.089	-0.152
gyrZ	0.000	0.001	0.193	0.298
After				
gyrX	0.000	0.001	-0.009	-0.058
gyrY	0.000	0.002	-0.035	0.249
gyrZ	0.000	0.001	0.070	0.007

5.3 Servo actuation experiment with load

The additional load experiment served two purposes. The first was to investigate if the magnetic field sensed by the magnetometer changed significantly. The second, and related, purpose, was to validate the model of the magnetic disturbance from the motor when the motor load changes. In this section, the resulting torque current and magnetic field is compared to the baseline experiment, and the mean, standard deviations, skew and kurtosis is presented. The data was further used in the motor disturbance modelling. The sine regression performed on the additional load data set will therefore be presented in Section 5.4.

Figure 5.10 compares the torque current during the baseline experiment and the load experiment. The torque current is clearly larger during the load experiment. The negative current is when the motor rotates in the negative direction. The change in the measured magnetic field with and without load is shown in Figure 5.11. Note that the initial magnetic field before the servo actuation are different for the experiment without and with load. The difference is less than 5 μT.

For the interested reader, Appendix A.2 presents the pair plots during the servo actuation with additional load in Figures A.4, A.5 and A.6. The figures were put in the appendix due to their similarities to the pair plots from the baseline experiment.

Table 5.5 shows the mean, standard deviation, skew and kurtosis for the magnetometer measurements before and after servo actuation with load. It views almost no change after servo actuation. The z-axis mean however increased by

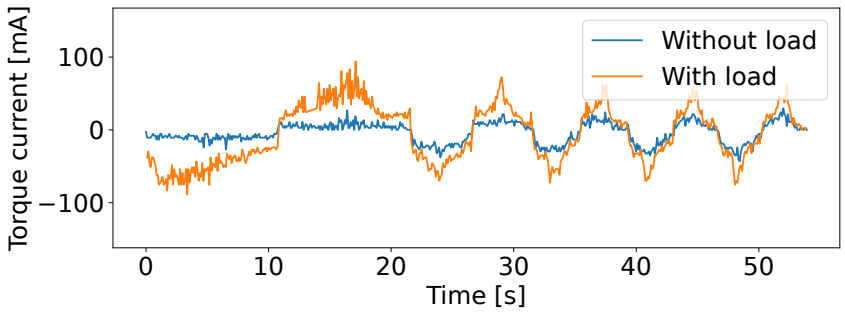

Figure 5.10: Torque current during servo actuation with and without additional load.

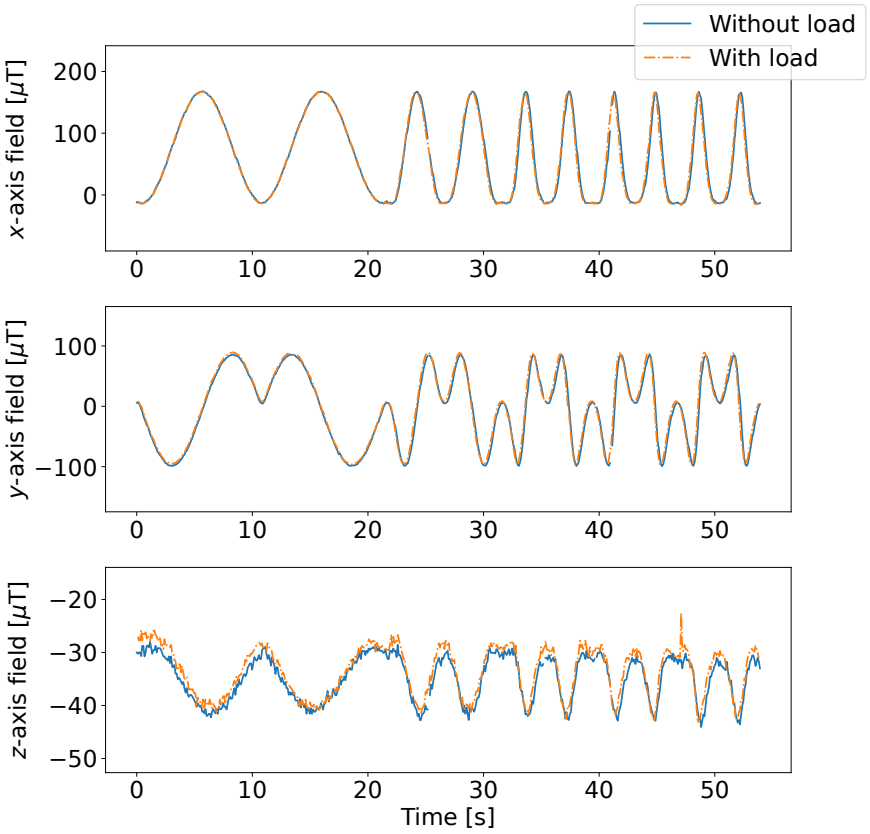

Figure 5.11: The magnetic field in the x-, y- and z- direction over time during servo actuation with and without load.

2.5 μT. The statistics for the gyroscope and accelerometer measurements viewed no clear change, and can be found in Tables A.1 and A.2 in Appendix A.3 by the interested reader. The statistical tables were used to find the distribution of the IMU noise, and the relevant numbers will be summarized and analysed in the discussion.

Table 5.5: Magnetometer sample statistics before and after the servo actuation in the additional load experiment. The statistics during servo actuation was omitted as the measurements where known to be strongly affected by the motor.

	mean	**std**	**skew**	**kurtosis**
Before				
magX	-12.267	0.621	-0.080	-0.038
magY	8.417	0.454	-0.086	-0.138
magZ	-27.718	0.597	0.030	0.053
After				
magX	-13.261	0.624	-0.110	0.106
magY	8.037	0.459	-0.010	-0.384
magZ	-30.349	0.665	0.043	0.043

5.4 Magnetic cross-talk modeling

The modelling of the cross-talk from the servo motor disturbance were based on the results from the servo motor experiments, and the evident sine relation between the magnetic field measurements and the servo motor shaft position. The model was used to predict the magnetic disturbance from the servo motor to improve the heading estimates which are presented in Section 5.6. In this section, any mention of periodic signal and sine function will be in the servo shaft position domain, and not the time domain unless specifically mentioned. This is due to the magnetic field following a sinusoidal curve as a function of the motor shaft position. The data presented is the magnetometer measurements from both the baseline experiment and the additional load experiment, but subtracted by the magnetic field of the earth that the IMU measured before the servo actuation, as described in Section 4.5. First, the sine function fitted on the baseline and load experiment data is presented. These results will be used to conclude on the effect of additional motor load. Second, the model built from the baseline experiment is evaluated, and tested on the data from the additional load experiment.

5.4.1 Sine regression on the baseline and load experimental data

Figure 5.12 shows the fitted sine function to the servo motor magnetic field, as sensed by the magnetometer, along each axis using non linear least's squares with *SciPy's* `curve_fit` function [9]. One can see that one rotation of the servo motor

shaft is one period of the generated magnetic field. Both the x- and y- axis start at approximately 0 µT at the shaft position of 0°. The z- axis starts at approximately 2 µT to 5 µT. The x- and y- axes has approximately 30° phase shift. The amplitude of the x- and y- axes are both approximately 90 µT. Figure 5.13 shows the fitted sine function to the servo's generated magnetic field during the experiment with load. The sines differs from the baseline experiment with approximately 1 µT, meaning that the effect of additional rotational load is in practice not visible in terms of the cross-talk model.

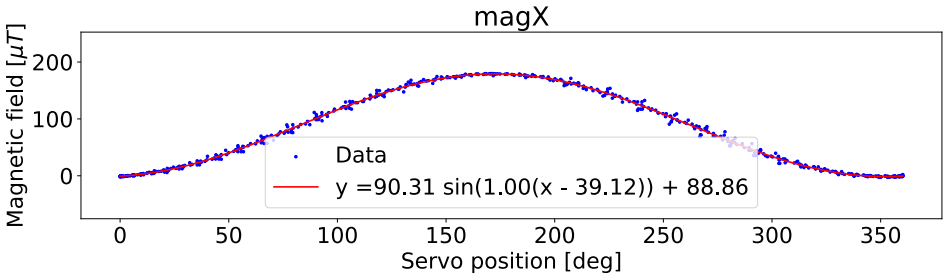

(a)

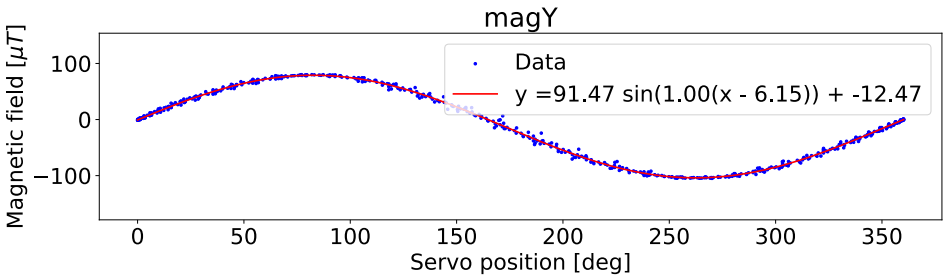

(b)

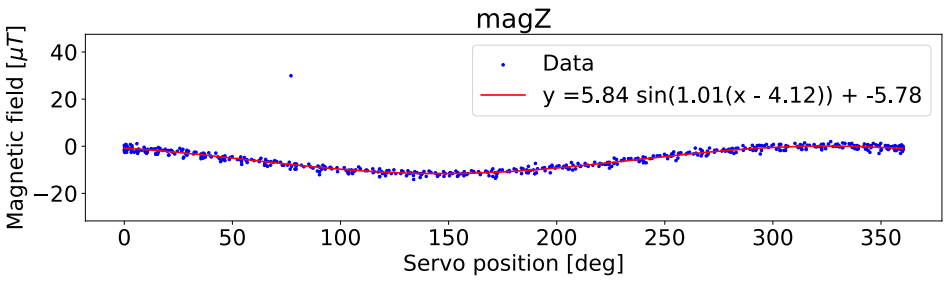

(c)

Figure 5.12: Sine regression of the magnetic cross-talk from the motor during the baseline experiment.

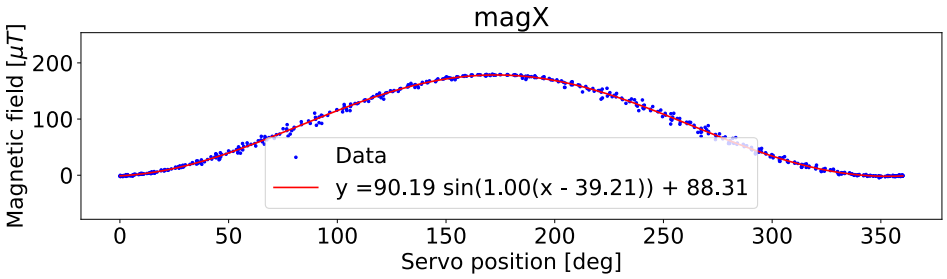

(a)

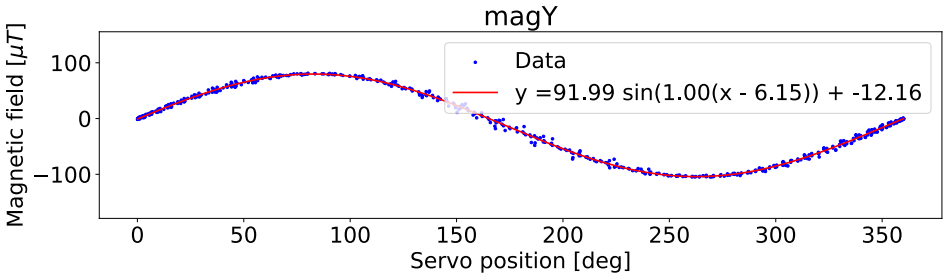

(b)

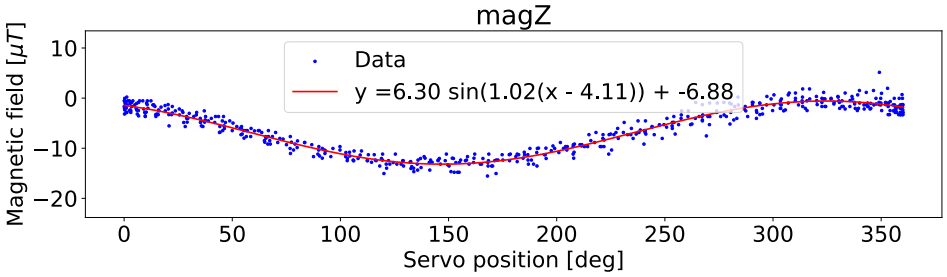

(c)

Figure 5.13: Sine regression of the magnetic cross-talk from the motor with additional motor load

5.4.2 Model performance

From this point on, references to "the model" or "the magnetic disturbance model" is the fitted sine to the baseline experiment data. As described in Section 4.5, the training data is the baseline experimental data, while the test data is the data set from the additional load experiment.

The model performance was evaluated by inspecting the residuals and RMSE of the model to both the training and the test data. The residuals and RMSE of the training data describes the general fit of the model, while the residuals and RMSE of the test data can be used to evaluate if the model is valid when the servo motor is subject to external load. The residuals are plotted against time and the motor velocity in Figure 5.14. The standard deviation of the residuals, and the RMSE of the model is given in Table 5.6.

(a)

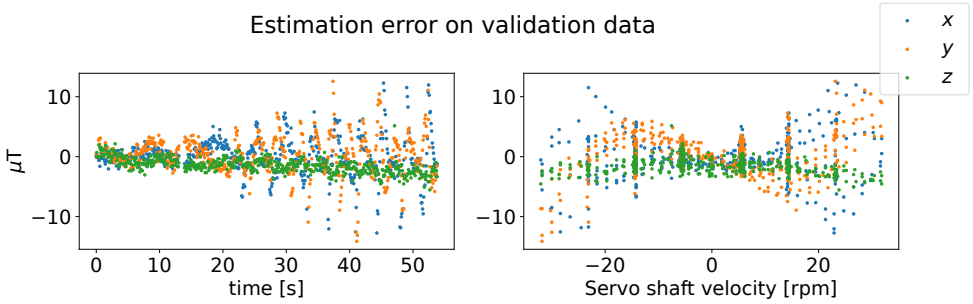

(b)

Figure 5.14: The motor model residuals when the model was used on a) the training data (from the servo actuation data during the baseline experiment), and b) the test data (from the servo actuation data during the additional load experiment).

It is observed that the residuals are similar in magnitude on both the training and test data. The residuals are higher when the motor shaft has higher velocity. It is also observed that in the time domain, the motor residuals follow the same trend as the magnetic field, but time shifted. The difference between the RMSE and standard deviations on the training and test data are less than the resolution

Table 5.6: Standard deviation and RMSE of the residuals from the motor magnetic disturbance model on training and test data.

	std training	std test	RMSE training	RMSE test
x	3.299	3.257	3.316	3.257
y	3.033	3.200	3.033	3.205
z	1.875	1.223	1.937	1.909

of the magnetometer (0.3 µT), and thus approximately equal: $\sigma_e \approx (3.3, 3.1, 1.9)$ µT. The standard deviation of the residuals gives an indication of the spread in the data, and can be used in the sensor fusion algorithm to estimate the heading. The use of these values will be described and discussed in Section 6.3.

5.5 Shielding results

In this section, the results from the physical magnetic disturbance mitigation techniques are presented. The goal of the shielding experiments were to see if shielding could improve the magnetic field model by overall reducing the sensed field from the motor. As part of the shielding experiment, one experiment with the baseline setup was conducted, since the experiments were performed in a different physical location than the baseline and additional load experiments.

The initial measured magnetic field after calibration, but before the servo actuates, for some of the shielding experiments are shown in Figure 5.15. The figure shows that the initial calibrated yielded different magnetic fields for all the experiments, even though the position and orientation of the IMU and the servo motor was approximately the same for all tests. Why these differences occurred will be discussed in Section 6.4.

Since the initial magnetic field varied between each experiment, the time series plots of each experiment was deemed an imprecise way of comparing the effectiveness of shielding. Instead, the motor field was estimated, and the model residuals and RMSE was used as a measure of the shielding performance. The residuals are plotted in Figures 5.16 and 5.17 for the shielding sheets and distance experiments respectively. The plots shows that the residuals are larger with shielding sheets in the beginning of the time series where the motor shaft had a low velocity, but is lower at the end of the experiment where the motor has a higher velocity. The effect of a 20 mm distance yields the lowest residuals.

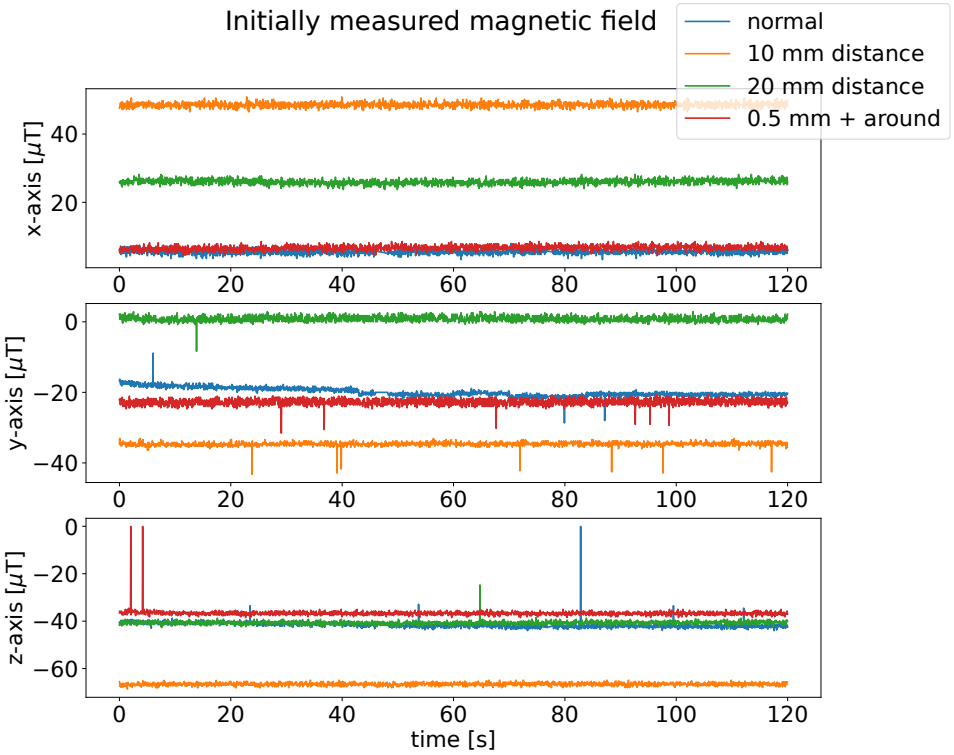

Figure 5.15: Magnetic field after calibration without servo motor actuation during the experiments with physical distance and with the 0.5 mm ferrite shielding sheets between the servo motor and the IMU. The rest of the shielding sheets experiments had all different initial values, but are not included in the plot to make it easier to read.

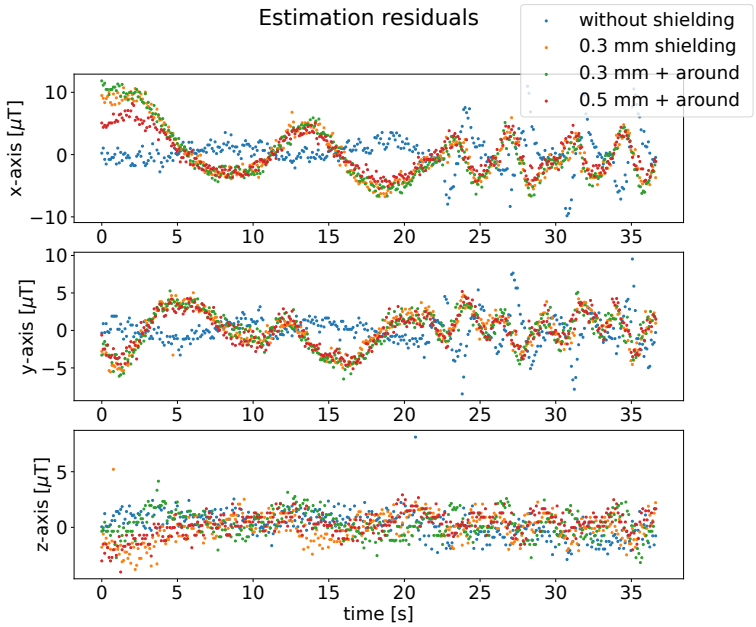

Figure 5.16: Estimated motor field residuals during the servo motor actuation tests with ferrite shielding sheets between the servo motor and the IMU.

It was generally observed that shielding sheets gave a more inconsistent magnetic field. The motor field estimate with 0.1 mm shielding is shown in Figure 5.18. It shows that the magnetic field from the motor sensed by the magnetometer spreads for the x- and y- axis fields, most likely either due to hysteresis, or the change in motor velocity.

The RMSE of the cross-talk model from the motor's magnetic field built from the the shielding experiments are shown in Table 5.7. The table shows that the RMSE of the model is larger with shielding sheets. Reducing the magnetic field by adding an additional distance of 20 mm between the IMU and servo motor yields an RMSE of around 1 μT.

Table 5.7: RMSE values of the motor field estimation during the experiments with different physical magnetic field disturbance reduction methods.

	RMSE x	RMSE y	RMSE z
0.0 mm shielding or distance	2.821	2.063	1.170
0.3 mm shielding	4.141	2.406	1.201
0.3 mm shielding + around	4.359	2.437	1.195
0.5 mm shielding + around	3.030	2.259	1.111
10 mm distance	1.541	1.290	0.901
20 mm distance	1.094	1.007	0.934

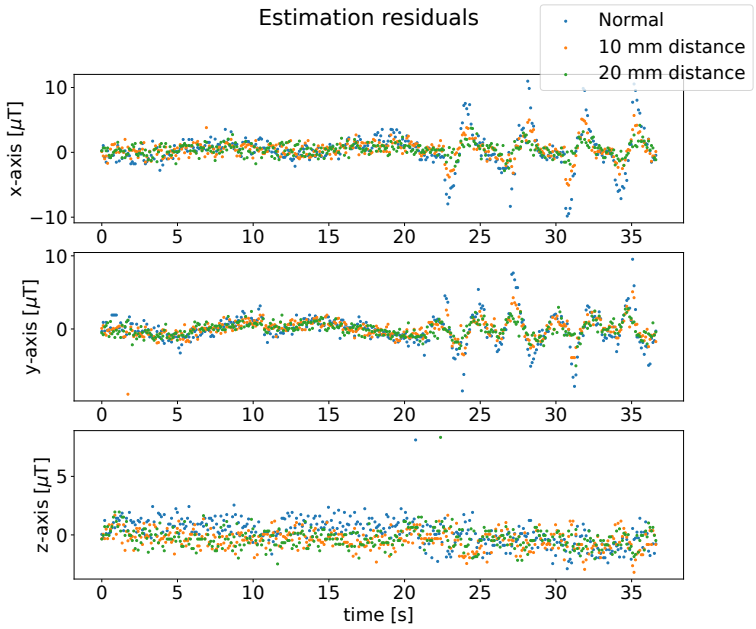

Figure 5.17: Estimated motor field residuals during the servo motor actuation tests with additional 10 mm and 20 mm distance between the servo motor and the IMU. ”Normal” is with the distance between the IMU and servo motor as in the baseline experimental setup, and could be referred to as 0 mm additional distance.

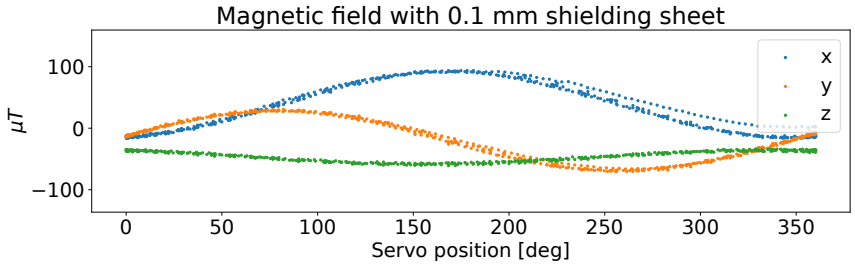

Figure 5.18: Magnetic field from the servo motor sensed by the magnetometer as a function of servo position when there is 0.1 mm shielding sheet between the motor and the IMU. The sheets introduced effects which made the the measured magnetic field more noisy.

Figure 5.19 shows the degree of magnetic field attenuation the shielding sheet thickness and distance yielded. Only the 0.5 mm shielding sheet experiment, which gave the highest degree of attenuation, is viewed to make the plot easier to read. The fitted sine to the motor disturbance was used to show the degree of magnetic field attenuation, instead of the raw data since the noisiness of the measurements during the shielding experiment would make the plot hard to read. It is observed that 20 mm has approximately the same attenuation as with 0.5 mm of shielding sheets, compared to no shielding or additional distance shown in blue.

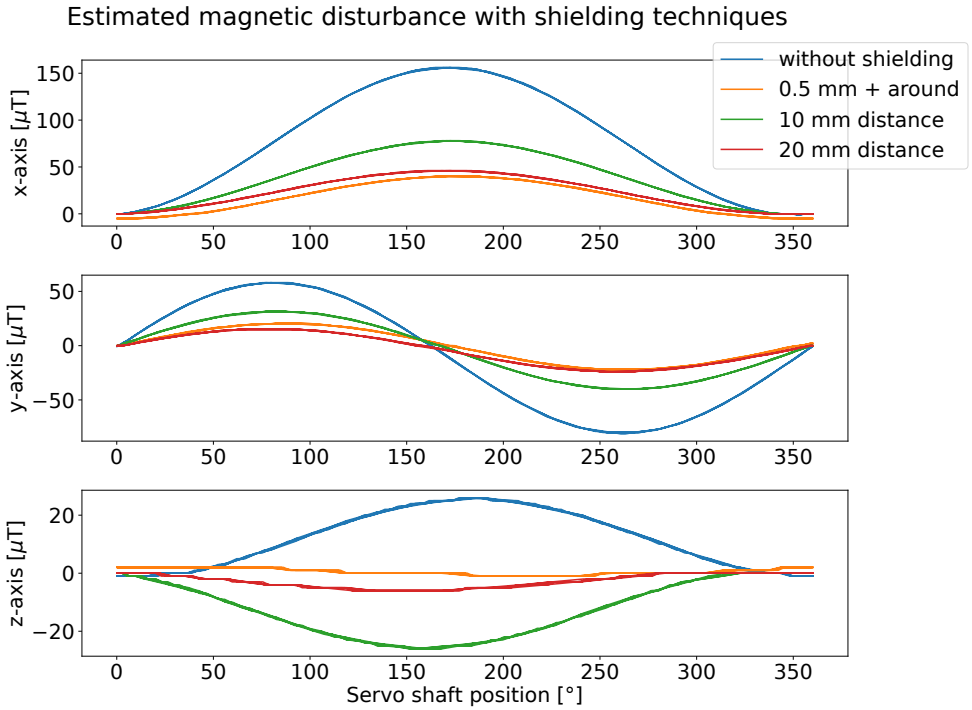

Figure 5.19: Estimated servo field with the different shielding techniques. Only the shielding sheet experiment with 0.5 mm of shielding is displayed for easier inspection.

5.6 Heading estimation

The proposed method of correcting the magnetic field measurements, by feed-forwarding the estimated magnetic disturbance from the motor, was tested by designing two Kalman filters: the standard Kalman filter, and a Kalman filter with the magnetic disturbance rejection method described in Section 4.6.2. The initial state estimate for the filters were $\mathbf{0}$. As no ground truth where known, the *BNO-055*'s own heading estimate served as a reference, even though there was no guarantee that this estimate was correct. Remember that the initial heading

was known to be approximately −70 deg, and that the movement was aimed to follow the following pattern on eye sight: 45° counterclockwise, 90° clockwise, 90° counterclockwise, 45° clockwise, 45° counterclockwise and lastly 90° counterclockwise and back to starting position. During this movement, the servo motor shaft rotated as programmed in the test script in Figure 4.5.

Figure 5.20 compares the pseudo measurement of the heading, the *BNO-055* estimate, two different tunings of the standard Kalman filter, and the Kalman filter with magnetic disturbance rejection. The covariance matrices for the different filters were shown in Table 4.1 in degrees. Note that $\mathbf{Q}$ was discretized in the Kalman filter. The left plot shows the heading estimators with feed-forward correction of the predicted cross-talk from the motor, while the right plot did not use feed-forward. The estimates with feed-forward correction will first be presented.

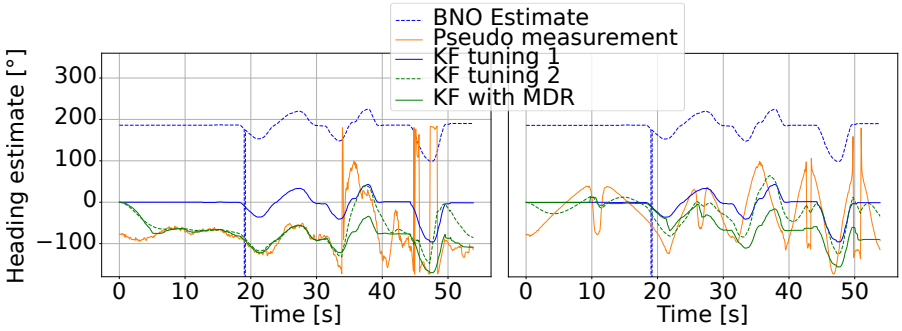

Figure 5.20: The heading estimates with servo motor magnetic disturbance, using the standard Kalman filter, and a Kalman filter with magnetic disturbance rejection. On the left, the magnetic field measurements were corrected by feed-forwarding the predicted magnetic disturbance from the motor before they were used in the Kalman filter. The right plot shows the heading estimates without feed-forward. The Kalman filters had initial state estimate of $\mathbf{0}$. The tuning parameters were as shown in Table 4.1. The heading was known to be approximately −70°.

The first, overconfident, tuning of the standard Kalman filter had an almost identical shape as the BNO estimate, however with an initial estimate of around 180°. The process covariance matrix was small for the heading estimate, meaning that it was very confident in the heading plant model. Additionally, the heading pseudo measurement variance was large compared to the gyroscope variance, meaning that the Kalman filter mainly relied on the gyroscope measurements. The first tuning therefore was able to capture the relative movement of the motor and IMU, but not estimate the correct heading value.

The second tuning of the standard Kalman filter was the best tuning achieved without the magnetic disturbance rejection rule presented in Section 4.6.2. It converged towards the raw pseudo measurement, but was greatly affected by large changes in the magnetic field. The shape deviated from the

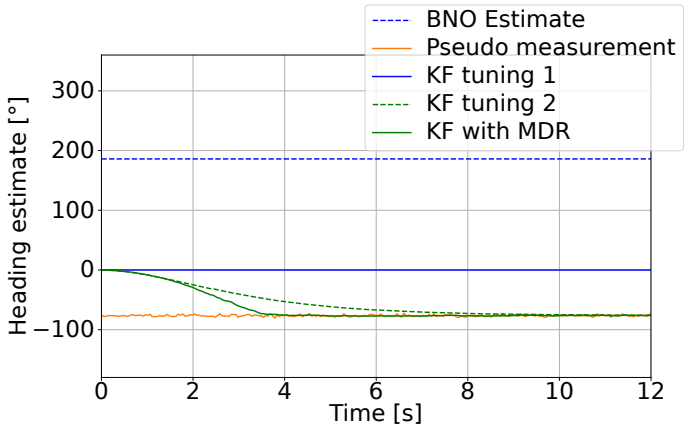

Figure 5.21: The initial heading estimates without servo motor magnetic disturbance or motor movement, using the standard Kalman filter, and a Kalman filter with magnetic disturbance rejection. The Kalman filters had initial state estimate of $\mathbf{0}$. The tuning parameters were as shown in Table 4.1. The initial heading was known to be approximately $-70°$.

BNO estimate, and reported a change in heading of more than 100° in the time frame 30 s to 40 s. This is the time frame where the movement was known to be less than 90°. In the time frame after 30 seconds, the motor speed and model residuals were known to be the largest, based on the motor model evaluation. The second Kalman filter tuning was therefore not able to estimate the heading correctly when the motor shaft rotated with higher velocities.

The Kalman filter with magnetic noise rejection follows approximately the same shape as the BNO estimate and first Kalman filter tuning, but were not biased with respect to the pseudo measurements. The Kalman filter with magnetic disturbance rejection thereby yields the best heading estimation results of the tested filters, based on the apriori information about the heading.

The heading estimates performed without feed-forward correction are shown in the right plot of Figure 5.20. One can see that the first Kalman filter tuning looks exactly the same as with feed-forward. The second tuning was affected by the disturbed magnetic field. This can be seen during the first 20 seconds, where the experimental setup were motionless on the table, and the second Kalman filter tuning reports a change in the heading. The Kalman filter with magnetic noise reduction was also not able to catch the correct movement in the time frame 20 - 30 seconds, but was able to stabilize at about 30 s. This shows that the filters on their own are not able to reliably estimate the heading without the magnetic cross-talk predictor and feed-forward loop.

In advance of the movement, nominal IMU measurements with no servo shaft rotation or movement of the motor was conducted, as with the other

experiments. The Kalman filters' and IMU's estimates from these measurements are shown in Figure 5.21. As one can see, the *BNO-055* estimate initially had the same initial estimate as during the servo movement. The first Kalman filter stays constantly equal to zero. The pseudo measurement had a mean of approximately $-75°$, and both the second Kalman filter tuning and the Kalman filter with magnetic disturbance rejection converges towards the pseudo measurement. One can see that the Kalman filter with magnetic disturbance rejection had the fastest convergence rate. This shows that the BNO estimate and the first tuning of the Kalman filter is over confident in the plant model.

5.7 Observations on surrounding metals

The attempt of improving the experimental setup of the heading experiment by mounting the motor and IMU on top of a camera tripod gave some interesting observations. Figure 5.22 shows the magnetic field when the baseline experimental setup was performed on the camera tripod. It shows similar patterns as the ones seen in the shielding sheets experiments in Figure 5.18, however much stronger. The measurements has a large range in the magnetic field. This observation consequentially led to the decision of not using the setup for the proof-of-concept heading experiment. The observed effect will be used to discuss the choice of materials of the snake robot's chassis, as well as what this may mean in terms of magnetic disturbances of the environment in Section 6.5.1.

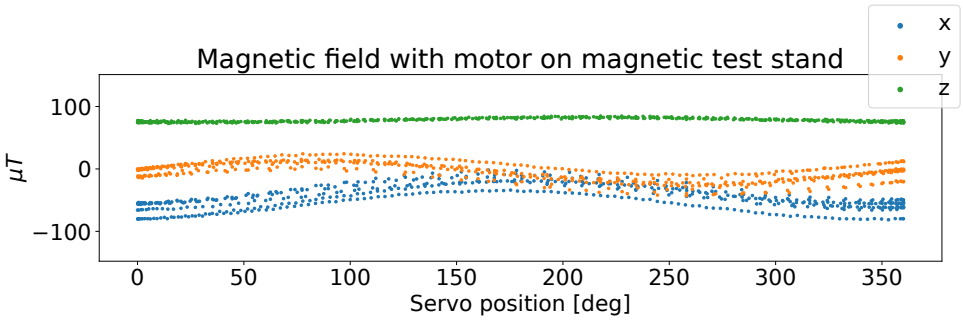

Figure 5.22: Surrounding metals makes the amplitude and offset of the magnetic cross-talk less predictable. The data acquired was from a baseline experiment, but with the motor mounted on top of a camera tripod which contained metals.

Chapter 6

Discussion

The aim of this thesis is to improve the heading estimates of the Boa snake robot, even in the presence of magnetic disturbances from the brushless DC servo motor. This chapter discuss the results and evaluates if the work was able to achieve its goal.

First, the results from the magnetometer noise characterization is discussed in Section 6.1.1. It was found that it cannot be modelled using an ARMA series. The discussion will therefore focus on the statistical properties of the time series and from there determine the magnetometer noise. Secondly, the gyroscope and accelerometer measurements noise is determined in Section 6.1.2 using the statistical data acquired during the pure IMU measurements sampled before and after the servo actuation in the baseline and load experiment.

In Section 6.2, the conclusions from the previous project work on the Boa snake robot are validated for the new Boa motor, using the data from the baseline and additional load experiments. As part of the validation, the IMU measurements before and after the servo actuation are compared to see if the servo motor's generated electromagnetic field had any permanent effects on the measurements. They are also compared with the measurements during servo actuation.

The results clearly validated that the magnetic cross-talk from the motor follows a sine curve as a function of the servo motor's angular position. The model of the magnetic cross-talk from the motor is evaluated in Section 6.3 using the results from the baseline and additional load experiments.

Further on, from the shielding experimental results, it was clear that the magnetic field measurements were more spread with shielding sheets than without shielding or additional distance. Section 6.4, is devoted to discussing these interesting results and how this affected the model performance and heading estimation.

The heading estimation results using a normal Kalman filter and an adaptive Kalman filter, both with and without feed-forward correction of the magnetic cross-talk, are evaluated in Section 6.5. Based on the entire discussion, a method to improve the heading estimates will be presented in Section 6.6. Lastly, the methodology of the work is discussed in Section 6.7, and future work proposed in Section 6.8.

6.1 IMU noise characterization

In attitude estimation, it is important to have a thorough understanding of the measurement noise. The Kalman filter assumes white Gaussian noise. The Kalman filter also relies on the correct tuning of the measurement covariance matrix. The IMU noise is therefore characterized in this Section based on the results from the nominal IMU measurements where the motor did not actuate. It is important to remember that the noise of course is relative to the environment where the test was performed and the calibration of IMU. The experiments was performed inside a building in Trondheim. Each calibration before each experiment was also unique.

6.1.1 Magnetometer noise evaluation

The magnetometer's nominal measurement noise is important to model correctly to obtain accurate heading estimates. Although the nominal measurement noise will be negligible while the servo motor actuates, the correct measurement noise model is important to know for the heading estimation when the servo motor's torque is disabled. Additionally, the nominal noise is important to know such that normal noise can be distinguished from effects made by the servo motor.

The results shows that the measurements from the nominal magnetometer characterization experiment had many outliers. This was seen in Figure 5.1a. This is most likely a sensor fault, since the values are so large. It could either be due to a bad solder, bad wiring or other reasons. These outliers can be removed easily in the control algorithm, and will therefore not be addressed in further detail. Figure 5.1b shows that without the outliers, the magnetometer measurements visually looks like white noise.

The ACF and PACF plots in Figure 5.3 further showed that the magnetometer measurements can't be modelled in terms of an ARMA series. This is because the the autocorrelation and partial autocorrelation was inside the 95 % confidence interval from the first lag. It can therefore be concluded that the noise was random. The density plot in Figure 5.2 further indicates that the noise could follow a normal distribution, even though the y-axis measurements visually looked spikey. This could however be due to the large and lonely outlier in the measurements. The statistical values presented in Table 5.1a can be used to evaluate the normality of the data, however, due to the many outliers, which

normally would be detected and ignored in a control algorithm, the statistic does not give representative data for the samples used in a control algorithm. This is especially visible in the large excess kurtosis and standard deviations. Instead, we look at the data where the outliers have been removed in Table 5.1b.

First, it is observed that the norm of the magnetometer measurement mean was 31.81 μT, which is low, but still within what one could expect inside a building in Trondheim. The absolute value of the skew of the magnetometer data is less than 0.5, meaning the data set is approximately symmetric. The excess kurtosis of the measurements are all close to 0, but not perfectly zero. The skewness and kurtosis of the data set thereby also indicates that the noise can be assumed to be Gaussian. Together with the reflection on the ACF and PACF plots, it can be concluded that the magnetic field measurements can be assumed to be white, zero mean noise. The standard deviations was found to be 0.634 μT, 0.486 μT and 0.612 μT for the x-, y- and z- axis respectively.

The standard deviations of the measurement noise can be validated by the measured IMU time series before and after the servo motor actuation with and without load. The ranges for the standard deviations from the test statistics in Tables 5.2 and Tables 5.5 are summarized in Table 6.1. The range of measured standard deviations differs by up to 0.111 μT, which is less than the resolution of the magnetometer. The standard deviations concluded from the magnetometer measurement noise characterization is all within the ranges in Table 6.1. The nominal magnetometer noise standard deviations without magnetic disturbances can therefore be assumed to be somewhere between the observed minimum and maximum standard deviations observed in Table 6.1.

Table 6.1: Minimum and maximum standard deviations for the magnetometer measurements before and after each servo actuation experiment.

std	min [μT]	max [μT]
x	0.612	0.656
y	0.400	0.459
z	0.597	0.708

6.1.2 Gyroscope and accelerometer noise evaluation

The statistical properties of the gyroscope and accelerometer noise can be found using the data presented in Tables 5.3 and 5.4 (and A.1 and A.2). Although it was not vital to determine the accelerometer noise for the heading estimation of a planar snake robot, it was performed due to the profit the contribution brings to the Boa project in general.

The results shows clearly that the standard deviation of the gyroscope measurements were $\sigma_{gyro} = [0.001, 0.002, 0.001]$. The skew are all less than 0.2. The gyroscope noise is therefore symmetrical, since a common rule of

thumb from the literature is that a skew less than 0.5 means the dataset is close to symmetric. The value of the kurtosis varied between each experiment, also within one axis. The lowest measured kurtosis was as close to zero as 0.005, while the highest measured kurtosis was before the additional load experiment with the value 0.437. The variations could be due to the time series not being long enough for a stable measure of kurtosis, the amount of outliers in the data set or different amount of drift during each experiment. The literature is not consistent on at which range of kurtosis the data can be considered to be normally distributed. Some say ±1, others ±3. Since the kurtosis indeed was less than one, the gyroscope measurements can be assumed to follow the Gaussian distribution with the standard deviations described above.

The accelerometer measurements had standard deviations between $\sigma_{acc} = [0.009, 0.013, 0.015]$ and $\sigma_{acc} = [0.014, 0.015, 0.018]$. Since the skew is less than or equal than 0.5 before and after servo actuation, the noise can be assumed to be symmetric. The kurtosis was however at maximum 1.27, but also varied a lot with the lowest value of 0.035. Depending on the rule of thumb one use, the noise may or may not be assumed to be normally distributed. For all practical scenarios, modelling the accelerometer noise as Gaussian or with another distribution would most likely not make a big different, since the excess kurtosis still was significantly lower than 3. The filter can however no longer be assumed to yield the optimal solution. It is recommended to at least address the increased kursosis in further detail in future work. It will not be addressed in further detail here, as it is not necessary for the heading estimation in this work.

To summarize, the nominal IMU measurements was all concluded to be white Gaussian noise, when not subject to the induced electromagnetic field from the servo motor.

6.2 Validating previous work

The project work performed in the autumn of 2022, on the previous version of the Boa Snake robot, concluded that the accelerometer and gyroscope was not affected by the servo motor's generated electromagnetic field [19]. However, the results was inconclusive whether the accelerometer's measurement noise was correlated with the servo motor's shaft speed. It also concluded that the magnetic field generated from the motor could be modelled as a sine function of the motor shaft's angular position [19]. The previous work marked validating the results on additional motor load as future work. This section will focus on discussing the validation of these results on the new motor, both with and without additional torque load.

Before deep diving into the discussion, the scatter plots with the servo velocity in Figures 5.7 needs to be addressed. The evenly spaced lines are the servo speed increments in each experiment, as described in Section 4.4, and

spans almost the entire magnetic field span. The curves are where the motor accelerates. This is viewed in an interpreted plot for the y-axis magnetic field in Figure 6.1. The servo motor only changed its direction around 0° and 360°, meaning that it only accelerated and changed velocity around these positions as well. The complex patterns are thus a result of the experimental design, and should not be misread as anything else. The pattern can therefore not be used to model the magnetic cross-talk. To prevent the test-script from affecting the plot, a dedicated experiment could have been made, were the servo motor rotates continuously with a constant acceleration. However, since each pre-programmed angular velocity had the same span in the magnetic field measurements, it is concluded that there probably is no evident correlation.

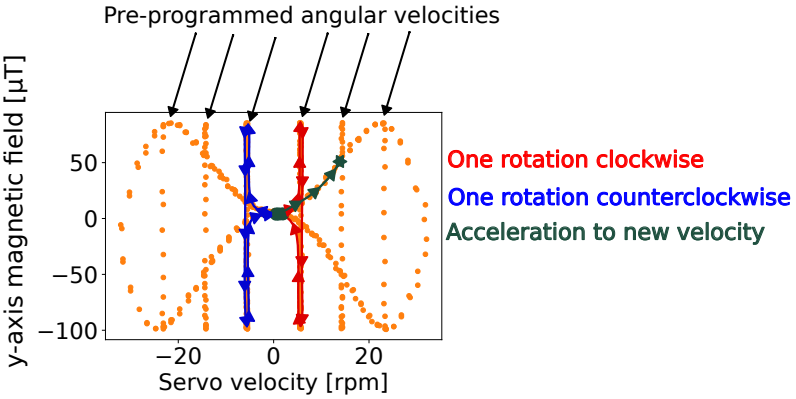

Figure 6.1: The complex patterns between the servo velocity and measured magnetic field is due to the design of the experiment. Between each new rotation, the motor changes its direction. When the motor has rotated with a pre-programmed velocity in each direction, it accelerated to a new, faster velocity.

6.2.1 Motor field impact on the accelerometer and gyroscope

The scatter plots showed no evident pattern between the servo motor's position, velocity, or torque current and the acceleration or gyroscope measurements, as could be seen in Figure 5.5 and the pair plots in Appendix A.1 and A.2. There was also no indication of the accelerometer's variance increasing with the motor's shaft speed. This makes sense since the strength of the electromagnetic field does not increase with increased speed of the motor, but rather the rate of change of the magnetic field, as shown in Figure 5.4.

The histograms in Figures 5.8 further showed that the accelerometer and gyroscope measurements remained approximately Gaussian during the servo actuation. Additionally, Tables 5.4 and 5.3 clearly showed that the mean and standard deviation of the gyroscope and accelerometer measurements in practice remained unchanged. The y-axis accelerometer mean however changed with $0.073\,\mathrm{m\,s^{-2}}$ during servo actuation. This is however so small it could be due to vibrations from the motor while the shaft rotated. It is therefore concluded

that the accelerometer and gyroscope measurements were not affected by the servo motor's generated electromagnetic field, as was also concluded in the previous project work on the previous motor [19].

6.2.2 Motor field impact on the magnetometer

The last part that had to be validated from the previous project work was the modelling of the magnetometer measurements during servo actuation. As expected, the time series in Figure 5.4 clearly showed that the magnetometer was affected by the servo motor's electromagnetic field. It was also observed from the results that there were no correlation between the measured magnetic field and the servo velocity or torque current.

The scatter plot in Figure 5.6 clearly revealed that the magnetic field along each measurements axes were correlated with each other, and that the magnetometer measurements followed a sine with respect to the servo motor's angular position. This is the same observation as in Linnerud for the previous Boa design [19]. It makes sense that the x- and y- axis magnetic fields were approximately the same scale, since the IMU was intentionally attempted to be mounted directly above the servo motor shaft. The elliptic correlation between each axis of the measured magnetic field also were as expected, since the measurement is a direct effect from the BLDC motor's generated electromagnetic field to rotate the motor's rotor. The magnetic disturbance from the motor thus makes perfect sense based on the theory. The modelling of the magnetic disturbance from the servo motor is further discussed in Section 6.3.

The results in Figure 5.9, comparing the IMU measurement before and after servo actuation, showed that the magnetometer measurements visually seems to have returned to its original value. Table 5.2 shows that the mean of the magnetic field after servo actuation, when the torque was disabled, changed with up to 1.531 µT. This is rather small in the engineering context, and it can be concluded that the calibration of the magnetometer is not damaged by the generated magnetic field from the servo motor.

It was expected that the magnetic field would be correlated with the torque current of the motor, based on the theory. An increased current in the coils should generate a larger magnetic field. This was however not observed. The reason could be due to the low motor load.

In conclusion, the servo motor seems to leave no permanent effect on the magnetic field measurements when the motor torque is disabled, and does not affect the gyroscope or accelerometer measurements. These results from the previous project work is thereby also valid with the new motor for the Boa snake robot.

6.2.3 Effects of additional motor load

The effect of additional load on the motor disturbance was not concluded in Linnerud [19], and was therefore investigated as part of this thesis. The effects of additional motor load, as presented in Section 5.3 will be further discussed in this section. Since additional load on the motor leads to increased torque current in the motor, the effects of additional load needed to be investigated. From Biot-Savrt's law, larger currents lead to a stronger magnetic field intensity. How large this change is in practice, was what the experiment tested.

To confirm that the experimental setup was able to emulate an additional load on the motor, the torque current during the additional load experiment was plotted against the torque current during the baseline experiment in Figure 5.10. The plot confirmed that the motor was subject to additional load because the torque current was larger than in the baseline motor actuation experiment.

The effect of adding load to the motor was hard to interpret using the pair plots in Appendix A.2, since the servo motor rotated a few degrees during the experiments. This made it hard to interpret which changes were due to the rotation, and which were due to the load. One can however assume that the accelerometer and gyroscope measurements were unaffected, as was concluded from the baseline experiments. Figure 5.11 showed that the magnetic field might have been stronger during the tests, but the difference could also be due to the differences in the IMU calibration between the tests with and without load. The pair plots indicated that it now may be a correlation between the measured magnetic field and the torque current. However, it does not make sense that the scatter plot with additional load shows gaps and signs of correlation, when the baseline experiment did have measurements in these areas. Adding the scatter plots on top of each other, as displayed in the interpreted plot in Figure 6.2 no correlations can be seen. This indicates that the observations were due to the design of the test script. It is concluded that increased torque current does not yield increased magnetic field

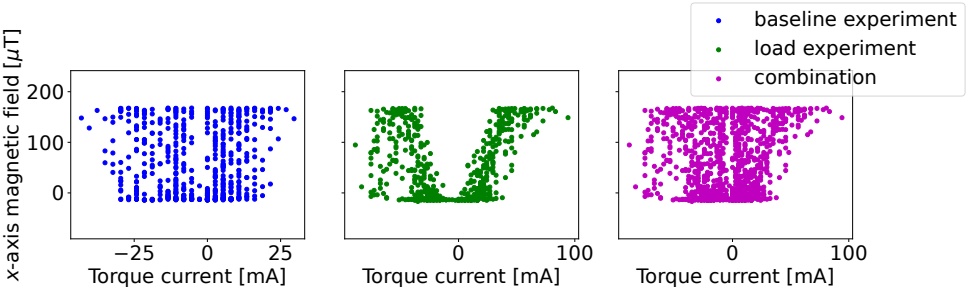

Figure 6.2: The experiments shows no correlation between the size of the measured magnetic field, and the torque current of the motor, although the additional load experiment on its own indicated that there might be a correlation.

In this case, a more effective way of investigating the effect of the added load is to compare the sine regressions of the generated magnetic field during the baseline experiment and the load experiment, using Figures 5.12 and 5.13 in Chapter 5.4. The modeled magnetic fields were almost identical. Additionally, as will be further discussed when evaluating the magnetic cross-talk model in Section 6.3, the model built on the data from the additional load experiment had lower residuals and RMSE than with the baseline experimental data. One can therefore assume that the magnetic cross-talk model does not need to include terms depending on additional motor load. It should however be noted that the amount of additional load was limited and that a higher load might give other conclusions. This would need to be validated when testing a multi-link snake robot once the hardware of the Boa snake robot links is available.

Table 5.5 showed that the measured magnetic field after servo actuation differed with approximately 2.5 µT in the z-direction from the nominal measurements sampled before servo actuation. This is not vital for the heading estimation in 2D, but will have an effect on heading estimation in 3D. This would need further assessment in future work if the Boa prototype design is ever developed for use in 3D.

6.3 Evaluating the magnetic cross-talk model

The results from modeling the magnetic cross-talk from the servo motor, as measured by the magnetometer, were presented in Section 5.4. The magnetic field was modeled using *SciPy's* `curve_fit` function. Note that the model parameters themselves depend on the distance between the IMU and servo motor, and the position of the IMU with respect to the center of the servo motor shaft. The fitted sines were plotted with the data points in Figure 5.12. The amplitudes of the x- and y- axis magnetic fields were both approximately 90 µT. The fact that the amplitudes were approximately similar are as expected, since the magnetic field of the BLDC motor rotates in the plane perpendicular to the rotational axis of the motor shaft. The offset of the x- and y-axis cross-talk model is however different. This could be due to the IMU not being mounted directly above the center of the rotor coils.

The model performance was evaluated by the Root Mean Square Error and residuals of the model on the training and test data. Testing the model on test data was crucial to validate the model. The standard deviation of the model residuals and RMSE on training and test data was presented in Table 5.6. The results showed that the RMSE was more than 3 µT for the x- and y-axis models, and around 1.9 µT for the z-axis model. The RMSEs were approximately equal for both the training set and the test set, in other words, the baseline experiment and the additional load experiment. This strongly indicates that the model is robust in terms of additional rotational load.

The RMSE values should preferably be lower. To try to understand why the RMSE values were so large, the motor residuals in Figure 5.14 should be considered. The plot clearly showed that the residuals increased with the motor's shaft velocity. It is most likely the deviations of up to 10 µT at the end of the time series (where the motor shaft speed was highest) that gave the large RMSE values. In the previous discussion, one does however not observe any evident correlations between the magnetic field magnitude and the motor velocity or current. On the other hand, if one compares the residuals with the magnetic field measurements, the residuals show the same periodic pattern, but time-shifted. This interpretation is illustrated in Figure 6.3.

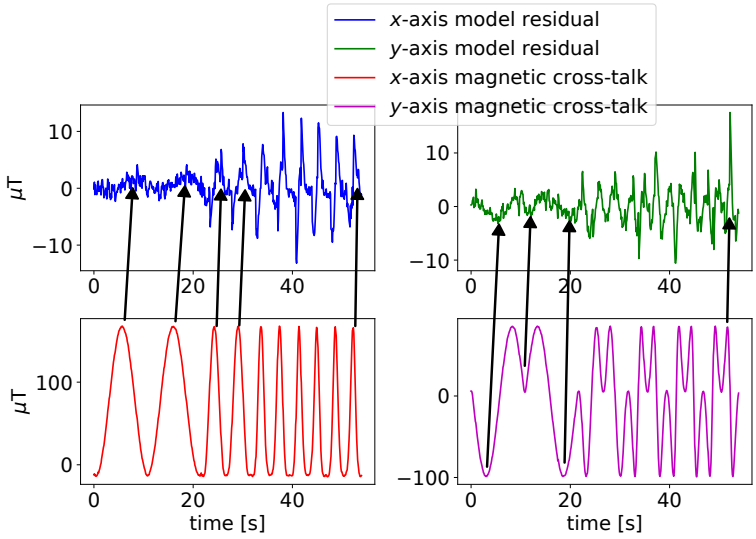

Figure 6.3: The residuals of the cross-talk model peaks of the residuals are time shifted, with respect to the measured magnetic field. The residuals are therefore most likely an effect of a changing back EMF in the BLDC motor.

Figure 6.3 illustrates, with arrows, that it seems like the peaks of the model residuals are time-shifted versions of the measured magnetic field when the was actuated. Remember that during the experiment, the motor shaft performed one rotation in each direction before it did the same movement several times at different speeds. The figure shows that the time shift became smaller and the residuals larger when the motor's magnetic field had a larger rate of change at the end of the time series. As stated by Faradays's law, described in the theory, a changing magnetic field will induce an electromotive force opposing the change in magnetic field, and thereby a back EMF voltage in the rotor coils. This further changes the observed magnetic field since the current in the coils will be affected by the back EMF. The back EMF is proportional to the rate of change of the magnetic field. Therefore, it is believed that the increased residuals that were observed when the shaft's angular velocity increased are a direct effect of the cross-talk model not considering the magnetic field from the back EMF voltage.

Unfortunately, it was not attempted to model the magnetic field in relation to the back EMF voltage. Instead, other methods to reduce the residuals were tested by performing the shielding experiments and adding magnetic disturbance rejection to the Kalman filter in the heading experiment. The effectiveness of these methods will be discussed in Section 6.4 and 6.5.

6.4 Effectiveness of shielding

The shielding experiments aimed at improving the heading estimates by either improving the cross-talk model or by attenuating the magnetic cross-talk. The nominal magnetic field was measured before each servo actuation following the test script used.

The nominal magnetometer measurements that were performed before the servo actuation, shown in Figure 5.15, clearly showed that the in-built magnetometer calibration of the *BNO-055* was inconsistent. Even when no ferrite sheets were near the IMU or the servo motor, the x-, y- and z- axis did not show consistent readings. Throughout the experiments, the servo motor maintained a consistent orientation, with variations only occurring during the calibration process. The calibration sets the initial magnetometer measurements, which further affects the offset between each measurement when the servo motor actuated. Why the calibration was bad is hard to say, since the IMU reported good calibration when the experiments were conducted. It could be due to surrounding metals, or the ferrite sheets. The bad calibration would need to be assessed in future work. Due to the differences in the nominal measured magnetic field and calibration, the effectiveness of shielding and distance could not be evaluated by the pure size of the magnetometer measurements. It was therefore chosen to build cross-talk models from the different experiments and evaluate the shielding methods using the estimated servo motor field and model residuals.

The hope was that by adding shielding sheets, the model residuals would reduce to White Gaussian Noise, or at least yield lower RMSE compared to those without shielding. When shielding sheets was employed, Figure 5.16 clearly showed that the residuals deviated from white noise characteristics. However, the magnitude of the residuals no longer increased with higher motor velocities but rather decreased. The residuals were actually higher with lower motor velocity during the shielding experiments than without shielding. In retrospect, this makes sense since shielding works better with higher frequencies. However, since the sheets were ferrite sheets, it was expected that the shielding would be able to contain the low-frequency magnetic field where the motor shaft rotated at a slower rate.

The introduction of shielding additionally resulted in a more unpredictable cross-talk in terms of the magnetic field against the motor's angular position.

This was clearly observed in Figure 5.18 from the experiment with 0.1 mm shielding sheet. The magnetic field during the different angular positions varied more than without shielding. Modeling the magnetic cross-talk would not be reliable with these effects. By adding more ferrite sheets, the variance of the sine model decreased. The accuracy of the models was however compromised as seen by the RMSE values of the models in Table 5.7. The RMSE values were higher with shielding than during the baseline setup, with a maximum RMSE of 4.350 μT.

Adding physical distance of only 10 mm and 20 mm proved to reduce the RMSE values of the magnetic cross-talk model more effectively than with shielding sheets. Figure 5.17 showed that the residuals were lower than with the baseline setup, also when the servo shaft velocity was higher at the end of the time series. The RMSE values were also significantly lower than without additional distance. The RMSE of the cross-talk model with 20 mm distance between the IMU and motor was around 1 μT. Considering the nominal magnetometer measurement noise was around 0.7 μT, this is a really good result. Following Biot-Savart's law, the decreased RMSE makes sense as the magnetic field intensity is inversely proportional to the square of the distance to the magnetic source. If the residuals indeed were following Faraday's law, this would describe why distance improved the model residuals, while the shielding sheets made the model residuals worse.

To conclude, adding distance made the cross-talk model more reliable than the shielding sheets did. Considering the significant cost and the added weight of shielding sheets, and their associated complications in modeling the magnetic disturbance from the servo motor, it can be concluded that shielding sheets should not be used. The consequence of additional distance is however that the snake robot will become bulkier.

6.5 Evaluation of the heading estimation method

The proof-of-concept heading experiment gave a clear indication of the performance of the magnetic disturbance compensation technique proposed in Section 4.6. The results compared four different heading estimators and the pseudo measurement of the heading, both with and without a feed-forward loop. The goal was to evaluate the effects of feed-forwarding the predicted cross-talk term by the quality of the estimates. The cross-talk was predicted with the model created in Phase 3 of this work. The experiment did not have a ground truth due to the limitations in the experimental setup. The heading of the experimental setup was however known to have an initial heading of approximately $-70°$, and the motion profile was as described in Section 4.6.

The heading estimators compared in the results were

1. The *BNO-055*'s own heading estimate, serving as a reference. The results showed that the heading itself was completely wrong, but the relative movement performed during the experiments were captured by the estimator. The BNO most likely only used the gyroscope measurements for the estimation, due to its similarity to ”KF tuning 1”.
2. ”KF tuning 1”: a standard Kalman filter tuned to not use the magnetic field measurements. The tuning was overconfident in the plant model and updated its estimate using the gyroscope measurement only. This was concluded based on the heading experiment, the stationary time series, and the heading estimate not using feed-forward in Figures 5.20 and 5.21.
3. ”KF tuning 2”: a standard filter, tuned to obtain the best possible heading estimate using feed-forward, but without magnetic field rejection.
4. ”KF with MDR”: This heading estimator used an adaptive Kalman filter, inspired by the literature review [17, 50]. The ”KF with MDR” adaptively changed its measurement covariance matrix to reject magnetic disturbances using the rules described in Section 4.6.2. This Kalman filter, used in combination with the feed-forward term and cross-talk model, gave the best results.

The results showed that the first Kalman filter tuning and the BNO estimate had almost identical shapes, but different initial values for the heading estimation. Even in the absence of magnetic disturbances, the heading estimates were significantly inaccurate for both the BNO estimate and the first Kalman filter tuning. The results thereby showed that not using the magnetic field measurements at all due to the magnetic disturbances is a bad idea, as it makes the estimator prone to a constant bias in case of bad initialisation.

The second Kalman filter tuning showed that even with feed-forward, the heading estimate would be unreliable using a conventional Kalman filter, due to modeling errors. This could be seen in Figure 5.20 from 20 s and through the rest of the experiment, where the motor shaft had the highest velocities, and the cross-talk model was known to have the largest residuals. By adding magnetic disturbance rejection, these modeling errors were compensated for. The adaptive Kalman filter with magnetic disturbance rejection (”KF with MDR”) was thereby the heading estimator with the best estimates, as long as feed-forwarding of the magnetic cross-talk model was performed. However, the results of using the ”KF with MDR” without the feed-forward loop, as was shown in the right plot of Figure 5.20, showed that the estimates were biased, or wrong through most of the experiment. Omitting the feed-forward loop before estimating the heading would therefore provide unreliable heading estimates. This shows that utilizing both an adaptive Kalman filter and the magnetic cross-talk model is crucial to make the heading estimator reliable when the servo motor actuates.

Since the heading experiment did not have a ground truth, the real performance of the adaptive Kalman filter with MDR, henceforth called the proposed method, cannot be evaluated. However, it is evident that the proposed method has the smallest estimation error based on the prior information of the movement in the experiments. The relative heading of the experimental setup can be assumed to be captured precisely enough by the *BNO-055* estimate and the overconfident Kalman filter in the first tuning. The proposed method had almost the same relative heading, but the value of the heading estimate itself was closer to the initially known heading which were approximately $-70°$. The experiment was therefore able to serve as a proof-of-concept to show that the heading estimates were improved using the proposed heading estimator.

A quick note on the magnetic cross-talk model used in the heading estimates is in order. The magnetic cross-talk model was re-fit in advance of the heading experiment. It was decided to do it this way because the IMU was moved between the baseline and additional load experiments, and the physical shielding experiments before the heading experiment was conducted. Additionally, the standard deviation of the residuals of the cross-talk model was used as a starting point to tune the measurement covariance matrix. However, it is very important to be aware that the modeling error yields non-Gaussian magnetic field measurement noise. The Kalman filter will therefore not yield the optimal solution for the heading estimator problem. However, the magnetic disturbance rejection reduces the noise further. Although the Kalman filter no longer is theoretically optimal, the proposed method showed an improvement of the heading estimates in a practical setting.

6.5.1 Notes on the heading estimator design

The chosen filtering technique of the magnetic disturbance from the servo motor was not an evident choice. In the literature review, only one of the reviewed magnetic rejection techniques dealt with the magnetic field from a vehicle's own motors. Widey and Woo filtered the motor's magnetic field when the RPM of the UAV motors was sufficiently higher than the dynamics of the system [50]. This was however not possible for the Boa snake robot, as the rotational speed of the servo motor per definition *is* the dynamics of the system. Instead, the feed-forward-loop-approach was chosen. Due to the observed residuals of the cross-talk model, the Kalman filter with magnetic disturbance rejection was used in combination with the feed-forward loop to handle the modeling error, inspired by the Wondosen *et al.* and Widey and Woo in the literature review [17, 50]. The work in this thesis has successfully improved the heading estimates by introducing this new proposed method. There are however a few weaknesses in the design which should be addressed.

First, the cross-talk from the motor poses the weakness that it is easily changed or affected by surrounding metals. When the motor changes its

magnetic field to rotate, it will induce eddy currents in surrounding metals. Following Lentz's law, this will create a magnetic field counteracting the change, and thereby distort the sensed magnetic field from the servo motor. This was observed in the attempt of improving the experimental setup of the heading experiment. Figure 5.22 showed that the magnetic disturbance from the servo motor spreads by roughly $30\,\mu T$ when the motor was mounted on a metallic camera tripod. The magnetic cross-talk most likely induced eddy currents in the camera stand, making the cross-talk to the IMU less predictable. To prevent this problem from being a permanent issue for the navigation of the snake robot, it is important that the hardware of the robot contains as little conductive or magnetic metals as possible. External, temporary environmental magnetic fields can however be handled by the adaptive Kalman filter. This is another reason to use the adaptive design rather than a standard Kalman Filter.

The filter is further greatly reliant on proper initialization without disturbance. Without this, there is a risk that the filter will use a long time to converge to the correct heading angle. Without disturbance, the filter used 3 seconds to converge, as seen in Figure 5.21. With magnetic disturbances, the left plot of Figure 5.20 showed that the Kalman filter with magnetic disturbance rejection used about 5 seconds to converge. However here, the IMU was only subject to the known magnetic field with low model residuals. If there are strong disturbances or external magnetic fields while the filter converges to the correct angle, the magnetic field measurements will be rejected, and the error will propagate in the filter until the magnetic disturbance is gone. Letting the Kalman filter converge before operating the snake robot is therefore crucial for the navigation of the robot.

6.6 Proposed technique for improved heading estimation

Based on the results from all the experiments, the proposed method to improve the heading estimates can be summarized as follows. Figure 4.6 in Chapter 4 may serve as a supplement to the description.

Hardware material selection and distance between the IMU and the motor: The first step is to attenuate the magnetic cross-talk from the motor as much as possible by increasing the distance between the servo motor and the mounting of the IMU. Additionally, since it was known that metals will interact with the magnetic field and make the field more unpredictable, the chassis of the Boa snake robot should limit the use of conductive materials or metals with high magnetic permeability.

Model the magnetic disturbance from the motor: Once the distance between the IMU and servo motor is maximized, the magnetic corss-talk from the motor can be modelled. This step is crucial to perform using the correct mounting and chassis of the snake robot link, such that the sensed magnetic field by the IMU from the servo motor is correct.

Predict the magnetic disturbance from the motor: Using the model acquired in the previous step, it is possible to predict the magnetic disturbance from the motor in loop. Since magnetic fields are additive, the magnetometer measurements can be corrected in a feed-forward loop by subtracting the predicted field from the measurements.

Reject magnetic disturbances using an adaptive Kalman filter: Although any model will never be perfect, and because any surrounding metals or magnetic fields in the environment will disturb the heading estimation, it is crucial to detect and reject these disturbances and modelling errors. This work proposes two rules to adaptively increase the measurement covariance matrix of the Kalman filter to ensure that the state estimates are not updated based on disturbed data. The two rules were to increase the initial heading measurement covariance by 1) adding a multiple of the square error of the predicted and measured heading, and 2) adding a multiple of the square error of the measured and expected norm of the magnetic field.

Proper initialization of the Kalman filter: Even with the feed-forward loop, the Kalman filter will use time to converge towards the correct initial heading estimate. It is therefore recommended to let it converge after initialization before enabling the torque of the snake robot motors. It is also recommended that the torque from all of the motor are disabled once in a while during operation, to let the heading estimates be corrected in case of drift.

It is also worth mentioning that the Boa snake robot, which uses servo motors as the joint between each link, has the great advantage that the servo motors can give valuable information about the angle and angle rate of the servo motors at each time step. This data can be used as odometry to further improve the attitude and position estimates of the snake robot.

The Kalman filter should of course, be tailored for the attitude and spacial position estimation. In this work, the linear Kalman filter was used since it was possible to linearize the plant model using pseudo measurements. For the full attitude and position estimates, a nonlinear Kalman filter such as the Extended Kalman Filter should be used. Additionally, state estimates should include the gyro bias to avoid drift, even though it was omitted in this work for simplicity.

6.7 Choice of method and scope

The goal of this work was to improve the heading estimates of the planar Boa snake robot, where the IMU was mounted near the servo motor joints. The scope was narrowed by only focusing on one motor and IMU. Additionally, some work were attributed to how the the accelerometer was affected by the motor field, since this was not concluded in the previous work, and is crucial for the force estimation for the obstacle based locomotion of the Boa.

The decision to focus exclusively on a single motor was wise for several reasons. Firstly, the approach undertaken proved to be highly comprehensive. Initially, considerable time was dedicated to validating the previous work. It involved creating new test scripts specifically tailored for the new motor, and designing the test rig for the additional load experiment. This validation process was time-consuming. However, it laid a solid foundation for subsequent steps. Notably, leveraging the validated work facilitated the identification of IMU measurement noise, ultimately streamlining the process of tuning the Kalman filter. Furthermore, the validation of the prior work served as a starting point for modeling the magnetic disturbance induced by the motor.

The test script design was as general as possible. This made it usable for validating previous work, modeling the magnetic disturbance from the motor, performing the shielding experiments, and performing the experiment for testing the proposed method of improved heading estimation. This saved a lot of time and made it easier to compare the performance of shielding. Furthermore, it simplified the evaluation of the heading estimates, as it was known where the motor field model would have larger residuals.

The investigation of physical magnetic disturbance attenuation techniques didn't yield the expected results, especially when it comes to the shielding sheets. However, the shielding experiments in combination with the attempted improvement in the setup with the camera tripod for the heading experiment,

gave a better understanding of how the hardware of the Boa will affect the heading estimates. It showed how important it is for the snake robot to consist of as little metals as possible, to make the proposed method in this work more reliable.

Lastly, the proof of concept heading estimation experiments needs to be addressed, both in terms of the experimental design, and the heading estimator design. Due to the time frame of the thesis, there would not have been time to set up an experiment in a motion lab or develop a test stand and test script where the movement of the IMU and servo motor was linked to the servo shaft's rotation. The chassis of a Boa link was also not available. Despite the limited availability of proper test rigs, making the proof-of-concept experiment, using the same test script, and moving the motor and IMU by hand, gave the data necessary to test the proposed heading estimation technique. The fact that the heading estimators used on the proof-of-concept data are of the most basic Kalman filter design shows that the proposed technique of correcting the magnetic field measurements makes it possible to yield good heading estimates. If the method is applied to a more sophisticated Kalman filter with data from the actuators and a more correct plant model, the heading estimation would most likely become even better.

6.8 Future work

The work in this thesis concluded with a proposed method to improve the heading estimates in the presence of strong magnetic fields from the vehicle's own motors. Future work should test this method in attitude and spacial orientation estimates on a multi-link snake robot. This way, the proposed technique can be tested in more realistic conditions where multiple motors actuates simultaneously. Having typical magnetic objects in a physical simulated environment would be an interesting assessment for an even more realistic investment. Future work could also assess the possibility to use the Double Quaternion Extended Kalman filter proposed by Wondosen *et al.* [17]. The plant model of the robot can also be improved by using the position and velocity of the servo motor's as odometry. This would however need a non-linear Kalman filter implementation.

For future work directly on the Boa snake robot, further investigation is recommended regarding the inconsistent nature of the auto-calibration feature of the *BNO-055* IMU. The calibration proved to be a hard task *in situ*. Even when the auto calibration reported good calibration, the magnetometer reported inconsistent magnetic fields. Lastly, the accelerometer noise should be investigated further, as the analysis showed that the excess kurtosis was over one. This is vital for the attitude and force estimation used to navigate the robot using obstacle aided locomotion.

Chapter 7

Conclusion

This work has successfully demonstrated a general approach to improve the heading estimates in the presence of a disturbing magnetic field from surrounding electric motors in small vehicles such as snake robots. The study was performed using the *Dynamixel XH540-V150-R* BLDC servo motor, and the *BNO-055* IMU, used on the Boa snake robot.

By performing a proof-of-concept heading experiment, it was concluded that the heading estimates were significantly improved by predicting the magnetic cross-talk from the servo motor to correct the magnetic field measurements in a feed-forward loop. By using a Kalman filter that adaptively changes its measurement covariance matrix to reject magnetic disturbances, the modeling error and external magnetic fields are rejected by the method. The absence of either the feed-forward compensation or the magnetic disturbance rejection rule made the heading estimates unreliable when the servo motor was actuated. Both methods should therefore be used in combination to obtain the best heading estimation results.

The magnetic cross-talk was modeled as a sine wave as a function of the BLDC motor's shaft position. The model was fit using non-linear least squares regression with *Scipy's* `curve_fit` function. The data used to model the magnetic cross-talk was obtained from a baseline experiment where the motor shaft rotated with pre-defined speed profiles while the motor housing and IMU themselves remained stationary. The model was validated to work with an additional rotational load on the motor. The maximum RMSE of the model was 3.316 μT. The residuals grew with the absolute value of the motor's shaft velocity, and it was concluded that these residuals most likely came from the back emf in the motor.

Physical shielding methods were tested to reduce these residuals. It was concluded that the expensive ferrite shielding sheets of 0.5 mm attenuated the magnetic field approximately as much as 20 mm of additional distance between

the motor and the IMU. However, the shielding sheets made the cross-talk from the motor harder to predict in terms of the amplitude and offset parameters. Using additional distance, on the other hand, decreased the maximum RMSE of the cross-talk model to 1.097 μT. It was therefore recommended to maximize the distance between the IMU and the motor as much as the design of the robot allows before building the cross-talk model. The proposed method requires the cross-talk model to be built for each individual snake robot link, preferably in a lab without environmental magnetic disturbances, before being incorporated into the heading estimator.

This work also validated the previous project work on the Boa snake robot with the new motor and characterized the nominal IMU measurement noise. Although the literature review suggested that the magnetometer noise might need to be modeled as an ARMA series, the nominal IMU measurement was determined to have White Gaussian Noise. By comparing the nominal noise with the measurement noise while the servo motor was actuated, it was validated that the accelerometer and gyroscope measurements were not affected by the strong magnetic field.

This work has shown that it is possible to acquire good heading estimates with a low-cost IMU by modeling the magnetic disturbances from the motor. Future work should test the proposed method on a multi-link snake robot, testing the method in attitude and spatial orientation estimation. The contribution of this work will make it easier for the research group working on the Boa snake robot to develop attitude and spatial orientation estimation algorithms. Overall, the developed method would be suitable to improve the heading estimates, not only for snake robots but also other small, low-cost vehicles with electric motors and IMUs mounted nearby.

Bibliography

[1] M. Linnerud, *Magnetic-noise-compensation*. [Online]. Available: https://github.com/Boa-Snake-Robot/Magnetic-Noise-Compensation (visited on 07/13/2023).

[2] Robotis Co. Ltd, *Dynamixel sdk*. [Online]. Available: https://emanual.robotis.com/docs/en/software/dynamixel/dynamixel_sdk/overview/ (visited on 06/16/2023).

[3] Robotis Co. Ltd, *Python read write protocol 2.0*. [Online]. Available: https://emanual.robotis.com/docs/en/software/dynamixel/dynamixel_sdk/sample_code/python_read_write_protocol_2_0/#python-read-write-protocol-20 (visited on 06/16/2023).

[4] *Fusion 360*, Autodesk Inc, Jan. 8, 2022. [Online]. Available: https://www.autodesk.com/products/fusion-360/.

[5] *Original prusa i3 mk3s+*, Prusa Research, Jul. 13, 2023. [Online]. Available: https://www.prusa3d.com/category/original-prusa-i3-mk3s/.

[6] The pandas development team, *Pandas-dev/pandas: Pandas*, Feb. 2020. DOI: 10.5281/zenodo.3509134. [Online]. Available: https://doi.org/10.5281/zenodo.3509134.

[7] M. Waskom, *Seaborn: Statistical data visualization*, version JOSS paper, Mar. 2021. DOI: 10.5281/zenodo.4645478. [Online]. Available: https://doi.org/10.5281/zenodo.4645478.

[8] S. Seabold and J. Perktold, "Statsmodels: Econometric and statistical modeling with python," in *9th Python in Science Conference*, 2010.

[9] *Scipy.optimize.curve_fit — SciPy v1.10.0 Manual*. [Online]. Available: https://docs.scipy.org/doc/scipy/reference/generated/scipy.optimize.curve_fit.html (visited on 02/16/2023).

[10] P. Virtanen *et al.*, "SciPy 1.0: Fundamental Algorithms for Scientific Computing in Python," *Nature Methods*, vol. 17, pp. 261–272, 2020. DOI: 10.1038/s41592-019-0686-2.

[11] J. D. Hunter, "Matplotlib: A 2d graphics environment," *Computing in Science & Engineering*, vol. 9, no. 3, pp. 90–95, 2007. DOI: 10.1109/MCSE.2007.55.

[12] *Inkscape*, version 1.2.1, Jul. 5, 2023. [Online]. Available: https://inkscape.org/.

[13] *Google drawings*, Google, Jul. 5, 2023. [Online]. Available: https://docs.google.com/drawings/.

[14] *Draw.io*, version 21.5.1, JGraph Ltd and draw.io AG, Jul. 5, 2023. [Online]. Available: https://www.drawio.com/about.

[15] P. Chavan *et al.*, "Modular snake robot with mapping and navigation: Urban search and rescue (usar) robot," in *2015 International Conference on Computing Communication Control and Automation*, 2015, pp. 537–541. DOI: 10.1109/ICCUBEA.2015.110.

[16] D. A. Schreiber *et al.*, "Arcsnake: An archimedes' screw-propelled, reconfigurable serpentine robot for complex environments," in *2020 IEEE International Conference on Robotics and Automation (ICRA)*, 2020, pp. 7029–7034. DOI: 10.1109/ICRA40945.2020.9196968.

[17] A. Wondosen *et al.*, "Improved attitude and heading accuracy with double quaternion parameters estimation and magnetic disturbance rejection," *Sensors*, vol. 21, no. 16, p. 5475, Aug. 13, 2021, ISSN: 1424-8220. DOI: 10.3390/s21165475. [Online]. Available: https://www.mdpi.com/1424-8220/21/16/5475 (visited on 03/13/2023).

[18] J. Løwer *et al.*, "Proprioceptive contact force and contact point estimation in a stationary snake robot," *IFAC-PapersOnLine*, vol. 55, no. 38, pp. 160–165, 2022, 13th IFAC Symposium on Robot Control SYROCO 2022. DOI: https://doi.org/10.1016/j.ifacol.2023.01.149. [Online]. Available: https://www.sciencedirect.com/science/article/pii/S240589632300157X.

[19] M. Linnerud, "Characterizing electromagnetic noise from a servo motor onto the imu measurements in the boa snake robot," Project thesis, Norwegian University of Science and Technology, 2023.

[20] P. Liljebäck, "Modelling, development, and control of snake robots," Ph.D. dissertation, The Norwegian University of Science and Technology, 2011.

[21] M. Sadiku and S. Nelatury, *Elements of Electromagnetics* (The Oxford Series in Electrical and Computer Engineering), 7th ed. New York, NY: Oxford University Press, Jan. 2021.

[22] *Difference between an Electromagnet and a Permanent Magnet*, Jun. 2020. [Online]. Available: https://www.stanfordmagnets.com/difference-between-an-electromagnet-and-a-permanent-magnet.html (visited on 12/12/2022).

[23] J. E. García-Farieta and A. H. Márquez, "Exploring the magnetic field of helmholtz and maxwell coils: A computer-based approach exploiting the superposition principle," *Revista Brasileira de Ensino de Física*, vol. 42, 2020. DOI: 10.1590/1806-9126-RBEF-2020-0282. [Online]. Available: https://doi.org/10.1590/1806-9126-RBEF-2020-0282.

[24] B. Sun *et al.*, "Correlating the microstructure of mn–zn ferrite with magnetic noise for magnetic shield applications," *Ceramics International*, vol. 49, no. 8, pp. 11 960–11 967, 2023, ISSN: 0272-8842. DOI: https://doi.org/10.1016/j.ceramint.2022.12.045. [Online]. Available: https://www.sciencedirect.com/science/article/pii/S0272884222044406.

[25] *WE-FSFS flexible sintered ferrite sheet*, Order No. 364004, Wurth Elektronik eiSos GmbH & Co. KG.

[26] Iova State University. "Nondestructive evaluation techniques : Eddy current testing." (2023), [Online]. Available: https://www.nde-ed.org/NDETechniques/EddyCurrent/ProbesCoilDesign/ProbesShielding.xhtml (visited on 07/11/2023).

[27] A. R. Hambley, *Electrical engineering : principles and applications*, eng, 5th ed. Boston: Pearson, ISBN: 9780132155168.

[28] P. Yedamale, "Brushless dc (bldc) motor fundamentals," *Microchip Technology Inc*, vol. 20, no. 1, pp. 3–15, 2003.

[29] M. N. Armenise *et al.*, *Advances in Gyroscope Technologies*, 1. edition. Berlin, Heidelberg: Springer-Verlag, 2011, vol. 9783642154935, ISBN: 364215493X.

[30] Bosch, *Smart sensor: Bno055*. [Online]. Available: https://www.bosch-sensortec.com/products/smart-sensors/bno055/ (visited on 10/22/2022).

[31] K. B. Lee, *Principles of Microelectromechanical Systems* (Wiley - IEEE), en. Hoboken, NJ: Wiley-Blackwell, Jan. 2011.

[32] G. Langfelder and A. Tocchio, "Operation of lorentz-force MEMS magnetometers with a frequency offset between driving current and mechanical resonance," *IEEE Transactions on Magnetics*, vol. 50, no. 1, pp. 1–6, 2014. DOI: 10.1109/TMAG.2013.2281404.

[33] A. Elzwawy *et al.*, "Current trends in planar hall effect sensors: Evolution, optimization, and applications," *Journal of physics D: Applied Physics*, vol. 54, no. 35, Sep. 2021. DOI: 10.1088/1361-6463/abfbfb.

[34] P. Semiconductors, *I2c manual*, Version 2.0, 2003.

[35] T. Instruments, *Rs-485 reference guide*, Revision A, 2014. [Online]. Available: https://web.archive.org/web/20180517101401/http://www.ti.com/lit/sg/slyt484a/slyt484a.pdf.

[36] R. E. Walpole *et al.*, *Probability and statistics for engineers and scientists*, 9th ed. Upper Saddle River, NJ: Pearson, Dec. 2010.

[37] X. Luo, *GPS Stochastic Modelling: Signal Quality Measures and ARMA Processes* (Springer Theses). Berlin, Heidelberg: Springer, 2013, ISBN: 978-3-642-34836-5.

[38] G. E. Box, G. M. Jenkins, and G. C. Reinsel, *Time Series Analysis: Forecasting and Control, Fourth Edition*, eng. Wiley, 2008, ISBN: 9780470272848.

[39] Z. Ning *et al.*, "Improved MEMS magnetometer adaptive filter noise reduction and compensation method," *IEEE Sensors Journal*, vol. 22, no. 2, pp. 1252–1264, Jan. 2022, Conference Name: IEEE Sensors Journal, ISSN: 1558-1748. DOI: 10.1109/JSEN.2021.3130652.

[40] A. D. Ho and C. C. Yu, "Descriptive statistics for modern test score distributions: Skewness, kurtosis, discreteness, and ceiling effects," *Educational and psychological measurement*, vol. 75, no. 3, pp. 365–388, 2015.

[41] "Scipy.stats.kurtosis — SciPy v1.10.1 manual." (2023), [Online]. Available: https://docs.scipy.org/doc/scipy/reference/generated/scipy.stats.kurtosis.html (visited on 06/09/2023).

[42] "Pandas.DataFrame.kurtosis — pandas 2.0.2 documentation." (2023), [Online]. Available: https://pandas.pydata.org/docs/reference/api/pandas.DataFrame.kurtosis.html (visited on 06/09/2023).

[43] E. Brekke, "Fundamentals of sensor fusion: Target tracking, navigation and slam," *Teaching material for future course in sensor fusion, NTNU*, 2018. [Online]. Available: https://folk.ntnu.no/edmundfo/msc2019-2020/sf13chapters.pdf.

[44] J. Nocedal and S. Wright, *Numerical Optimization* (Springer Series in Operations Research and Financial Engineering), en, 2nd ed. New York, NY: Springer, Jul. 2006.

[45] *Sine fitting*. [Online]. Available: https://se.mathworks.com/matlabcentral/fileexchange/66793-sine-fitting (visited on 02/16/2023).

[46] T. Chai and R. R. Draxler, "Root mean square error (rmse) or mean absolute error (mae)? – arguments against avoiding rmse in the literature," *Geoscientific Model Development*, vol. 7, no. 3, pp. 1247–1250, 2014. DOI: 10.5194/gmd-7-1247-2014. [Online]. Available: https://gmd.copernicus.org/articles/7/1247/2014/.

[47] K. Esbensen *et al.*, *Multivariate Data Analysis: An Introduction to Multivariate Analysis, Process Analytical Technology and Quality by Design*. CAMO., 2018, ISBN: 9788269110401. [Online]. Available: https://books.google.no/books?id=VRqTtgEACAAJ.

[48] R. W. Beard and T. W. McLain, *Small unmanned aircraft*, en. Princeton, NJ: Princeton University Press, Feb. 2012.

[49] T. I. Fossen, *Handbook of marine craft hydrodynamics and motion control*. Wiley, Jun. 2021.

[50] A. Widy and K. T. Woo, "Robust attitude estimation method for underwater vehicles with external and internal magnetic noise rejection using adaptive indirect kalman filter," *2017 IEEE/RSJ International Conference on Intelligent Robots and Systems (IROS)*, pp. 2595–2600, 2017.

[51] MyActuator, *RMD-X6 1:6*. [Online]. Available: `https://www.myactuator.com/product-page/rmd-x6` (visited on 12/10/2022).

[52] Robotis Co. Ltd, *Robotis e-manual: Xh540-v150-r*. [Online]. Available: `https://emanual.robotis.com/docs/en/dxl/x/xh540-v150/#specifications` (visited on 06/16/2023).

[53] Bosch, *Bosch sensortec tutorials: How to calibrate the absolute orientation sensor bno055*. [Online]. Available: `https://www.youtube.com/watch?v=Bw0WuAyGsnY` (visited on 10/22/2022).

[54] Adafruit, *Adafruit bno055 absolute orientation sensor - overview*. [Online]. Available: `https://learn.adafruit.com/adafruit-bno055-absolute-orientation-sensor/arduino-code?view=all` (visited on 10/22/2022).

Appendix A

Additional results from the servo actuation experiments

Multiple plots and results that served to make the conclusions of this work was not presented in the results Chapter 5, *Results*, to avoid filling the chapter with large plots or numbers which could be shown in a more concise way with the supplement of words. They are presented in this appendix for the interested reader.

A.1 Pair plots during servo actuation in the baseline experiment

Seaborn's `pairplot` function [7] was used to make scatter and histogram plots of each feature to easily get an overview of the servo motor's effect on the IMU measurements. The pair plots in Figures A.1, A.2 and A.3 displays the pairplots that gave the starting points for the analysis and results from the baseline experimental results.

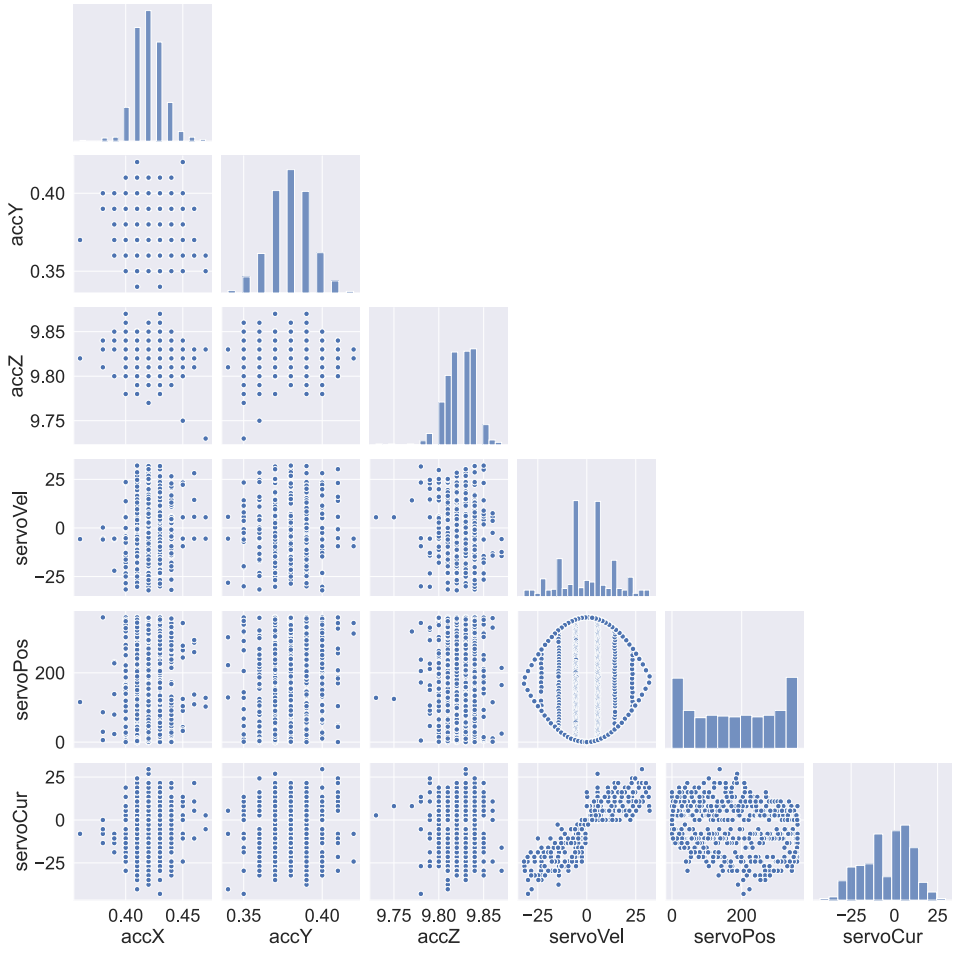

Figure A.1: Pair plot between the accelerometer measurements and the gyroscope measurements from the baseline experiment.

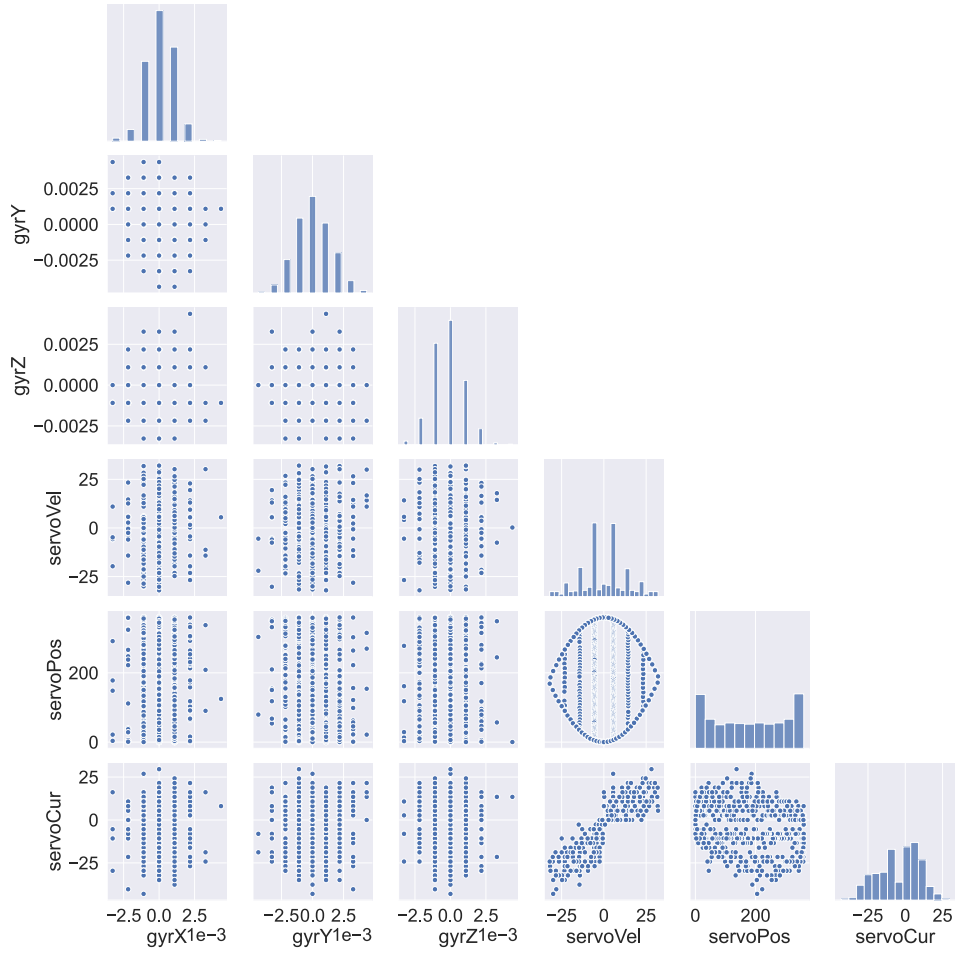

Figure A.2: Pair plot between the servo measurements and the gyroscope measurements from the baseline experiment.

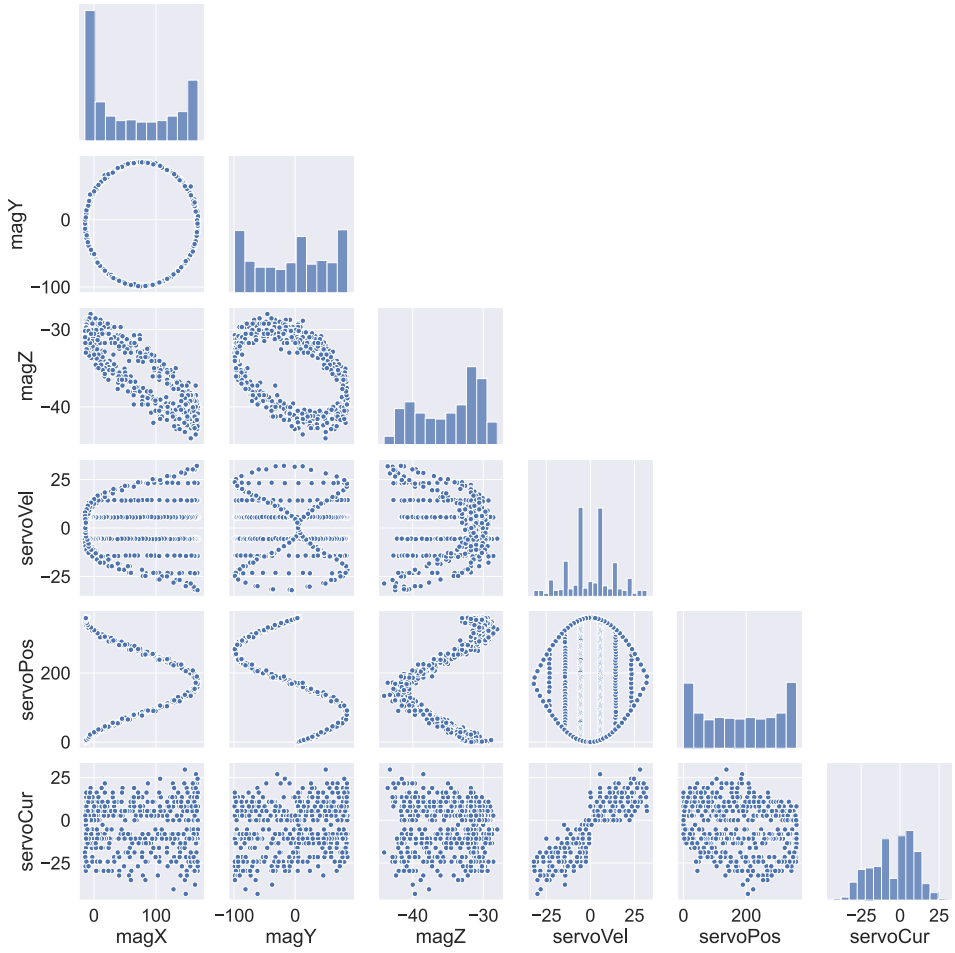

Figure A.3: Pair plot between the servo measurements and the magnetometer measurements from the baseline experiment.

A.2 Pair plots during servo actuation in the load experiment

The pair plots in Figures A.4, A.5 and A.6 displays the pair plots from the additional load experiments. The IMU and motor rotated a few degrees during the experiments, which can be seen in the scatter plots. The scatter plots were therefore deemed unreliable in terms of interpreting if there would be any correlation between the different features of the servo motor and the IMU measurements. It was these results that led to decision to compare the cross-talk model of the baseline and the additional load experiments.

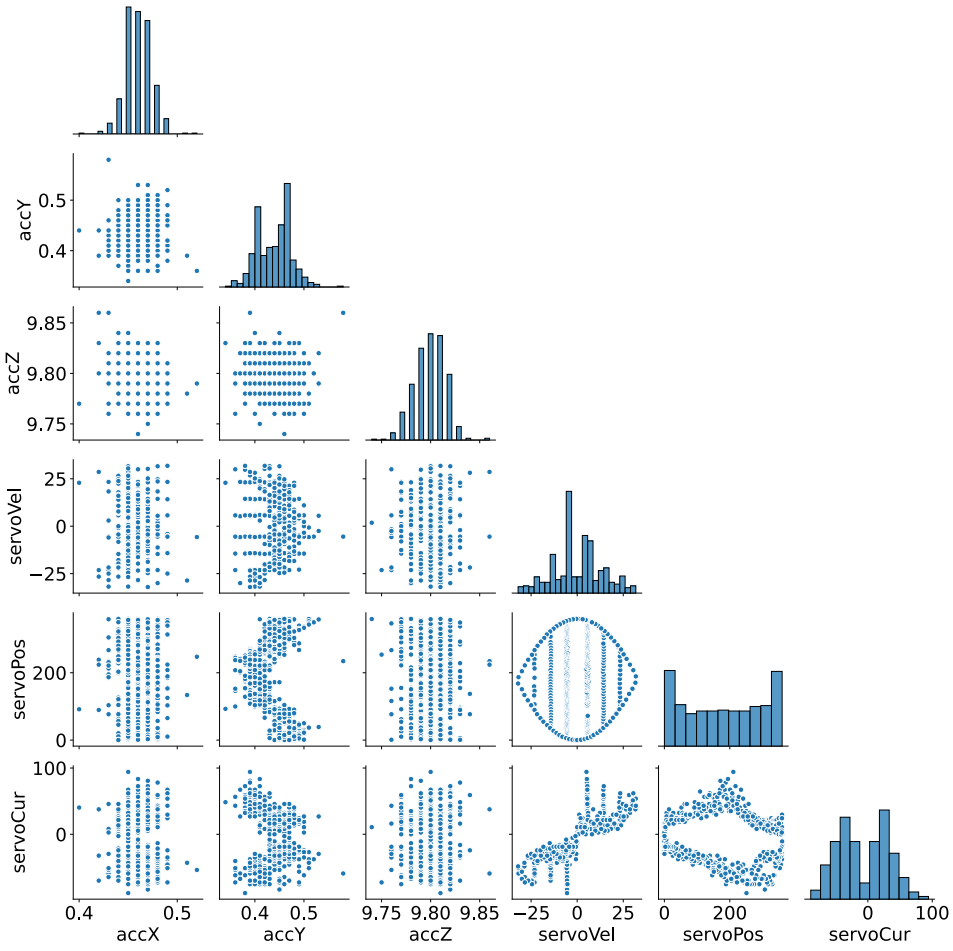

Figure A.4: Pair plot between the accelerometer measurements and the gyroscope measurements with load.

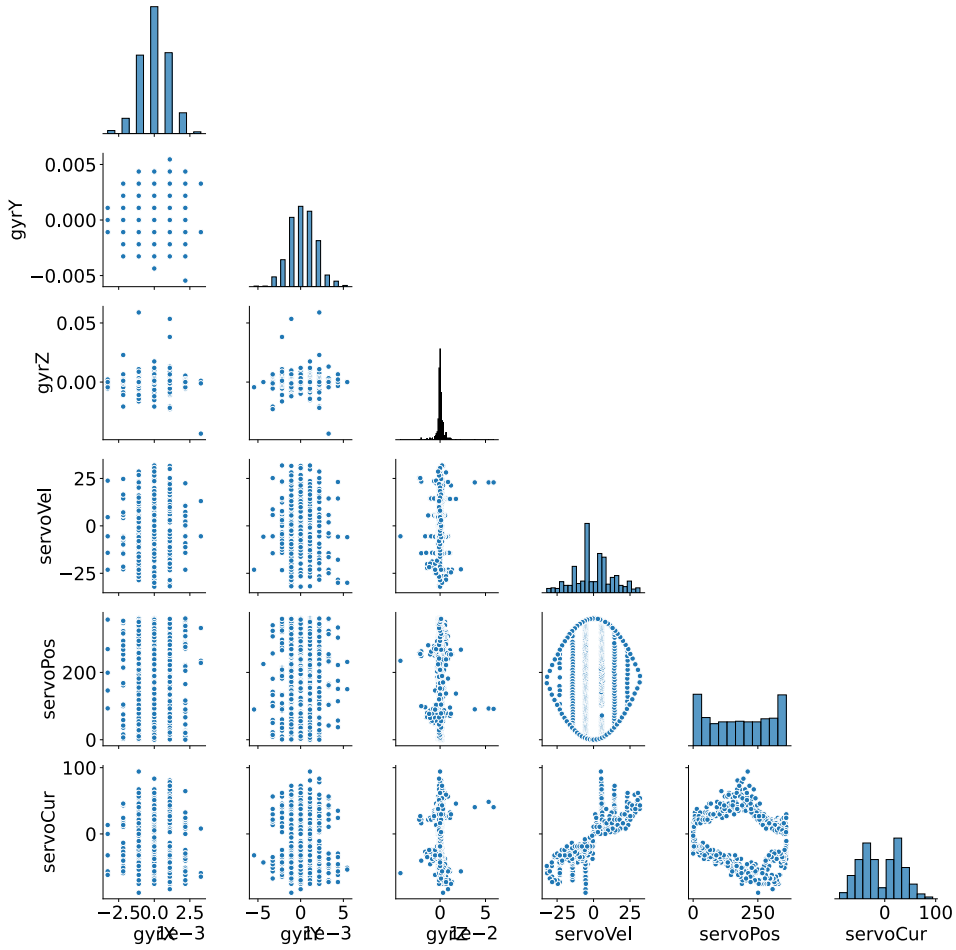

Figure A.5: Pair plot between the servo measurements and the gyroscope measurements with load.

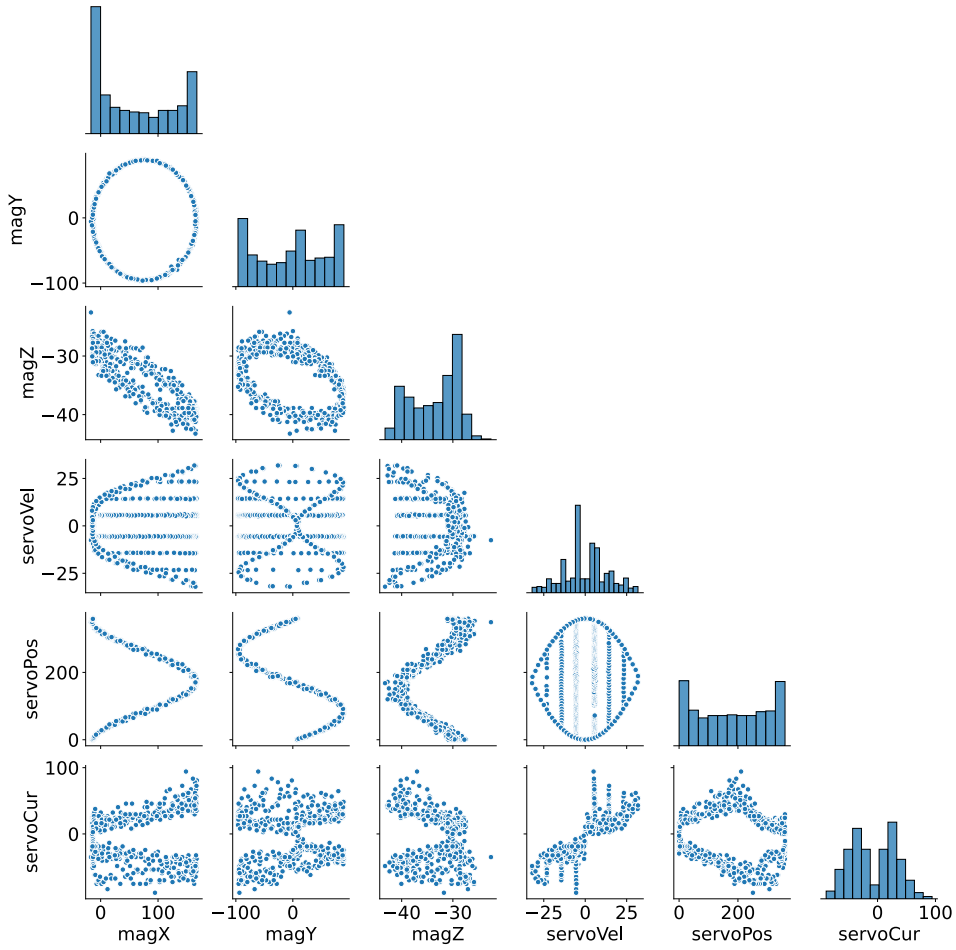

Figure A.6: Pair plot between the servo measurements and the magnetometer measurements with load.

A.3 Sample statistics before and after servo actuation with load

To avoid filling the results chapter with numbers, the sample statistic from before and after servo actuation with additional load are presented in Table A.1 and A.2. The most important numbers were extracted and used in the discussion. The sample statistics complemented the baseline experiments in characterizing the IMU measurement noise. They were also used to conclude that after servo actuation, the measurements are equal to before actuation.

Table A.1: Accelerometer sample statistics before and after the servo actuation in the additional load experiment. The statistics during servo actuation was omitted as experimental setup rotated during servo actuation.

	mean	**std**	**skew**	**kurtosis**
Before				
accX	0.466	0.011	0.157	-0.506
accY	0.527	0.015	0.296	0.828
accZ	9.794	0.016	-0.231	0.180
After				
accX	0.448	0.009	-0.058	0.924
accY	0.439	0.012	-0.030	-0.062
accZ	9.799	0.015	-0.217	-0.184

Table A.2: Gyroscope sample statistics before and after the servo actuation in the additional load experiment. The statistics during servo actuation was omitted as experimental setup rotated during servo actuation.

	mean	**std**	**skew**	**kurtosis**
Before				
gyrX	0.000	0.001	0.065	0.437
gyrY	0.000	0.002	-0.131	-0.045
gyrZ	-0.000	0.001	0.145	0.153
After				
gyrX	0.000	0.001	-0.029	-0.163
gyrY	0.000	0.002	-0.030	-0.009
gyrZ	-0.000	0.001	0.005	-0.009

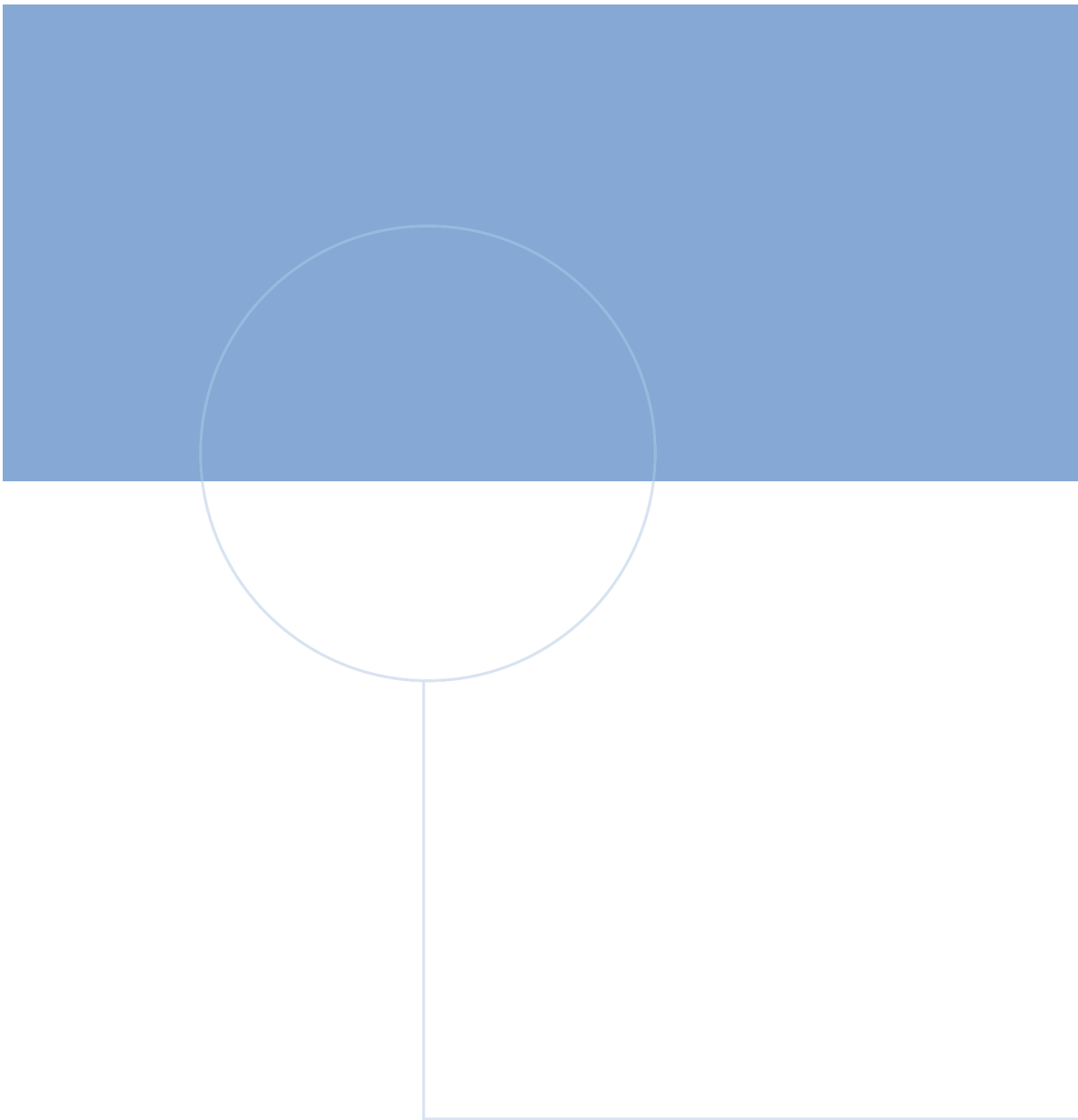

NTNU

Norwegian University of
Science and Technology